Published in ApJS, 132: 129-198, 2001

AN ULTRAVIOLET/OPTICAL ATLAS OF BRIGHT GALAXIES

Pamela M. Marcum[1], Robert W. O'Connell[2], Michael N. Fanelli [3,4], Robert H. Cornett[4], William H. Waller[4,5], Ralph C. Bohlin[6], Susan G. Neff[7], Morton S. Roberts[8], Andrew M. Smith[7], K.-P. Cheng[9], Nicholas R. Collins[4], Gregory S. Hennessy[2,10], Jesse K. Hill[4], Robert S. Hill[4], Paul Hintzen[11], Wayne B. Landsman[4], Raymond G. Ohl[2], Ronald A. Parise[12], Eric P. Smith[7], Wendy L. Freedman[13], Leslie E. Kuchinski[14], Barry Madore[14], Ronald Angione[15], Christopher Palma[2], Freddie Talbert[15], and Theodore P. Stecher[7]

Abstract. We present wide-field imagery and photometry of 43 selected nearby galaxies of all morphological types at ultraviolet and optical wavelengths. The ultraviolet (UV) images, in two broad bands at 1500 and 2500 Å, were obtained using the Ultraviolet Imaging Telescope (UIT) during the Astro-1 *Spacelab* mission. The UV images have ~ 3" resolution, and the comparison sets of ground-based CCD images (in one or more of *B*, *V*, *R*, and Hα) have pixel scales and fields of view closely matching the UV frames. The atlas consists of multiband images and plots of UV/optical surface brightness and color profiles. Other associated parameters, such as integrated photometry and half-light radii, are tabulated. In an appendix, we discuss the sensitivity of different wavebands to a galaxy's star formation history in the form of "history weighting functions" and emphasize the importance of UV observations as probes of evolution during the past 10-1000 Myr. We find that UV galaxy morphologies are usually significantly different from visible band morphologies as a consequence of spatially inhomogeneous stellar populations. Differences are quite pronounced for systems in the middle range of Hubble types, Sa through Sc, but less so for ellipticals or late-type disks. Normal ellipticals and large spiral bulges are fainter and more compact in the UV. However, they typically exhibit smooth UV profiles with far-UV/optical color gradients which are larger than any at optical/IR wavelengths. The far-UV light in these cases is probably produced by extreme horizontal branch stars and their descendants in the dominant, low-mass, metal-rich population. The cool stars in the large bulges of Sa and Sb spirals fade in the UV while hot OB stars in their disks brighten, such that their Hubble classifications become significantly later. In the far-UV, early-type spirals often appear as peculiar, ringlike systems. In some spiral disks, UV-bright structures closely outline the spiral pattern; in others, the disks can be much more fragmented and chaotic than at optical wavelengths. Contributions by bright active galactic nuclei (AGNs) to the integrated UV light in our sample range from less than 10% to nearly 100%. A number of systems have unusual UV-bright structures in their inner disks, including rings, compact knots, and starburst nuclei, which could easily dominate the UV light in high-redshift analogs. A significant but variable fraction of the far-UV light in spiral disks is diffuse rather than closely concentrated to star-forming regions. Dust in normal spiral disks does not control UV morphologies, even in some highly inclined disk systems. The heaviest extinction is apparently confined to thin layers and the immediate vicinity of young H II complexes; the UV light emerges from thicker star distributions, regions evacuated of dust by photodestruction or winds, or by virtue of strong dust clumpiness. Only in cases where the dust layers are disturbed does dust appear to be a major factor in UV morphology. The UV-bright plume of M82 indicates that dust scattering of UV photons can be important in some cases. In a companion paper, we discuss far-UV data from the Astro-2 mission and optical comparisons for another 35 galaxies, emphasizing face-on spirals.

Key words: galaxies: evolution-galaxies: fundamental parameters-galaxies: photometry-galaxies: structure-ultraviolet: galaxies

Table of Contents

- INTRODUCTION

- BACKGROUND AND MOTIVATION FOR ULTRAVIOLET IMAGING OF GALAXIES
  - Ultraviolet Probes of Galaxy Astrophysics
    - Ages and Metal Abundances of Stellar Populations
    - Star Formation Histories for *t* < 1 Gyr
    - Cold Interstellar Material
    - Hot Interstellar Material
    - Nuclear Structures

    - Low Surface Brightness Systems
  - Applications to High-Redshift Galaxies
  - UV Imaging of Galaxies

- OBSERVATIONS AND DATA REDUCTION
  - UIT Imaging
  - Ground-based Optical Imaging

- DATA ANALYSIS AND ATLAS PRESENTATION
  - Sample Selection
  - Treatment of Images
  - Flux Calibration and Error Analysis
  - Image Atlas
  - Photometry
  - Length Scales and Light Concentration

- COMMENTS ON INDIVIDUAL OBJECTS
  - Primary Objects
  - Secondary Objects

- DISCUSSION

- CONCLUSION

- APPENDIX A: STAR FORMATION HISTORY WEIGHTING FUNCTIONS

- APPENDIX B: GROWTH CURVE PHOTOMETRY

- REFERENCES

---

[1] Physics and Astronomy Department, Texas Christian University, Box 298840, Fort Worth, TX 76129; p.marcum@tcu.edu.
[2] Astronomy Department, University of Virginia, P. O. Box 3818, Charlottesville, VA 22903-0818; rwo@virginia.edu.
[3] Physics Department, University of North Texas, Denton, TX 76203-5370; fanelli@unt.edu.
[4] Raytheon ITSS, Code 681, NASA/GSFC, Greenbelt, MD 20771.
[5] Department of Physics and Astronomy, Tufts University, Medford, MA 02155.
[6] Space Telescope Science Institute, 3700 San Martin Drive, Baltimore, MD 21218.
[7] Laboratory for Astronomy and Solar Physics, Code 681, NASA/GSFC, Greenbelt, MD 20771.
[8] National Radio Astronomy Observatory, Charlottesville, VA 22903.
[9] Physics Department, California State University, Fullerton, CA 92634.
[10] Visiting Astronomer, Kitt Peak National Observatory and Cerro Tololo Inter-American Observatory of the National Optical Astronomy Observatories, operated by the Association of Universities for Research in Astronomy (AURA), Inc. under cooperative agreement with the National Science Foundation.
[11] US Naval Observatory, 3450 Massachusetts Avenue, NW, Washington, DC 20392-5420.
[12] Physics and Astronomy Department, California State University, Long Beach CA 90840.
[13] Computer Sciences Corporation, NASA/GSFC, Code 684.9, Greenbelt, MD 20771.
[14] Carnegie Observatories, 813 Santa Barbara Street, Pasadena, CA 91101-1292.
[15] Caltech, IPAC 100-22, Pasadena, CA 91125.
[16] Astronomy Department, San Diego State University, San Diego, CA 92182.

1. INTRODUCTION

Morphological analysis and classification are powerful tools for assessing the current evolutionary state and earlier history of galaxies. To date, however, these techniques have been based overwhelmingly on observations in the relatively narrow optical band, 4000-7000 Å. Because the appearance of galaxies is strongly dependent on wavelength, extension of morphological studies into both the infrared and ultraviolet wavelength regimes promises new insights into the nature of galaxies as well as independent tests of the elaborate conceptual framework that has been developed on the basis of optical band imagery.

The optical band light of galaxies is a mix of warm and cool stellar components, in which older populations have significant influence (as discussed in Appendix A). In optical images of spiral galaxies, both the cool bulge and hot spiral arm components can be bright. The presence of the interstellar medium is revealed through low to moderate ionization emission lines (e.g., H I, [N II], [O II], and [O III]) and extinction effects from dust, especially at wavelengths below 5000 Å. Near-infrared light emphasizes cool stellar components, mainly the red giant branch or cool supergiants, while simultaneously reducing the effects of extinction from dust. Spiral galaxies tend to be more concentrated and smooth in images at 8200 Å as compared to the *B* band, and spiral structure in many cases is less prominent (Elmegreen 1981).

The vacuum ultraviolet (< 3200 Å) is more sensitive to hot stellar components (young massive stars and advanced evolutionary phases of low-mass stars) and to dust than are the optical and near-IR. As first indicated by emission line maps (e.g., Hodge 1966; Hodge & Kennicutt 1983), which trace the locations of gaseous regions containing ionizing far-UV continuum, the appearance of galaxies in the UV can be dramatically different from that in the optical and IR. There is growing interest in the UV properties of nearby galaxies because of their importance for interpreting the rapidly enlarging sample of high-redshift galaxies detected in deep ground-based and space surveys.

In this and a companion paper (Kuchinski et al. 2000), we present the first comparative atlas of bright nearby galaxies at UV and optical wavelengths. The UV images were obtained by the Ultraviolet Imaging Telescope (UIT) during the Astro-1 and Astro-2 *Spacelab* missions in 1990 and 1995, respectively. The Astro-1 data set discussed in this paper includes both far-UV (~ 1500 Å) and mid-UV (~ 2500 Å) images; data for a total of 43 galaxies are presented. The atlas consists of multiband, wide field comparisons of galaxies at ~ 1"-3" resolution together with corresponding surface photometry. The comparison sets of ground-based optical band CCD images were obtained with pixel scales and fields of view which approximately match those of the UIT imagery. Kuchinski et al. (2000) discuss far-UV data from the Astro-2 mission and optical comparisons for another 35 galaxies, emphasizing face-on spirals.

This paper is organized as follows. In the next section we discuss the scientific potential and technical development of ultraviolet imaging of galaxies and the motivations for our work. Sections 3 and 4 describe the UIT and ground-based observations, reduction, and analysis of the data, and the presentation of images and photometry in the atlas. Section 5 provides notes on individual objects. Section 6 discusses some of the implications of our data. In Appendix A we discuss the concept of star formation history weighting functions. A complete table of UV/optical aperture photometry for the primary targets is presented in Appendix B.

2. BACKGROUND AND MOTIVATION FOR ULTRAVIOLET IMAGING OF GALAXIES

Changes in the two-dimensional light distribution of galaxies with wavelength can provide new and unique perspectives on their structures and evolution. The spectral region of interest here lies between the Lyman cutoff of the interstellar medium at 912 Å and the cutoff of the terrestrial atmosphere near 3200 Å. This window contains information on the character of stellar populations, dust grains, interstellar gas, and AGNs which is largely independent of that in the familiar optical bands. In this section we discuss the potential utility of the UV in understanding galaxy evolution and progress to date in exploiting these opportunities.

2.1. Ultraviolet Probes of Galaxy Astrophysics

2.1.1. *Ages and Metal Abundances of Stellar Populations*

The UV has the highest sensitivity of any spectral region to stellar temperature and metal abundance, implying that it is especially valuable as a means of characterizing stellar populations, current star formation rates (SFRs), and star formation histories. Stars with surface temperatures above ~ 10,000 K (e.g., main-sequence stars with masses $\gtrsim 3\ M_{\odot}$) are brighter in the UV than at longer wavelengths (Fanelli et al. 1992). Consequently, UV imaging or spectroscopy of star-forming galaxies permits direct detection of the massive stars responsible for most ionization, photodissociation, kinetic energy input, and element synthesis.

Figure 1 illustrates predicted UV-IR spectral energy distributions of stellar populations over timescales up to 3000 Myr. The strong time evolution of the UV compared to longer wavelengths is the reason for its utility in determining population ages. The sensitivity of the UV to stellar properties extends even to the cool ~ 1 $M_{\odot}$ stars near the main-sequence turnoff in the oldest model shown in Figure 1. These solar-type stars dominate the mid-UV (2000-3200 Å) light in this model, and chemical composition as well as age influences the spectrum. The concentration of strong metallic absorption features is responsible for much of the short-wavelength structure in this model. The abundance sensitivity of selected UV spectral regions is discussed by Fanelli et al. (1992).

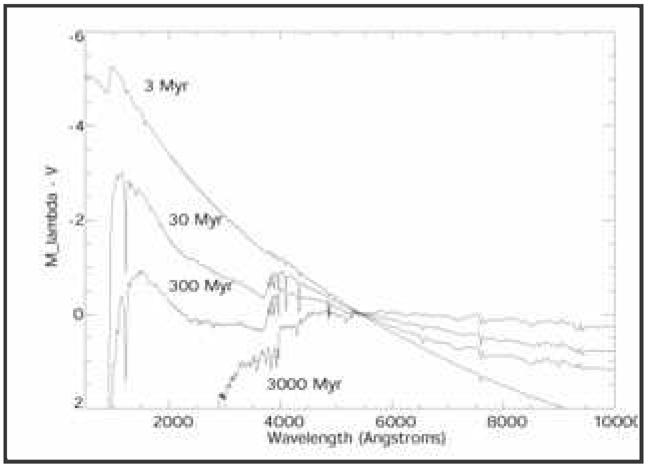

Figure 1. Synthetic spectral energy distributions of single generation stellar populations having Salpeter IMFs and solar abundances for ages 3-3000 Myr from Bruzual & Charlot (1993) , showing the rapid evolution in UV amplitude and shape. The shape of the near-IR spectrum (λ > 7000) is much less sensitive to age. Interstellar emission lines are not modeled here but would be absent in all except the 3 Myr SED.

In old, quiescent systems such as elliptical galaxies and spiral bulges, the UV offers a second major probe of stellar populations. Most old systems have been found to contain a very hot, low-mass stellar component with $T_{\rm eff} > 15{,}000$ K which dominates the far-UV light. This probably consists of stars with very thin envelopes on the extreme horizontal branch and subsequent advanced evolutionary phases (reviewed in Greggio & Renzini 1990 and O'Connell 1999). Their UV output is predicted to be very sensitive to their envelope masses and compositions. Overall, UV spectra are powerful age and abundance diagnostics for both young and old populations.

2.1.2. *Star Formation Histories for t < 1 Gyr*

The UV offers a unique probe of the star formation history of galaxies on intermediate timescales of 10-1000 Myr. By "history" we mean the star formation rate as a function of time, SFR(t). The most widely used methods for estimating the recent star formation rate, SFR(t_0), involve optical emission lines such as Hα, radio continuum emission from hot gas or relativistic electrons, and far-infrared or submillimeter continuum emission from dust grains (e.g., Kennicutt 1998). Both emission lines and free-free thermal radio continuum depend on photoionization from massive stars and therefore reflect activity only over the past ~ 5 Myr, after which photoionization rapidly decreases. This period represents only 0.05% of the star-forming lifetime of a typical galaxy. Nonthermal radio emission powered by supernova-driven relativistic electrons is a useful index of massive star formation over the past few tens of Myr (Condon 1992) but is influenced by the character of the surrounding interstellar medium. Infrared ($\lambda > 10\ \mu$m) and submillimeter thermal emission from dust grains is likewise strongly influenced by the nonstellar environment and has intrinsically poor time resolution, since grains can be heated by photons from stars of all ages.

These conventional methods for estimating recent SFRs are based on the indirect effects of massive stars, involving the downconversion of UV photons by surrounding media, and have either restricted or ill-defined age sensitivity. By contrast, the vacuum UV offers a direct measure of the light from the massive star populations. Extinction by dust is often cited as a serious obstacle to using direct FUV observations to infer star formation rates. However, the photoionizing UV continuum ($\lambda \lesssim 912$ Å) which drives line and free-free emission is possibly yet more sensitive to extinction, while there are fewer empirical constraints on its nature. The actual effects of dust on the emergent UV light are smaller than naively expected (see Section 2.1.3 and 6). All of these methods are comparably affected by uncertainties in extinction.

The timescales which can be probed by observations of the 1200-3200 Å continuum range from less than 10 Myr to $\gtrsim$ 1 Gyr. This critical interval is well sampled neither by the methods described above nor by the optical region (3200-9000 Å), which is influenced by the star formation history on longer timescales (more than a few Gyr). It is the "gap" which Gallagher, Hunter, & Tutukov (1984), for instance, were compelled to omit in their landmark study of spiral galaxy histories derived from Hα fluxes, *B*-band fluxes, and total masses.

An example of the additional information on galaxy star formation histories to be gained from UV continuum imaging is shown in Figure 2. This is a map comparing the Hα and far-UV morphologies of the well-known Sc galaxy M51. There are clearly large variations in the far-UV to Hα ratio. The ~ 10-50 Myr old populations (FUV-bright) are usually spread farther downstream from the putative density wave than the ~ 5 Myr old, Hα -bright populations, but the pattern is not entirely symmetrical. Diffuse far-UV light tends to "fill in" the spiral arms between intense concentrations of Hα light. There is a hint of multiple FUV wavelets, with feathery extensions inclined in pitch angle to the main spiral pattern. The UIT data for M51 are discussed further by Kuchinski et al. (2000). A similar comparison map based on a lower resolution UV image from the FOCA program (see Section 2.3) was published by Petit et al. (1996).

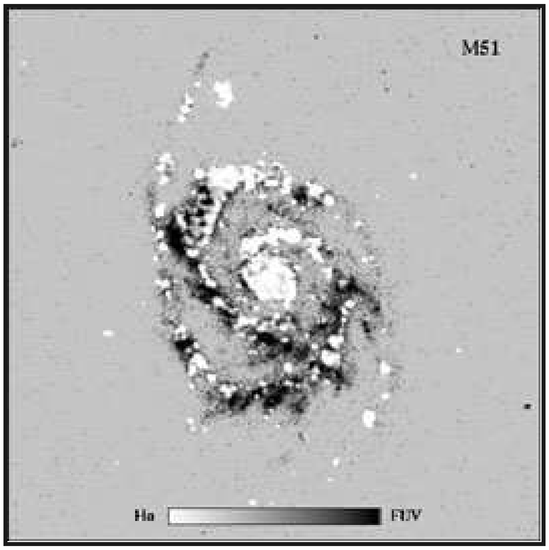

Figure 2. Hα-FUV difference map of the face-on Sc galaxy M51. The image shows the logarithmic difference between a continuum-subtracted ground-based Hα image and a UIT far-UV (1500 Å) continuum image taken by UIT during the Astro-2 mission. The map contrasts regions of current star formation ($\lesssim$5 Myr), which are bright in Hα and appear as white/light gray in the image, with regions active during the era 5-50 Myr in the past, which are relatively brighter in the FUV continuum and are represented by dark gray/black in the image.

The sensitivity of different wavebands to a galaxy's star formation history is discussed further in the form of "history weighting functions" in Appendix A.

2.1.3. *Cold Interstellar Material*

The UV offers high sensitivity to interstellar dust and regions of concentrated cold material (i.e., potential star formation sites). Before the advent of UV observations of galaxies, it was widely assumed that this would actually be a serious disadvantage because the Galactic extinction law (e.g., Cardelli, Clayton, & Mathis 1989) yields $A(\mathrm{UV}) / A(V) > 2.5$, implying that the UV light of typical disk galaxies might be strongly suppressed. However, as is amply demonstrated by the images in this atlas and spectroscopic studies (e.g., Calzetti, Kinney, & Storchi-Bergmann 1994), dust does not dominate the UV morphology of most galaxies.

The UV may ultimately prove to be a valuable tracer of quiescent, cold, molecular material. Because the albedo of dust is high in the UV, cool interstellar clouds far from star-forming regions can be detected by scattered light, as in the case of the faint gaseous outer arms of M101 (Donas et al. 1981; Stecher et al. 1982) or the outer halo of NGC 1068 (Neff et al. 1994). UV imaging can also detect H_2 in photodissociation regions directly by virtue of its fluorescence bands in the 1550-1650 Å region (e.g., Witt et al. 1989; Martin, Hurwitz, & Bowyer 1990). Although such regions occupy only a small fraction of the total volume of a typical molecular cloud, nonetheless the direct detection of H_2 has, in principle, considerable advantages over methods involving trace constituents like radio-emitting CO (see Allen et al. 1997 and references therein).

2.1.4. *Hot Interstellar Material*

The UV contains uniquely important emission line probes of interstellar gas in the $T \sim 10^5$-10^6 K regime, including C IV (λ1550), N V (λ1241), and O VI (λ1035). These spectral diagnostics have been extensively exploited in absorption-lin spectroscopic studies of our galaxy. Little has been done to date using imaging, though C IV images of supernova remnants have been published (e.g., the Cygnus Loop, Cornett et al. 1992; N49 in the LMC, Hill et al. 1995c).

2.1.5. *Nuclear Structures*

The nuclei of galaxies are often UV-bright. The optical-UV energy distributions of AGNs and associated nonthermal jets are relatively flat, and their contrast against the stellar background is usually better in the UV than in the optical band. Activity has been detected by UV imaging in a number of nearby galaxies (e.g., Maoz et al. 1995; Renzini et al. 1995; Barth et al. 1998). Spiral nuclei often contain starburst cores or ringlike structures, which are again more prominent in the UV (e.g., in M83, Bohlin et al. 1983; NGC 1068, Neff et al. 1994). The leverage of the UV in isolating such hot sources is especially important in spiral bulges and E galaxies, where the cool star background is often overwhelming at optical wavelengths.

2.1.6. *Low Surface Brightness Systems*

A minimum in the natural night sky background occurs at 1600-2400 Å. This is the deepest window in the UV-optical-IR spectrum and permits detection of extremely low surface brightness objects, perhaps up to 100,000 times fainter than the ground-based sky (O'Connell 1987; Waller et al. 1995). Applications include the study of faint circumgalactic star-forming regions in nearby galaxies and faint blue galaxies at redshifts up to ~ 1 (Martin et al. 1997; Treyer et al. 1998) and detection of low surface brightness disk systems (O'Neil et al. 1996).

2.2. Applications to High-Redshift Galaxies

UV imaging of nearby galaxies is relevant to galaxies at high redshift for two reasons. First, as just described, the rest-frame UV continuum is a robust tracer of star formation and is measurable to very high redshifts ($z \gtrsim 10$) with optical/IR instruments. For instance, the 2800 Å rest-frame continuum has been used to estimate the cosmic star formation density at $z \sim 0.5$-4 for the Canada-France Redshift Survey, Hubble Deep Field, and other surveys (Pei & Fall 1995; Lilly et al. 1995; Madau et al. 1996; Steidel et al. 1999), leading to the conclusion that gas processing occurred at a relatively constant rate for $z \sim 1$-4 but has precipitously declined since $z \sim 1$.

Second, observations of high-z galaxies are preferentially made in the rest-frame UV. This is particularly true for ground-based telescopes, where the rapidly increasing night sky brightness for wavelengths above 7000 Å, and thermal emission beyond 2 μm, seriously compromises observations in the near infrared. Because of the strong changes in galaxy appearance with wavelength, as illustrated in this atlas, there is a large "morphological k-correction" which must be quantified in order to distinguish genuine evolutionary effects from simple bandshifting.

High-redshift studies are also strongly influenced by reduced spatial resolution and by surface brightness selection. The latter is a very serious problem for $z \gtrsim 1$ because $I \sim I_0(1 + z)^{-n}$, where I_0 is the surface brightness in the rest-frame and $n = 3$ or 5 for monochromatic surface brightnesses per unit frequency or wavelength, respectively; $n = 4$ for bolometric surface brightnesses. Figure 3 illustrates these effects using a far-UV image of the luminous, nearby Sc spiral M101. Bohlin et al. (1991) and Giavalisco et al. (1996) describe methods of creating such simulations from rest-frame UV data.

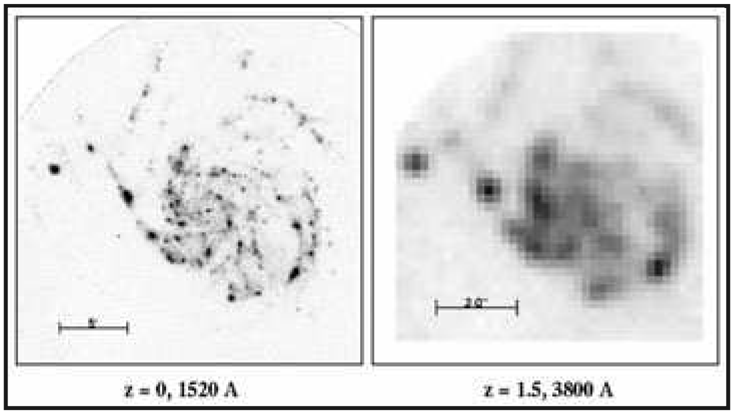

Figure 3. *Left panel*: A far-UV (1500 Å) image of the luminous Sc galaxy M101 obtained by UIT during the Astro-2 mission. A 5' bar is shown for scale. *Right panel*: A simulation of a galaxy with the same structure but 10 times higher surface brightness at a redshift z = 1.5 as observed by the Keck 10 m telescope in a 10 hr exposure with 0".5 FWHM seeing against a sky background of 22.5 mag arcsec^{-2}. A 2" bar is shown for scale. The simulation is not easily recognizable as a normal spiral galaxy. Its asymmetries are emphasized; it appears distorted and fragmented. High surface brightness star-forming associations in its disk have taken on the appearance of nearby "companions."

It is possible to explore bandshifting effects using multicolor (e.g., *B* and *R*) optical images to extrapolate the spectral energy distribution to the rest-frame UV on a pixel-by-pixel basis. This has been done using ground-based data (e.g., Abraham 1997; Abraham, Freedman, & Madore 1997; Brinchmann et al. 1998) and moderate-redshift *Hubble Space Telescope* (*HST*) data (Bouwens, Broadhurst, & Silk 1998). These studies, as well as those based on *HST*/NICMOS observations in the rest-frame optical bands (e.g., Bunker 1999, Corbin et al. 2000), conclude that the peculiarities in shape and size distributions found in the deep *HST* surveys considerably exceed the effects of bandshifting. While this is probably a robust result, these extrapolation methods do not accurately capture the range of rest-frame UV spectra found in real galaxies and are not suitable for making detailed comparisons with the local universe. The reason is that there is considerable scatter in UV colors of nearby galaxies at any given optical color. This is true even in the classic (*U-B*, *B-V*) diagram (e.g., Larson & Tinsley 1978), but it is much more pronounced in the rest-frame UV, where, for instance, Donas, Milliard, & Laget (1995) found a 3 mag range in (UV-*b*) colors at a given (*b-r*) color in a faint galaxy sample. This UV/optical decoupling is confirmed in spectroscopy of UV-selected samples by Martin et al. (1997) and Treyer et al. (1998). The implication is that the true evolutionary history of galaxies on timescales more recent than a few Gyr can be rather different from that inferred from optical data.

Fiducial photometric and imaging studies of nearby galaxies in the rest-frame UV are needed in order to calibrate these selection and morphological effects and to improve our understanding of the astrophysical drivers of the rest-frame UV luminosity, particularly the influence of dust and the history of star formation.

2.3. UV Imaging of Galaxies

Extragalactic UV astronomy to date has been largely based on spectroscopy, usually with small entrance apertures (1"-20") centered on galaxy nuclei (e.g., *IUE*, *HST*/FOS, *HST*/GHRS). Several hundred objects have also been photometered in broad bands with large apertures. Early photometric surveys were performed by OAO and ANS; the most recent large-scale study was by FAUST (Deharveng et al. 1994). The total number of UV spectroscopic and photometric observations of galaxies still far exceeds the number of imaging observations (an inversion of the historical development of optical extragalactic astronomy). Brosch (1999) has recently reviewed the available results of UV surveys of galaxies. No all-sky UV survey faint enough to include galaxies has yet been conducted, but this will be remedied by the GALEX mission (Martin et al. 1999).

The first UV *image* (defined as having many resolution elements over the area of interest) of another galaxy was obtained by the NRL Apollo S201 camera from the lunar surface in 1972 (Page & Carruthers 1981). This was of the Large Magellanic Cloud in the 1250-1600 Å band and dramatically demonstrated a strong wavelength-dependent morphology. Its remarkably fragmented appearance in the UV is entirely different from its familiar barlike shape in the optical continuum.

Subsequent progress in UV imaging up to 1990 was relatively slow (reviewed in O'Connell 1991). Since 1990, we have accumulated a sample of vacuum UV images of about 200 galaxies, principally from three instruments:

1. The *Hubble Space Telescope* Faint Object Camera (*HST*/FOC). Because of its better rejection of red leaks (i.e., residual response to low-energy photons outside the primary UV bands) the *HST*/FOC has been more extensively used for UV imaging than the *HST*/Wide Field Planetary Cameras. Its main limitation is a small field of view. FOC produced the first extensive compilation of galaxy UV images in an atlas of the nuclei (22" fields) of 110 nearby galaxies at 2300 Å with 0".05 resolution (Maoz et al. 1996). Many of the objects exhibit UV-bright nuclear structures, including a number of star-forming rings and five cases of unusually bright LINER active nuclei (Maoz et al. 1995). Far-UV (<2000 Å) imaging even with FOC is compromised by red leaks, but the newer *HST*/Space Telescope Imaging Spectrograph camera provides pure UV imaging over 25" fields (e.g., Brown et al. 2000).
2. The SCAP/FOCA balloon-borne telescope of the Marseille and Geneva groups. SCAP/FOCA operates in a narrow atmospheric window near 2000 Å with a large field of view of up to 2°.3 and resolution of ~ 15" (Deharveng et al. 1980; Milliard, Donas, & Laget 1991; Donas et al. 1995). By virtue of a fast *f*/ratio and long integration times, it can reach relatively low UV surface brightnesses despite its narrow band. A number of bright galaxies have been studied morphologically and photometrically with SCAP/FOCA. Donas et al. (1987) summarized integrated UV photometry for a sample of 149 spiral and irregular galaxies. A sample of fainter, mostly unresolved, UV-detected galaxies near the north galactic pole has been recently discussed by Donas et al. (1995) and Treyer et al. (1998). Fewer objects have been studied with resolved imaging; individual citations are given in Section 5.
3. The Ultraviolet Imaging Telescope (UIT), from which the UV images in this atlas were obtained. UIT has a field of view of 40' and spatial resolution of 3" and was intended to provide a good match to the performance of typical ground-based telescopes on large angular diameter, nearby galaxies. UIT is described in detail in the next section.

Because of technical difficulties in achieving high reflectivity optics shortward of 1100 Å and in rejecting the very bright geocoronal Lyα line at 1216 Å from exposures centered at shorter wavelengths, both the *HST* and UIT imaging cameras work primarily at wavelengths longer than 1216 Å.

3. OBSERVATIONS AND DATA REDUCTION

3.1. UIT Imaging

The ultraviolet images of galaxies presented here were obtained by the UIT, which was one of the three copointed UV telescopes of the Astro observatory. UIT was designed and constructed at NASA-Goddard Space Flight Center by a team headed by T. P. Stecher. The final instrument is an outgrowth of a series of prototype experiments carried on sounding rockets in the 1970s and 1980s for missions of ~ 5 minute duration, from which a number of UV images of galaxies and star clusters with lower spatial resolution were published. UIT flew on two Space Shuttle missions, Astro-1 in 1990 December and Astro-2 in 1995 March.

A complete description of UIT, its performance, and standard data processing and calibration procedures is given in Stecher et al. (1992, 1997). UIT is an f/9 Ritchey-Chrètien telescope with a 38 cm aperture. It contains two cameras, each of which consists of a magnetically focused, two-stage image intensifier with a phosphor output which is fiber-optically coupled to 70 mm film. The mid-ultraviolet (MUV, 1800-3200 Å) camera, designated "A," employs a Cs_2Te photocathode. The far-ultraviolet (FUV, 1200-1800 Å) camera, designated "B," has a CsI photocathode. The photocathode responses combined with the filters yield excellent long-wave rejection; no evidence of "red leaks" has been detected on extragalactic images. The UIT field of view is 40' in diameter. There is some vignetting and reduced image quality in the outer 2' of the field, but most of the images in this atlas are taken from the field center. Fine guidance during exposures is accomplished by an articulated secondary mirror coupled to an external star tracker and gyroscope assembly.

The cameras carried a total of 11 filters, but the images discussed here were taken through only three of these, listed in Table 1. $A1$ and $B1$ are the primary broadband filters for the MUV and FUV cameras, respectively. $B5$ is an FUV filter with a slightly reduced bandwidth to avoid strong airglow emission lines shortward of 1450 Å. This filter was primarily used during orbital daytime exposures. Note that the effective wavelength of the very broad $A1$ filter depends on the spectral energy distribution of the source. UIT filter sensitivity functions are displayed in Stecher et al. (1992, 1997).

Table 1. UIT Filters

Filter (1)	Substrate (2)	λ_{eff} (Å) (3)	Peak λ (Å) (4)	$\delta\lambda$ (Å) (5)
Mid-ultraviolet:				
A1...	Fused SiO_2	2488	2763	1147
Far-ultraviolet:				
B1...	SrF_2	1521	1443	354
B5...	Crystal SiO_2	1615	1518	225

The UV filters used here are insensitive to line emission in normal galaxies. There could be a small line contribution to the net flux in *B*1 or *B*5 in objects with very strong C IV 1550 Å emission, but the *A*1 filter is so broad, and mid-UV line emission so faint, that it is essentially a pure continuum filter.

The developed film was digitized using Perkin-Elmer 1010m microdensitometers. Astro-1 data frames were scanned with a 20 μm square aperture and a sample spacing of 20 μm. Astro-2 frames were scanned with a 20 μm square aperture but with a sample spacing of 10 μm; frames used in this study were then box-averaged to a 20 μm pixel. Standard processing steps for the densitometered data included background fog subtraction, linearization, flat-fielding, and flux calibration. Flux calibration and uncertainties are described in more detail in Section 4. Astrometry for most UIT frames was obtained using the *Hubble Space Telescope* Guide Star Catalog (Lasker et al. 1990).

This standard "pipeline" data reduction process produces 2048 × 2048 images with pixel sizes 1".14 square containing the circular 40' diameter data field surrounded by a section of unexposed film. Calibrated data frames are produced in the observed spatial orientation as defined by the spacecraft roll angle, and in a north-up, east-left orientation, corrected for the geometric distortion induced by the UIT image intensifier. These, and frames at several other steps in the pipeline process, can be obtained electronically from the Multimission Archive at the Space Telescope Science Institute.

Almost all of the data discussed here were derived from the inner 80% of the full UIT field, for which vignetting is negligible. Typical values of the full width at half-maximum (FWHM) of the point spread function in this region are 2".7 and 3".0 for the MUV and FUV cameras, respectively, although individual frames may yield larger FWHMs in the case of pointing system disturbances. The point spread function is approximately Gaussian, with an extended tail at large radii.

3.2. Ground-based Optical Imaging

A primary goal of the UV imaging program was to compare galaxy morphologies across a wide spectral range. Therefore, we carried out an optical band imaging survey of the UIT sample to provide the ancillary data necessary for quantitative analysis of their stellar and interstellar components. Wide-field CCD images in *B*, *V*, *R*, and Hα were obtained between 1991 and 1994 at Kitt Peak, Cerro Tololo, and Mount Laguna Observatories. Table 2 presents the location and dates of observing runs associated with the data set described in this paper. Given the large angular extent of some UIT targets, we required CCDs with the largest available format. Many of these observations were obtained with the first generation of scientific-grade 2K chips. Characteristics of each observing set are described below. Digital versions of some of the optical imagery were presented by Cheng et al. (1996).

Table 2. Observing Runs

Observatory (1)	Start Date (2)	Number of Nights (3)
Astro-1...	1990 Dec 2	10
KPNO...	1990 May 27	7
KPNO...	1991 Mar 7	7
KPNO...	1991 Dec 30	7
CTIO...	1991 Dec 5	7
CTIO...	1992 Feb 5	7
CTIO...	1992 Nov 20	7
CTIO...	1992 Nov 27	5
MLO...	1991 Feb 18	3
MLO...	1991 May 10	3
MLO...	1991 Oct 7	2
MLO...	1991 Dec 12	1
MLO...	1993 Aug 22	2
MLO...	1992 Nov 1	1
MLO...	1993 Nov 7	2

All UIT-related observations at Kitt Peak National Observatory (KPNO) were made using the 0.9 m telescope and either a Tektronix or T2KA CCD. The imagery taken from Cerro Tololo Inter-American Observatory (CTIO) was obtained using a 0.9 m telescope with either a Tek2048, Tek1024, or Thompson 1024 CCD detector. Additional images were obtained using the 1.0 m telescope with a TI 800 CCD at Mount Laguna Observatory (MLO), which is operated by San Diego State University at a dark site ~ 45 miles inland from San Diego. Pixel scales for these instruments were comparable or smaller than that of UIT, ranging from 0".4 to 1".5 pixel^{-1}.

Standard data reductions (bias and overscan correction, flat-fielding, cosmic ray rejection, and cosmetic corrections) for ground-based frames were performed using IRAF. Additional processing, which included astrometic solutions, artifact masking, registration to the UV imagery, and photometric calibration were carried out using software developed by us in IDL. [16] These tasks are further detailed in Section 4.

4. DATA ANALYSIS AND ATLAS PRESENTATION

4.1. Sample Selection

UIT pointings were chosen by the UIT science team and guest observers with an emphasis on breadth of coverage of galaxy types, likely UV brightness, low foreground extinction, and a size (typically more than 5' diameter) which takes advantage of the UIT's large field of view. Given the short duration of the Astro missions and the brief ($\lesssim$35 minute) periods during which the spacecraft was in Earth's shadow, it was not possible to conduct statistically complete surveys or very deep exposures. Technical difficulties with the Shuttle data display units often reduced exposure times below requested values. This atlas includes data from all Astro-1 UIT frames containing identifiable images of galaxies, excluding fields centered on the Magellanic Clouds, which have been discussed elsewhere by Cheng et al. (1992); Cornett et al. (1994, 1997); Hill et al. (1993a, 1994a, 1995c); and Parker et al. (1996, 1998).

Often, galaxies in addition to the intended target are present in the field. All galaxies which were readily detectable as UV sources on the selected UIT images are included in this atlas. Identification of cataloged sources in the UV frames was accomplished by comparing each image with Digital Sky Survey images obtained using SkyView (McGlynn, Scollick, & White 1996), and searching relevant catalogs using a 20' radius around the central coordinate of the image. We did not attempt a rigorous selection of very faint or uncataloged sources. Examples of examination of UIT data frames for very low surface brightness objects may be found in O'Neil et al. (1996).

Table 3 lists the objects which were found to be UV sources in the Astro-1 images. Sources which are both strongly detected and have an angular diameter exceeding 30" in the MUV are classified as "Primary" objects. For these we present multiband imagery, corresponding azimuthally averaged radial surface brightness profiles and integrated magnitudes. Objects which are either weakly detected or appear as point sources are classified as "Secondary" objects. For these we present UV images and integrated quantities.

Table 3. Atlas Galaxy Sample

Object (1)	Alt. ID (2)	R.A. (2000) (3)	Decl. (2000) (4)	V_0 (km s^{-1}) (5)	D (Mpc) (6)	Dist. Ref. (7)	Scale (pc $arcsec^{-1}$) (8)	M_{B_0} (mag) (9)	RC3 Type (10)	RSA Type (11)
Primary Objects										
NGC 221...	M32	00 42 41.9	+40 51 55	-28	0.76	1	3.7	-15.70	cE2	E2
NGC 224...	M31	00 42 44.4	+41 16 08	-121	0.76	1	3.7	-20.37	SA(s)b	Sb I -II
NGC 598...	M33	01 33 50.9	+30 39 37	-46	0.84	2	4.1	-18.54	SA(s)cd	Sc(s) II-III
NGC 628...	M74	01 36 42.1	+15 47 11	753	7.6	3	36.8	-19.58	SA(s)c	Sc(s) I
NGC 1068...	M77	02 42 40.2	-00 00 48	1144	15.3	4	74.1	-21.36	SA(rs)b Sy2	Sb(rs) II
NGC 1275...	Pers A	03 19 48.5	+41 30 45	5362	71.5	4	347	-22.38	cD,pec Sy2	
NGC 1316...	Fornax A	03 22 41.6	-37 12 28	1674	17.0	5	82	-21.73	SAB(s)0,pec	Sa,pec
NGC 1317...		03 22 44.7	-37 06 10	1822	17.0	5	82	-19.24	SAB(r)a	Sa
NGC 1399...		03 38 29.0	-35 26 58	1323	17.0	5	82	-20.60	E1,pec	E1
NGC 1404...		03 38 51.7	-35 35 36	1805	17.0	5	82	-20.18	E1	E2
NGC 2146...		06 18 40.1	+78 21 19	1035	13.8	4	66.9	-19.65	SB(s)ab,p	Sb II,pec
NGC 2992...		09 45 42.1	-14 19 39	2125	28.9	4	140	-19.43	Sa,pec Sy2	Sa (tides)
NGC 2993...		09 45 48.4	-14 22 08	2224	28.9	4	140	-19.46	Sa,p	Sab (tides)
NGC 3031...	M81	09 55 33.5	+69 04 00	69	3.6	6	17.4	-20.05	SA(s)ab	Sb(r) I-II
NGC 3034...	M82	09 55 54.0	+69 40 57	323	3.6	6	17.4	-18.61	I0	Amorphous
UGC 5336...	Ho IX	09 57 30.0	+69 02 00	154	3.6	6	17.4	-13.64	Im	
UGC 6697...		11 43 48.7	+19 58 12	6678	86	7	417	-20.59	Im	
NGC 4151...		12 10 32.4	+39 24 30	1022	13.6	4	66	-19.17	SAB(rs)ab Sy1.5	Sab
NGC 4321...	M100	12 22 55.2	+15 49 23	1540	16	8	77	-21.03	SAB(s)bc	Sc(s) I
Secondary Objects										
Mrk 335...		00 06 19.5	+20 12 09	7846	105	4	509		S0/a Sy1	
NGC 891...		02 22 33.1	+42 20 48	661	8.8	4	42.7	-19.23	SA(s)b?	Sb on edge
NGC 1267...		03 18 44.9	+41 28 04	5161	71.5	4	347		E+	
NGC 1268...		03 18 44.9	+41 29 18	3226	43.0	4	208		SAB(rs)b	
NGC 1270...		03 18 58.5	+41 28 18	4973	71.5	4	347	-20.71	E	
NGC 1272...		03 19 21.3	+41 29 32	4123	71.5	4	347	-22.11	E+	
NGC 1273...		03 19 27.2	+41 32 25	5453	71.5	4	347	-20.75	SA(r)0?	
UGC 2665...		03 19 27.4	+41 38 07	7909	104	4	504		Scd?	
NGC 1277...		03 19 51.8	+41 34 25	5084	71.5	4	347	-20.36	S0+,pec	
NGC 1278...		03 19 54.4	+41 33 50	6148	71.5	4	347	-21.45	E,pec	
NGC 1282...		03 20 12.1	+41 22 05	2294	30.6	4	148	-19.30	E	
NGC 1396...		03 38 06.3	-35 26 25	771	17.0	6	82	-16.35	SAB0-	
NGC 2551...		08 24 49.3	+73 24 46	2384	32	4	155	-19.50	SA(s)0/a	Sb(r) I-II

NGC 3837...		11 43 56.7	+19 53 42	6230	86	7	417	-20.42	E	
MCG3-30-71...		11 44 01.9	+19 46 57	4886	65	4	315	-18.52	Irr	
NGC 3842...		11 44 02.0	+19 57 01	6164	86	7	417	-21.89	E	
CGCG 97-114...		11 44 47.2	+19 46 22	6369	86	7	417	-19.37	Irr	
NGC 4156...		12 10 49.7	+39 28 24	6782	90	4	436	-20.81	SB(rs)b	
UGC 7188...		12 11 16.5	+39 24 08	1030	13.6	4	66		SBm	
NGC 4470...		12 29 37.9	+07 49 22	2272	16	8	78	-18.00	Sa?	
NGC 4472...	M49	12 29 46.5	+07 59 58	846	16	8	78	-21.65	E2	$E1/S0_1$
NGC 4476...		12 29 58.7	+12 20 53	1873	16	8	78	-18.11	SA(r)0-	E5,pec
NGC 4478...		12 30 17.4	+12 19 44	1329	16	8	78	-18.76	E2	E2
NGC 4486...	M87	12 30 49.7	+12 23 24	1229	16	8	78	-21.43	E0,pec	E0

Notes. - Col. (1): Galaxy identification. Col. (2): Alternate identification. Col. (3): Right ascension of the galaxy centroid taken from the RC3, in units of hours, minutes, and seconds. Col. (4): Declination of the galaxy centroid taken from the RC3, in units of degrees, arcminutes, and arcseconds. Col. (5): Recession velocity in km s^{-1}, corrected to the Galactic standard of rest as presented in the RC3. Col. (6): Adopted distance in megaparsecs. Col. (7): Distance references, given below. Col. (8): Physical scale in parsecs per arcsec using the distance given in col. 7. Col. (9): Absolute B magnitude, derived from B_T, corrected for Galactic foreground absorption, using the distance given in col. 7. Col. (10): Morphological type from the RC3. Col. (11): Morphological type from the Revised Shapely Ames Catalog.

References for Distance Estimates. - (1) Freedman 1990, Freedman & Madore 1990; (2) Freedman et al. 1991; (3) Sohn & Davidage 1996, Sharina et al. 1996; (4) distance obtained from recessional velocity listed in col. (7) and H_0 = 75 km s^{-1} Mpc^{-1}; (5) Fornax cluster members, Kohle et al. 1996, Shaya et al. 1996, McMillan et al. 1993; (6) Freedman et al. 1994; (7) D'Onofrio et al. 1997, Fruscione & Gavazzi 1990, Godwin & Peach 1982; (8) Ferrarese et al. 1996.

4.2. Treatment of Images

Table 4 summarizes information pertaining to both the UIT and ground-based images, such as exposure times and image sources. A footnoted entry in column (4) indicates that multiple images of adequate quality were obtained for that object. In such a case, the listed UIT frame number is the best image of the set (e.g., it has the longer exposure time or optimally shows low surface brightness structures). Where there are multiple images for a given filter with comparable exposure times, the images have been registered, scaled, and co-added to improve the signal-to-noise ratio. Addition of UIT images for objects which are only marginally detected does not significantly enhance the detection. In situations for which a short and a long exposure exist for a particular object, the shorter exposure was used to replace any saturated pixels in the longer exposure. Saturated pixels in the UV data (those with E-unit values $\geq$ 1500 in the notation of Stecher et al. 1997) were found for a few of the brightest galaxy nuclei (e.g., Mrk 335) and star-forming regions (as found in NGC 598) but were common in the optical images. Spatial registration of images was accomplished using field star astrometry obtained from the *HST* Guide Star Catalog (Lasker et al. 1990). Many of the FUV frames did not contain enough bright field stars to accurately derive an astrometric solution. In such cases, we used either spacecraft telemetry, uncataloged field stars, or morphological features of the targets to register and align the images. For Andromeda (NGC 224), a mosaic covering a roughly 1° field of view was constructed from two different UIT pointings. Image panels for the primary objects are presented in Figures 4*a* - 22*a*. Secondary objects are displayed in Figures 23*a* - 23*b*.

Table 4. Ultraviolet-Optical Image Information

Object (1)	Filter (2)	t_{exp} (s) (3)	UIT Frame/Observatory (4)	Date (5)	Calibration Reference (6)
			Primary Objects		
NGC 221...	B1	582.5	0485f	1990 Dec 9	
	A1	583.5	0388f	1990 Dec 9	
NGC 224...	B1	384.5	0266f [a]	1990 Dec 7	

	A1	330.5	0236f	1990 Dec 7	
NGC 598...	B1	424.5	0496f[a]	1990 Dec 9	
	A1	416.5	0402f[a]	1990 Dec 9	
	R	120.0	KPNO[a]	1992 Jan 1	1
	Hα	600.0	KPNO[a]	1992 Jan 1	2
NGC 628...	B1	514.5	0172f	1990 Dec 6	
	A1	530.5	0161f	1990 Dec 6	
	B	600.0	MLO	1991 Oct 8	1,3,4
	V	300.0	MLO	1991 Oct 8	1,3,4
	R	180.0	MLO	1991 Oct 8	1,4
	Hα	900.0	MLO	1991 Oct 8	5
NGC 1068...	B1	563.5	0411f[a]	1990 Dec 6	
	A1	752.5	0303f[a]	1990 Dec 6	
	B	300.0	MLO	1991 Dec 1	1,6
	V	150.0	MLO[a]	1993 Nov 7	1,6
	R	60.0	KPNO	1991 Mar 12	6
	Hα	2040.0	KPNO	1991 Mar 12	7
NGC 1275...	B1	563.5	0464f	1990 Dec 9	
	A1	564.5	0384f[a]	1990 Dec 9	
	B	900.0	KPNO	1991 Mar 8	1[b]
	V	900.0	KPNO	1991 Mar 8	1[b]
	R	180.0	KPNO	1991 Mar 13	1[b]
NGC 1316...	B1	545.5	0533f	1990 Dec 10	
	A1	545.5	0425f	1990 Oct 12	
	B	300.0	CTIO	1991 Dec 6	1
	V	180.0	CTIO	1991 Dec 6	1
	R	180.0	CTIO	1991 Dec 6	1
	Hα	600.0	CTIO	1991 Dec 6	NC[c]
NGC 1317...	B1	545.5	0533f	1990 Dec 10	
	A1	545.5	0425f	1990 Oct 12	
	B	600.0	CTIO	1991 Dec 10	1[b]
	V	600.0	CTIO	1991 Dec 10	1[b]
	R	180.0	CTIO	1991 Dec 6	1[b]
	Hα	900.0	CTIO	1991 Dec 11	8
NGC 1399...	B1	1454.5	0232f	1990 Dec 7	
	A1	1099.5	0216f	1990 Dec 7	
	B	300.0	MLO	1990 Jul 19	1[b]
	V	600.0	MLO	1991 Feb 18	1,9
	R	300.0	MLO	1990 Jul 19	1,9[b]
NGC 1404...	B1	1454.5	0232f	1990 Dec 7	
	A1	1099.5	0216f	1990 Dec 7	
NGC 2146...	B5	443.5	0545f[a]	1990 Dec 10	
	A1	442.5	0437f	1990 Oct 12	
	B	300.0	KPNO	1991 Dec 1	1
	R	180.0	KPNO	1991 Dec 1	1
	Hα	600.0	KPNO	1991 Dec 31	7,10

NGC 2992...	B1	256.5	0097f	1990 Dec 5	
	A1	256.5	0090f	1990 Dec 5	
	B	300.0	KPNO	1991 Dec 9	1
	V	600.0	CTIO	1991 Dec 9	1
	R	600.0	CTIO	1991 Dec 9	1
	Hα	1800.0	CTIO	1991 Dec 9	11
NGC 2993...	B1	256.5	0097f	1990 Dec 5	
	A1	256.5	0090f	1990 Dec 5	
	B	300.0	KPNO	1991 Dec 9	1
	V	600.0	CTIO	1991 Dec 9	1
	R	600.0	CTIO	1991 Dec 9	1[b]
	Hα	1800.0	CTIO	1991 Dec 9	11
NGC 3031...	B1	640.5	0556f	1990 Dec 10	
	A1	639.5	0442f	1990 Oct 12	
	B	600.0	KPNO	1993 Dec 8	1
	V	600.0	KPNO	1991 Mar 8	1
	R	300.0	KPNO[a]	1990 May 27	1
	Hα	600.0	KPNO	1991 Apr 13	12
NGC 3034...	B1	270.5	0204f[a]	1990 Dec 6	
	A1	270.5	0194f	1990 Dec 6	
	B	600.0	MLO	1991 Feb 19	13
	V	600.0	KPNO	1991 Mar 9	13
	R	300.0	MLO[a]	1991 May 12	13
	Hα	1200.0	MLO	1991 May 12	14
UGC 5336...	B1	640.5	0556f	1990 Dec 10	
	A1	639.5	0442f	1990 Oct 12	
	B	600.0	KPNO	1993 Dec 8	1[b]
	R	300.0	KPNO[a]	1990 May 27	1[b]
UGC 6697...	B5	529.5	0193f	1990 Dec 6	
	A1	105.5	0184f	1990 Dec 6	
	B	300.0	KPNO	1992 Jan 1	1[b]
	R	180.0	KPNO	1992 Jan 1	1[b]
NGC 4151...	B5	1199.5	0337f[a]	1990 Dec 8	
	A1	293.5	0295f[a]	1990 Dec 8	
	B	300.0	KPNO	1990 Jun 1	1[b]
	V	600.0	KPNO	1991 Mar 8	1[b]
	R	180.0	KPNO	1990 Jun 1	1
	Hα	3600.0	KPNO	1991 Mar 8	NC
NGC 4321...	B5	226.5	0166f	1990 Dec 6	
	A5	226.5	0157f	1990 Dec 6	
	B	600.0	KPNO	1991 Mar 12	1,15
	V	300.0	KPNO	1991 Mar 12	1,15
	R	180.0	KPNO	1992 Jan 2	1,15
	Hα	600.0	KPNO	1992 Jan 2	16

Secondary Objects

Mrk 335...	B1	286.5	0507f[a]	1990 Dec 10	
	A1	294.5	0410f[a]	1990 Dec 10	
NGC 891...	B5	437.5	0358f[a]	1990 Dec 8	
	A1	437.5	0307f	1990 Dec 8	
	R	300.0	MLO	1992 Aug 23	NC
	Hα	600.0	MLO	1993 Dec 6	10
NGC 1267...	B1	563.5	0464f	1990 Dec 9	
	A1	564.5	0384f[a]	1990 Dec 9	
NGC 1268...	B1	563.5	0464f	1990 Dec 9	
	A1	564.5	0384f[a]	1990 Dec 9	
NGC 1270...	B1	563.5	0464f	1990 Dec 9	
	A1	564.5	0384f[a]	1990 Dec 9	
	B	900.0	KPNO	1991 Mar 8	1
	V	900.0	KPNO	1991 Mar 8	1
	R	180.0	KPNO	1991 Mar 13	1[b]
NGC 1272...	B1	563.5	0464f	1990 Dec 9	
	A1	564.5	0384f[a]	1990 Dec 9	
	B	900.0	KPNO	1991 Mar 8	1
	V	900.0	KPNO	1991 Mar 8	1[b]
	R	180.0	KPNO	1991 Mar 13	1[b]
NGC 1273...	B1	563.5	0464f	1990 Dec 9	
	A1	564.5	0384f[a]	1990 Dec 9	
	B	900.0	KPNO	1991 Mar 8	1
	V	900.0	KPNO	1991 Mar 8	1
	R	180.0	KPNO	1991 Mar 13	1[b]
UGC 2665...	B1	563.5	0464f	1990 Dec 9	
	A1	564.5	0384f[a]	1990 Dec 9	
	B	900.0	KPNO	1991 Mar 8	1[b]
	V	900.0	KPNO	1991 Mar 8	1[b]
NGC 1277...	B1	563.5	0464f	1990 Dec 9	
	A1	564.5	0384f[a]	1990 Dec 9	
	B	900.0	KPNO	1991 Mar 8	1
	V	900.0	KPNO	1991 Mar 8	1
	R	180.0	KPNO	1991 Mar 13	1[b]
NGC 1278...	B1	563.5	0464f	1990 Dec 9	
	A1	564.5	0384f[a]	1990 Dec 9	
	B	900.0	KPNO	1991 Mar 8	1
	V	900.0	KPNO	1991 Mar 8	1
	R	180.0	KPNO	1991 Mar 13	1[b]
NGC 1282...	B1	563.5	0464f	1990 Dec 9	
	A1	564.5	0384f[a]	1990 Dec 9	
	B	900.0	KPNO	1991 Mar 8	1
	V	900.0	KPNO	1991 Mar 8	1
	R	180.0	KPNO	1991 Mar 13	1
NGC 1396...	B1	1454.5	0232f	1990 Dec 7	
	A1	1099.5	0216f	1990 Dec 7	

NGC 2551...	B1	454.5	0451f[a]	1990 Dec 9	
	A1	454.5	0380f	1990 Dec 9	
NGC 3837...	B5	529.5	0193f	1990 Dec 6	
	A1	105.5	0184f	1990 Dec 6	
	B	300.0	KPNO	1992 Jan 1	1
	R	180.0	KPNO	1992 Jan 1	1[b]
MCG 3 30 71...	B5	529.5	0193f	1990 Dec 6	
	A1	105.5	0184f	1990 Dec 6	
	B	300.0	KPNO	1992 Jan 1	1[b]
	R	180.0	KPNO	1992 Jan 1	1[b]
NGC 3842...	B5	529.5	0193f	1990 Dec 6	
	A1	105.5	0184f	1990 Dec 6	
	B	300.0	KPNO	1992 Jan 1	1
	R	180.0	KPNO	1992 Jan 1	1[b]
CGCG 97 114...	B5	529.5	0193f	1990 Dec 6	
	A1	105.5	0184f	1990 Dec 6	
NGC 4156...	B5	1199.5	0337f[a]	1990 Dec 8	
	A1	293.5	0295f[a]	1990 Dec 8	
	B	300.0	KPNO	1990 Jun 1	1
	V	600.0	KPNO	1991 Mar 8	1
	R	180.0	KPNO	1990 Jun 1	1[b]
	Hα	3600.0	KPNO	1991 Mar 8	NC
UGC 7188...	B5	1199.5	0337f[a]	1990 Dec 8	
	A1	293.5	0295f[a]	1990 Dec 8	
	B	300.0	KPNO	1990 Jun 1	1[b]
	V	600.0	KPNO	1991 Mar 8	1[b]
	R	180.0	KPNO	1990 Jun 1	1[b]
	Hα	3600.0	KPNO	1991 Mar 8	NC
NGC 4470...	B5	180.5	0415f	1990 Dec 9	
	A5	180.5	0338f	1990 Dec 9	
NGC 4472...	B5	180.5	0415f	1990 Dec 9	
	A5	180.5	0338f	1990 Dec 9	
NGC 4476...	B5	352.5	0125f	1990 Dec 5	
	A1	70.5	0113f	1990 Dec 5	
NGC 4478...	B5	352.5	0125f	1990 Dec 5	
	A1	70.5	0113f	1990 Dec 5	
NGC 4486...	B5	352.5	0125f	1990 Dec 5	
	A1	70.5	0113f	1990 Dec 5	
	B	300.0	MLO	1991 Feb 4	1,17,18,19
	V	300.0	MLO	1991 Nov 5	1,17,18,19,20
	R	300.0	MLO[a]	1991 Nov 5	1,21,22

Notes. - Col. (1): Galaxy identification. Col. (2): Filter used for this observation. Col. (3): Exposure time in seconds. Col. (4): For UIT data this column lists the assigned UIT image frame number from which the photometry was derived (See Section 4.2 for details). These frame numbers can be used to access the UIT data from the *HST* multimission archive. For optical band imagery, this column lists the source of the data. Col. (5): Date of observation. Col. (6): Literature reference to the published data that was used to bootstrap the calibration of the optical photometry presented in this paper.

[a] Indicates images which have been co-added with other exposures of the same target.

[b] Due to lack of reliable data, this galaxy was calibrated based on an average of other galaxies in the field. (See Section 4.6 for discussion).

[c] Data are not calibrated.

References. -(1) Prugniel & Heraudeau 1998; (2) using spectrophotometric standard star Feige 34 (Stone 1977) ; (3) Frogel 1985; (4) Elmegreen 1980; (5) Kennicutt & Hodge 1980; (6) Schild et al. 1985; (7) Young et al. 1988; (8) Crocker et al. 1996; (9) Mackie et al. 1990; (10) Smith & Harvey 1996; (11) Usui et al. 1998; (12) Hill et al. 1995a; (13) using standard star field; (14) O'Connell & Mangano 1978; (15) de Jong & van der Kruit 1994, with applied systematic offsets given by Prugniel & Heraudeau 1998; (16) Kennicutt & Kent 1983; (17) Goudfrooij et al. 1994, with applied systematic offsets given by Prugniel & Heraudeau 1998; (18) Michard 1982, with applied systematic offsets given by Prugniel & Heraudeau 1998; (19) Poulain 1983, private communication, with applied systematic offsets given by Prugniel & Heraudeau 1998; (20) Aaronson & Mould 1981, with applied systematic offsets given by Prugniel & Heraudeau 1998; (21) Djorgovski 1985, with applied systematic offsets given by Prugniel & Heraudeau 1998; (22) Peletier et al. 1990, with applied systematic offsets given by Prugniel & Heraudeau 1998

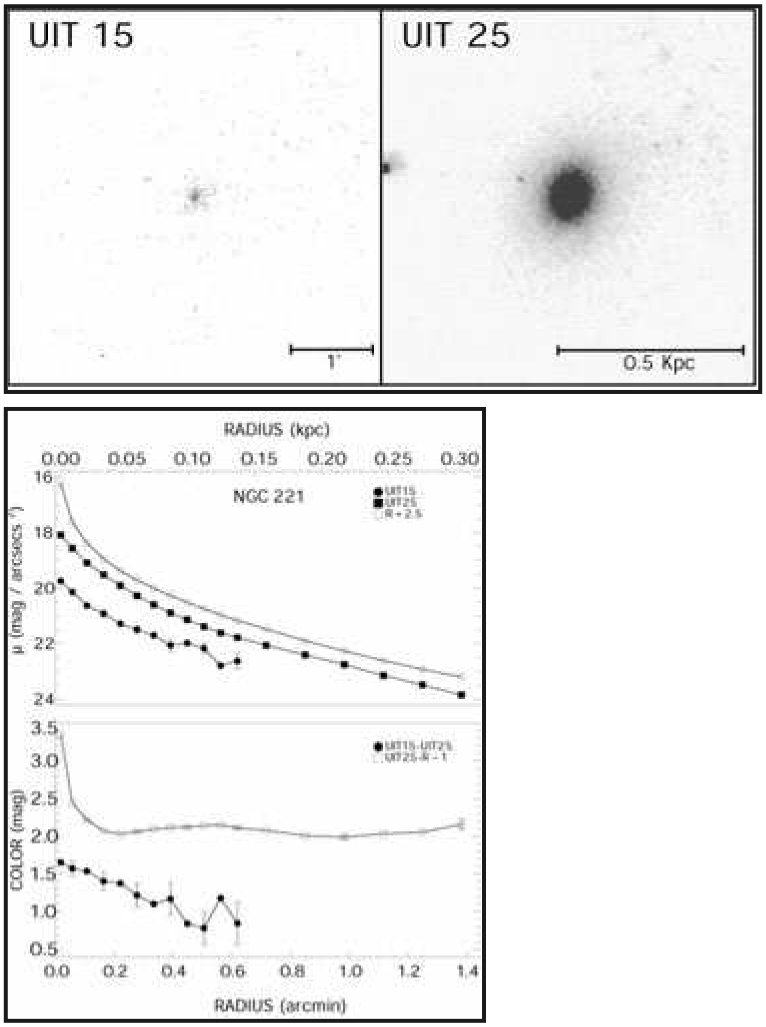

Figure 4. (*a*) UV images for NGC 221 (M32). Surface brightness and color profiles show 1σ error bars in this and all proceeding surface brightness and color profiles (for inner radii, the error bars are smaller than the symbol sizes). (*b*) UV/optical extinction-corrected radial surface brightness (*upper*) and color (*lower*) profiles for NGC 221. Note that offsets (given in the legend) have been applied. The *R*-band data are from Kent (1987).

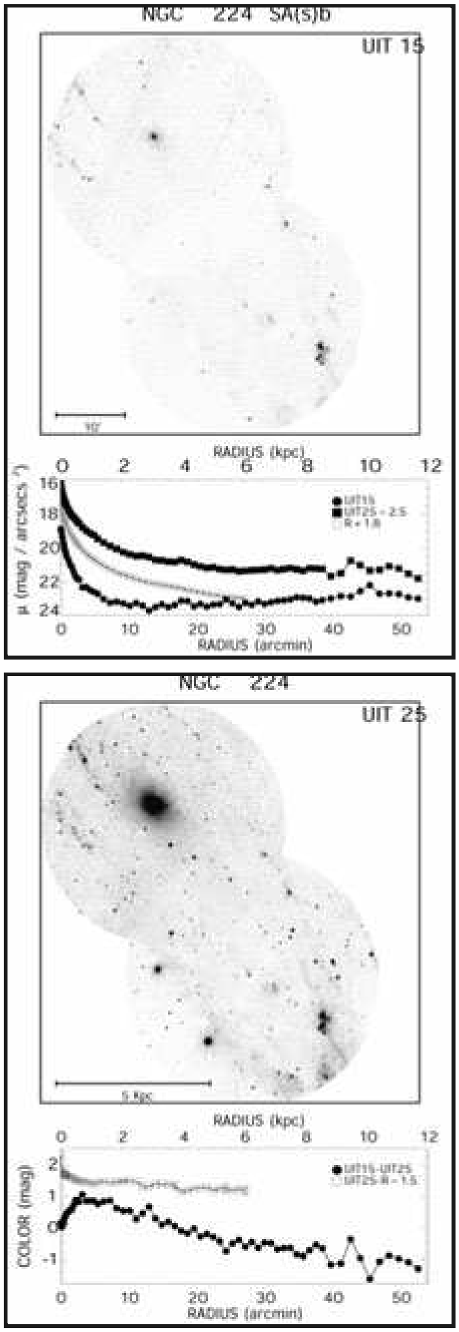

Figure 5. (*a*) *Upper panel*: FUV mosaic of NGC 224 (M31). *Lower panel*: UV and *R*-band (from Kent 1987) extinction-corrected radial surface brightness profiles. Note that offsets (given in the legend) have been applied. (*b*) *Upper panel* : MUV mosaic of NGC 224. *Lower panel*: UV and *R* -band extinction-corrected color profiles. Note that offsets (given in the legend) have been applied.

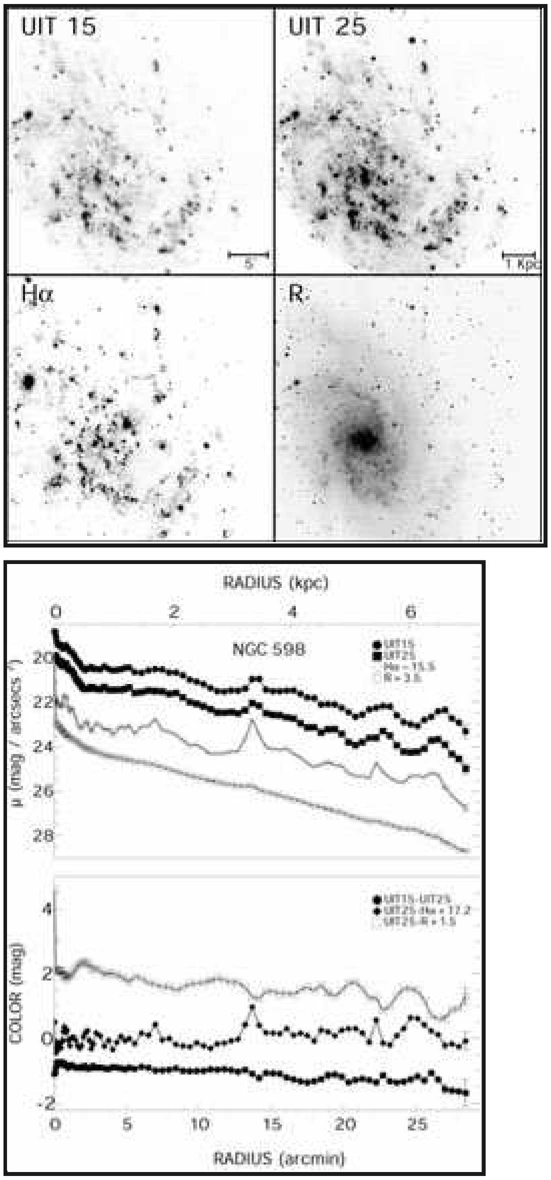

Figure 6. (*a*) UV and optical images for NGC 598 (M33). (*b*) UV/optical extinction-corrected radial surface brightness (*upper*) and color (*lower*) profiles for NGC 598. Note that offsets (given in the legend) have been applied. The Hα data are presented as -2.5 $\log_{10}(f)$, where *f* is in units ergs s^{-1} cm^{-2} $arcsec^{-2}$.

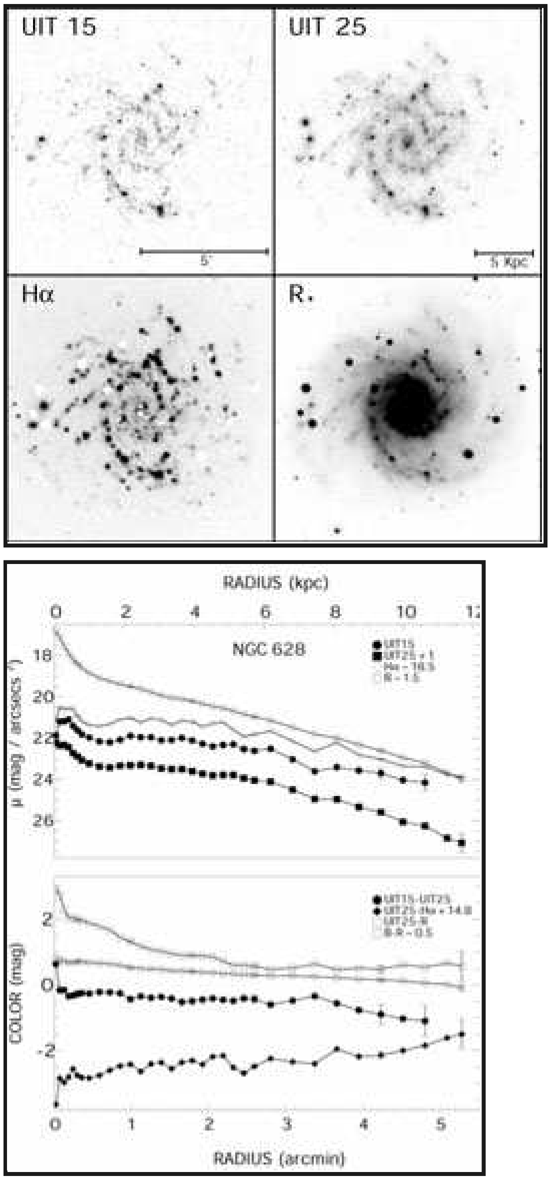

Figure 7. (*a*) UV and optical images for NGC 628 (M74). (*b*) UV/optical extinction-corrected radial surface brightness (*upper*) and color (*lower*) profiles for NGC 628. Note that offsets (given in the legend) have been applied. The Hα data are presented as -2.5 $\log_{10}(f)$, where f is in units ergs s^{-1} cm^{-2} $arcsec^{-2}$.

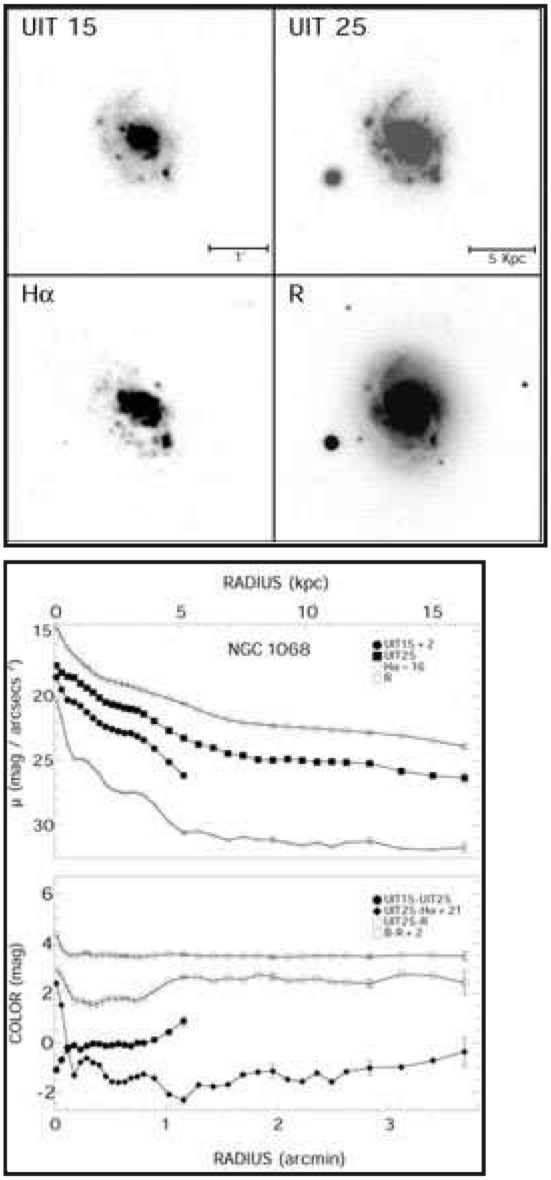

Figure 8. (*a*) UV and optical images for NGC 1068 . (*b*) UV/optical extinction-corrected radial surface brightness (*upper*) and color (*lower*) profiles for NGC 1068. Note that offsets (given in the legend) have been applied. The H α data are presented as -2.5 $\log_{10}(f)$, where *f* is in units ergs s^{-1} cm^{-2} $arcsec^{-2}$.

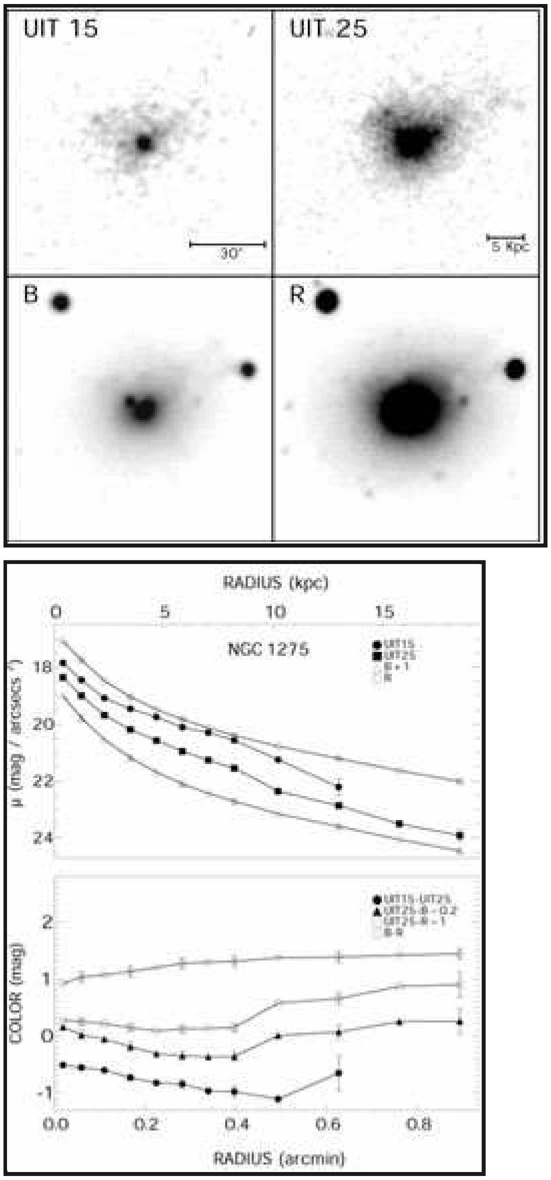

Figure 9. (*a*) UV and optical images for NGC 1275 . (*b*) UV/optical extinction-corrected radial surface brightness (*upper*) and color (*lower*) profiles for NGC 1275. Note that offsets (given in the legend) have been applied.

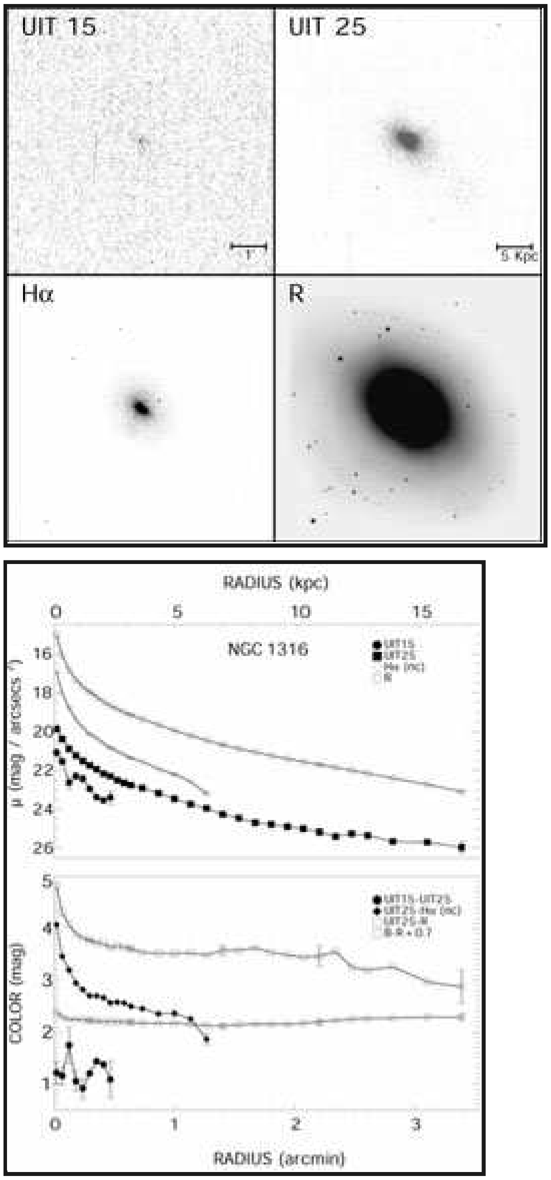

Figure 10. (*a*) UV and optical images for NGC 1316 . (*b*) UV/optical extinction-corrected radial surface brightness (*upper*) and color (*lower*) profiles for NGC 1316 . Note that the H α is uncalibrated, and therefore presented in relative magnitudes.

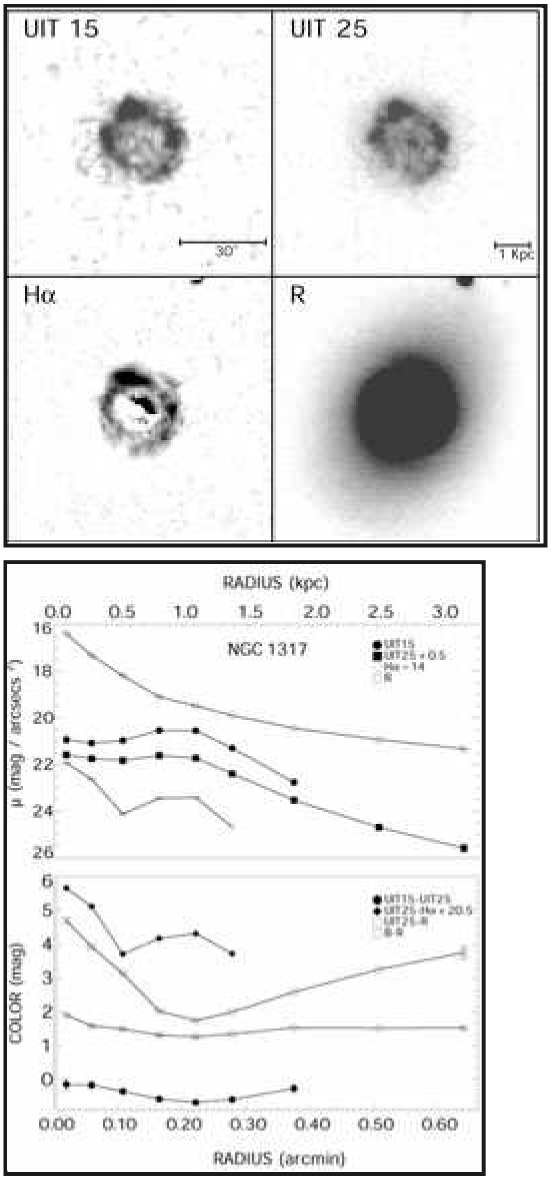

Figure 11. (*a*) UV and optical images for NGC 1317 . (*b*) UV/optical extinction-corrected radial surface brightness (*upper*) and color (*lower*) profiles for NGC 1317. Note that offsets (given in the legend) have been applied. The H α data are presented as -2.5 $\log_{10}(f)$, where *f* is in units of ergs s^{-1} cm^{-2} $arcsec^{-2}$.

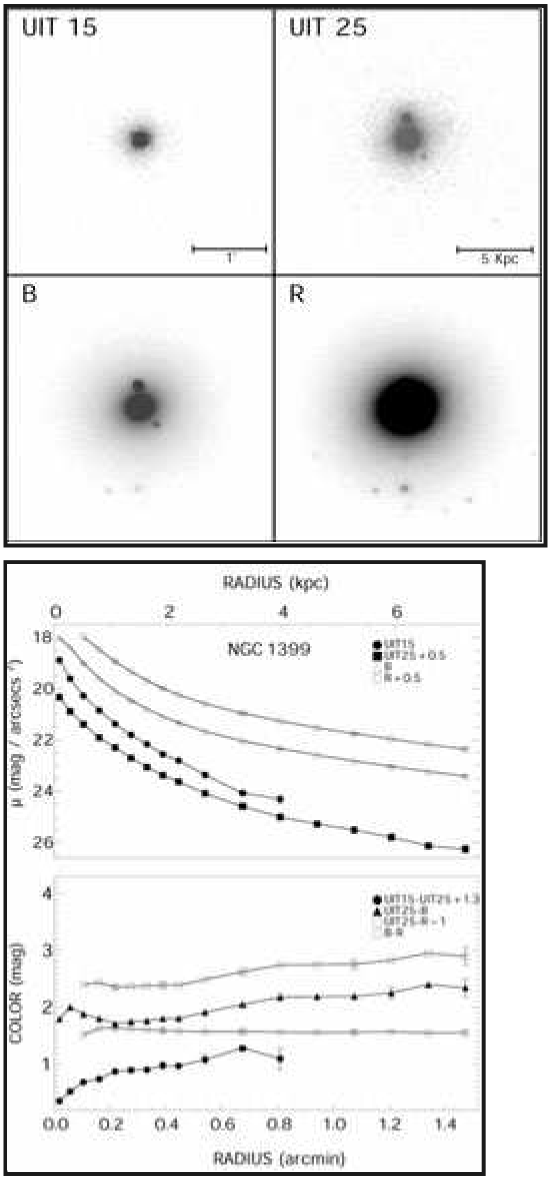

Figure 12. (*a*) UV and optical images for NGC 1399 . (*b*) UV/optical extinction-corrected radial surface brightness (*upper*) and color (*lower*) profiles for NGC 1399. Note that offsets (given in the legend) have been applied.

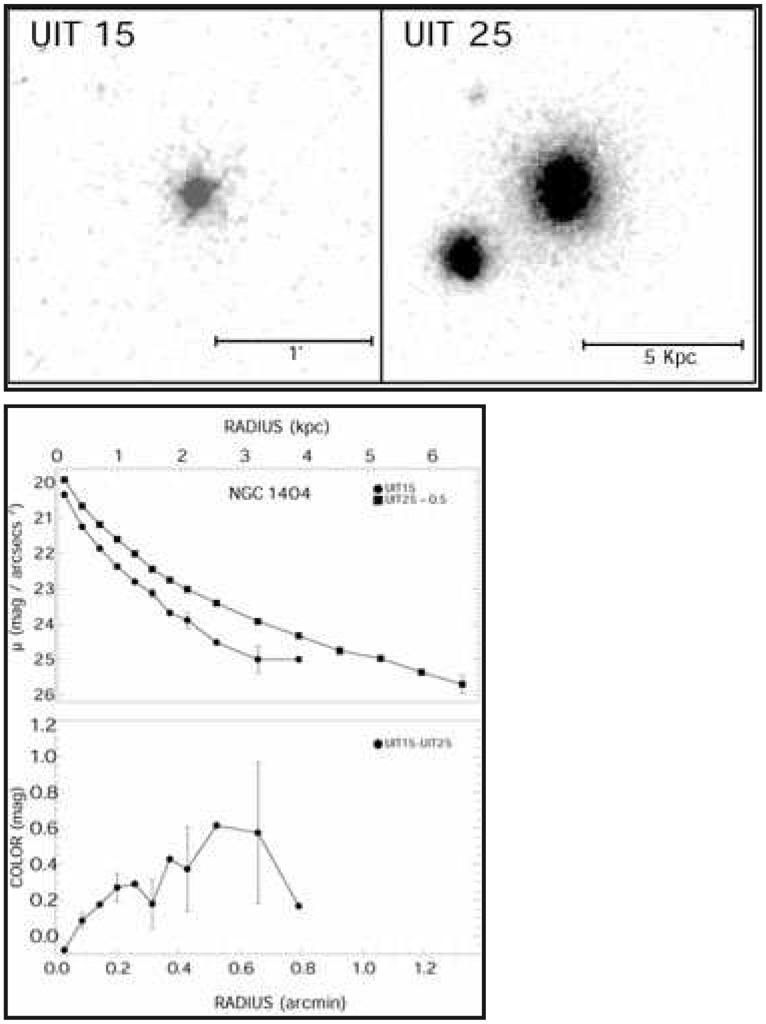

Figure 13. (*a*) UV images for NGC 1404 . (*b*) UV/optical extinction-corrected radial surface brightness (*upper*) and color (*lower*) profiles for NGC 1404.

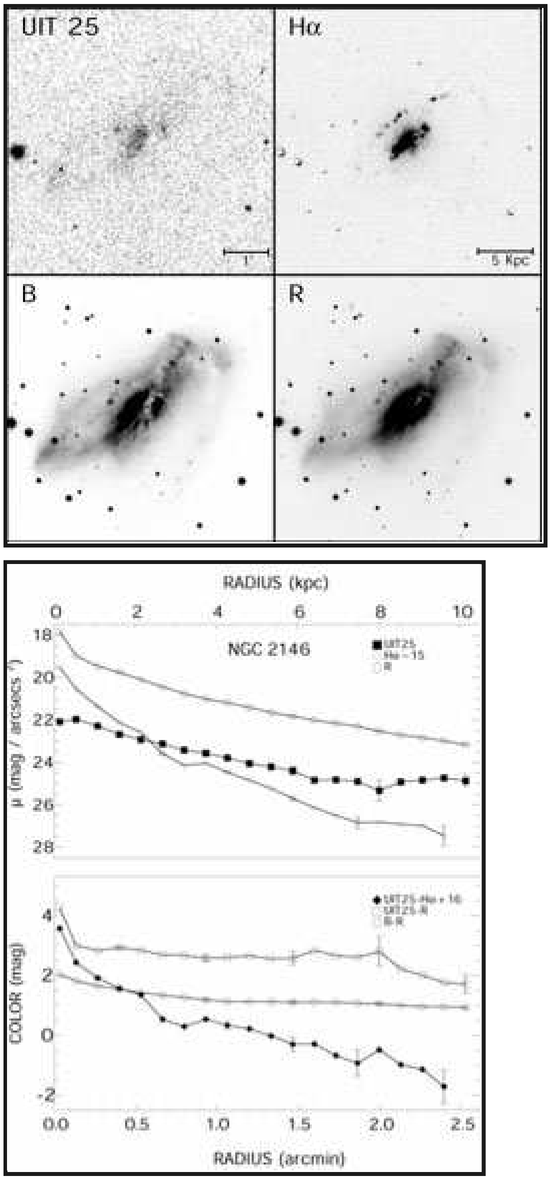

Figure 14. (*a*) UV and optical images for NGC 2146. (*b*) UV/optical extinction-corrected radial surface brightness (*upper*) and color (*lower*) profiles for NGC 2146. Note that offsets (given in the legend) have been applied.

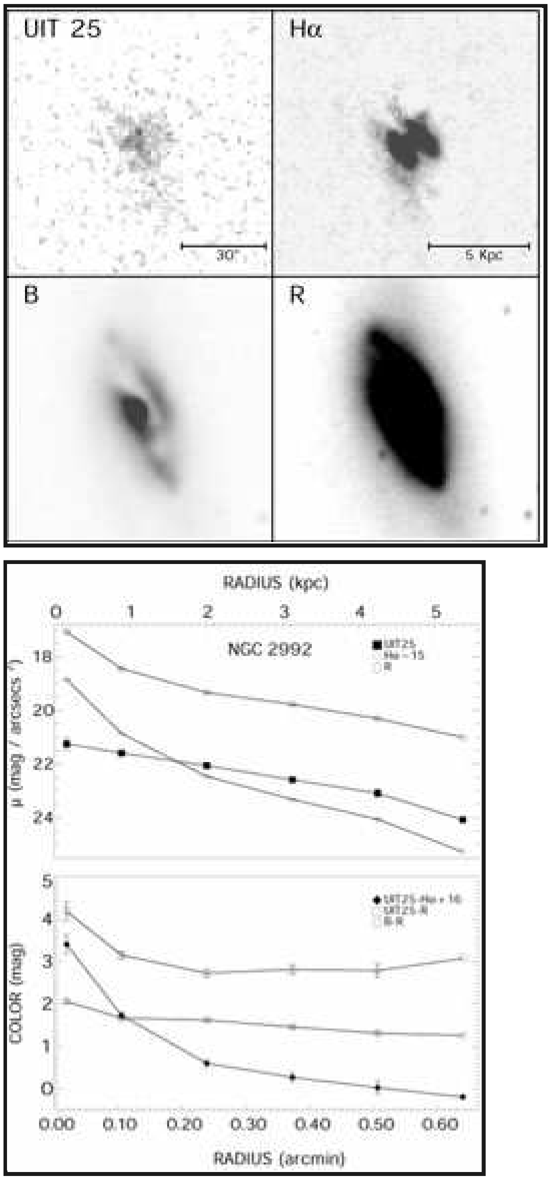

Figure 15. (*a*) UV and optical images for NGC 2992, an interacting galaxy with NGC 2993. (*b*) UV/optical extinction-corrected radial surface brightness (*upper*) and color (*lower*) profiles for NGC 2992. Note that offsets (given in the legend) have been applied. The Hα data are presented as -2.5 $\log_{10}(f)$, where f is in units ergs s^{-1} cm^{-2} $arcsec^{-2}$.

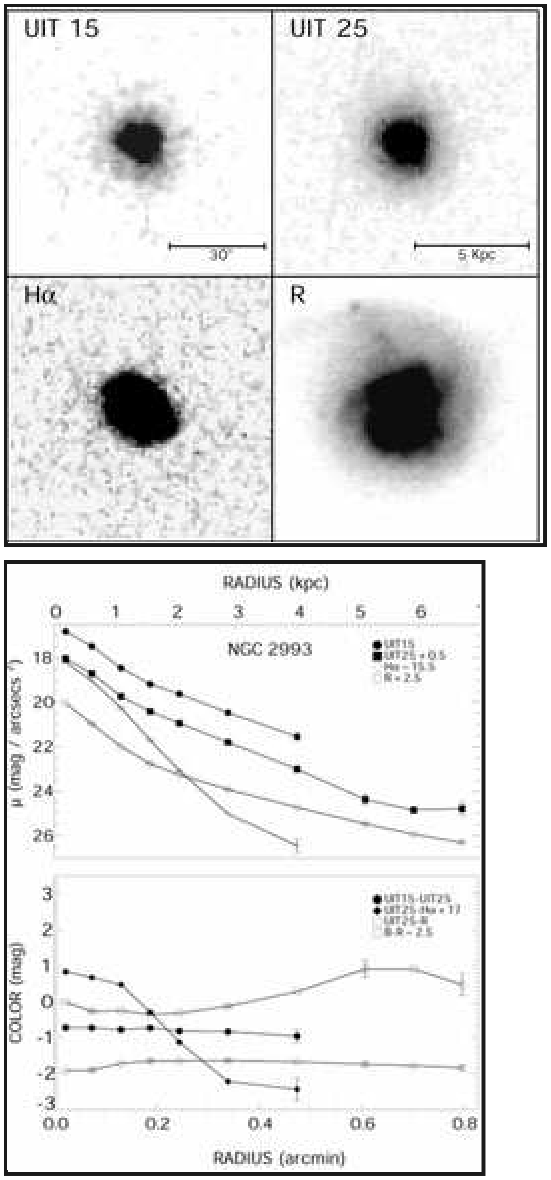

Figure 16. (*a*) UV and optical images for NGC 2993, an interacting galaxy with NGC 2992. (*b*) UV/optical extinction-corrected radial surface brightness (*upper*) and color (*lower*) profiles for NGC 2993. Note that offsets (given in the legend) have been applied. The Hα data are presented as -2.5 $\log_{10}(f)$, where f is in units ergs s^{-1} cm^{-2} $arcsec^{-2}$.

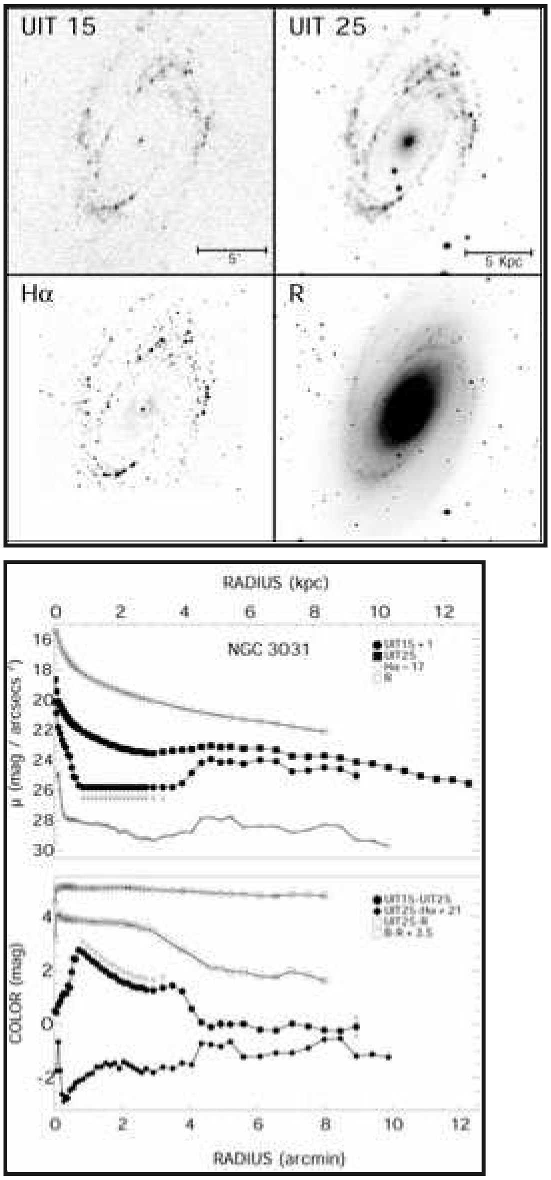

Figure 17. (*a*) UV and optical images for NGC 3031 (M81). (*b*) UV/optical extinction-corrected radial surface brightness (*upper*) and color (*lower*) profiles for NGC 3031.

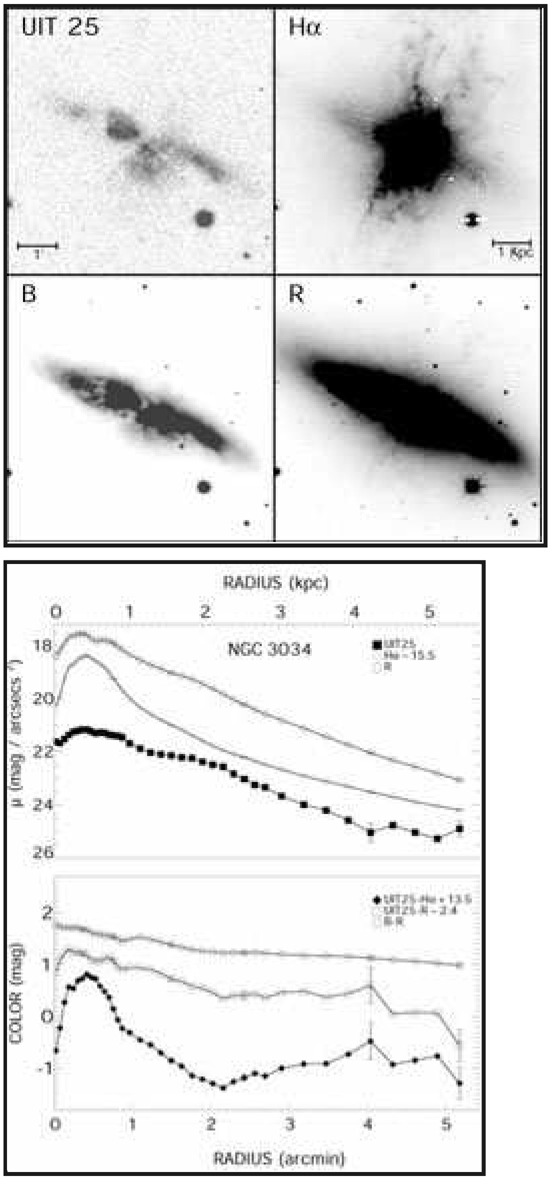

Figure 18. (*a*) UV and optical images for NGC 3034 (M82). (*b*) UV/optical extinction-corrected radial surface brightness (*upper*) and color (*lower*) profiles for NGC 3034. Note that offsets (given in the legend) have been applied. The Hα data are presented as -2.5 $\log_{10}(f)$, where f is in units ergs s^{-1} cm^{-2} $arcsec^{-2}$.

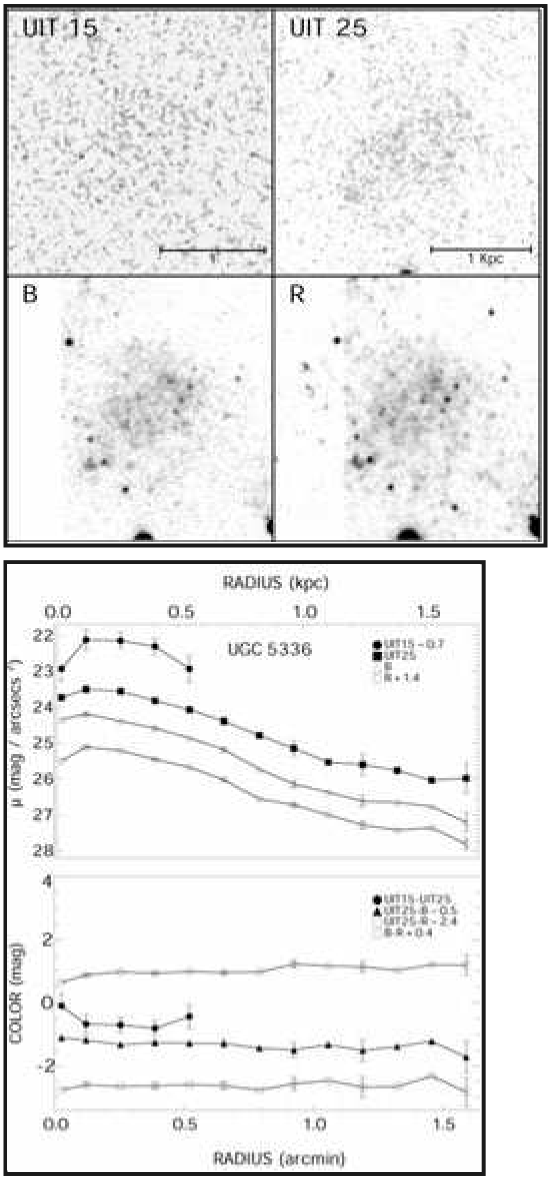

Figure 19. (*a*) UV and optical images for UGC 5336 . (*b*) UV/optical extinction-corrected radial surface brightness (*upper*) and color (*lower*) profiles for UGC 5336. Note that offsets (given in the legend) have been applied.

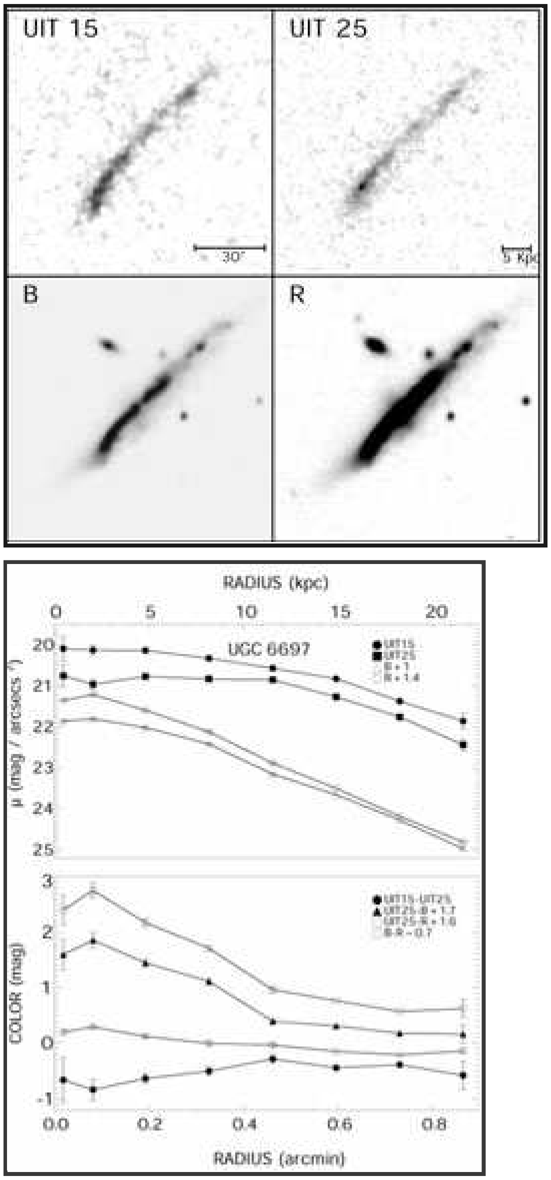

Figure 20. (*a*) UV and optical images for UGC 6697 . (*b*) UV/optical extinction-corrected radial surface brightness (*upper*) and color (*lower*) profiles for UGC 6697. Note that offsets (given in the legend) have been applied.

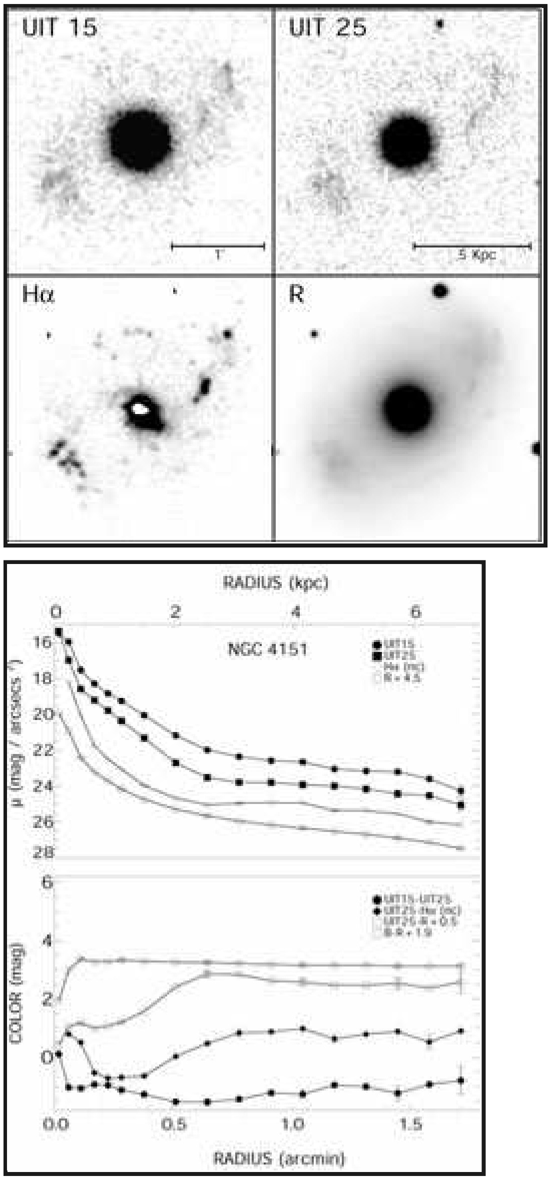

Figure 21. (*a*) UV and optical images for NGC 4151 . (*b*) UV/optical extinction-corrected radial surface brightness (*upper*) and color (*lower*) profiles for NGC 4151. Note that offsets (given in the legend) have been applied and that the H α data, which is uncalibrated, is presented in relative magnitudes.

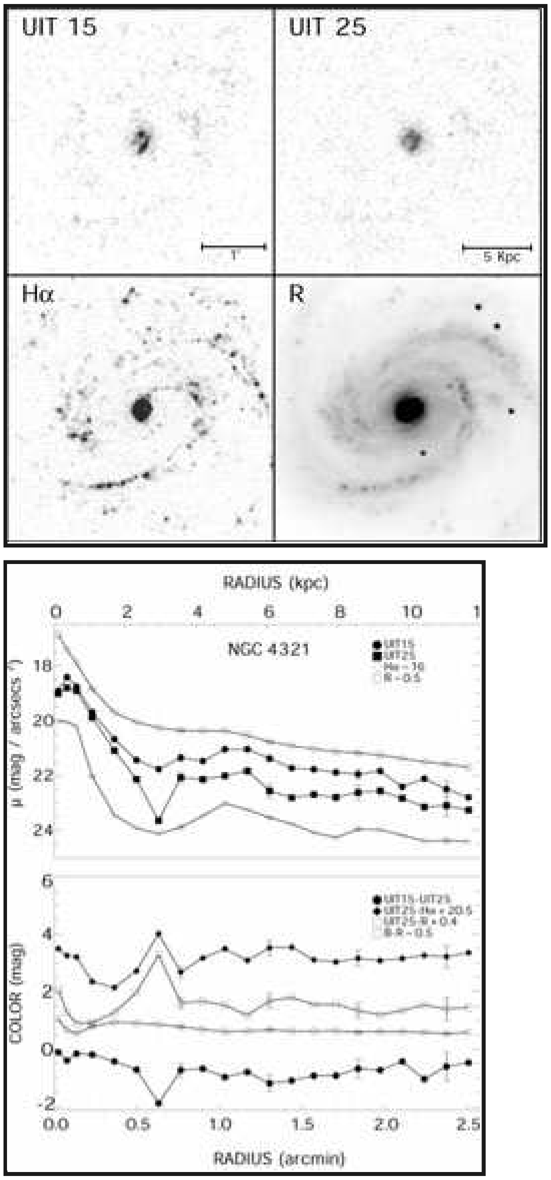

Figure 22. (*a*) UV and optical images for NGC 4321 . (*b*) UV/optical extinction-corrected radial surface brightness (*upper*) and color (*lower*) profiles for NGC 4321. Note that offsets (given in the legend) have been applied. The H α data are presented as -2.5 $\log_{10}(f)$, where f is in units ergs s^{-1} cm^{-2} $arcsec^{-2}$.

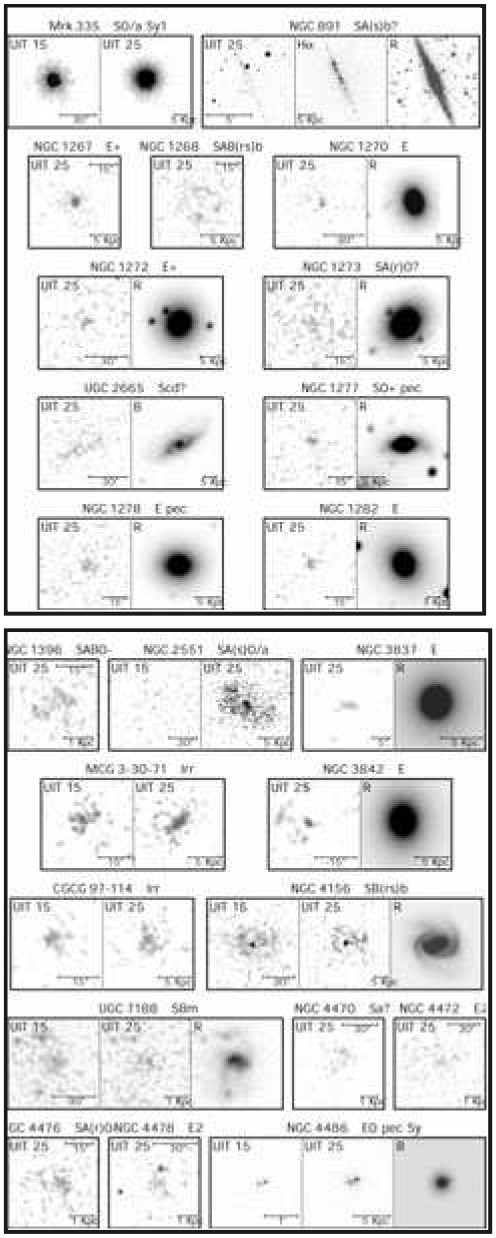
Mrk 335 S0/a Sy1
NGC 891 SA(s)b?
NGC 1267 E+
NGC 1268 SAB(rs)b
NGC 1270 E
NGC 1272 E+
NGC 1273 SA(r)0?
UGC 2665 Scd?
NGC 1277 S0+ pec
NGC 1278 E pec
NGC 1282 E
NGC 1396 SAB0-
NGC 2551 SA(s)0/a
NGC 3837 E
MCG 3-30-71 Irr
NGC 3842 E
CGCG 97-114 Irr
NGC 4156 SB(rs)b
UGC 7188 SBm
NGC 4470 Sa?
NGC 4472 E2
NGC 4476 SA(r)0
NGC 4478 E2
NGC 4486 E0 pec Sy
UIT 15
UIT 25
Hα
R
B
5 Kpc
1 Kpc
30"
15"
5"

Figure 23. UV and optical (where available) images for "secondary" objects.

Some Astro-1 images were affected by thin (a few pixels) linear scratches, apparently on the emulsion surface, which occurred during the digitalization process. These artifacts have been treated by replacing the affected pixels with values determined by linear interpolation from neighboring pixels. Astro-2 images (see Kuchinski et al. 2000) are not similarly affected.

4.3. Flux Calibration and Error Analysis

UIT noise characteristics have been determined from repeated measurements of the pixel values in laboratory flat fields (see Stecher et al. 1997 for full details). The resulting noise/signal ratio is relatively small (15%-20% for single pixels and 5% for regions several arcseconds in size) over the center of the dynamic range, with substantial increases ($\lesssim$ 40%) at the extremes. The photometric uncertainties reported in the tables here combine the estimated variances for all pixels in a given measuring aperture in quadrature, treating source pixels and sky as independent contributors to uncertainty in the flux values.

Absolute flux calibration of UIT was determined by comparing photometry of stars from selected UIT frames with photometry from *IUE*, HUT, ANS, GHRS, and other UV instruments. The primary calibration is based on isolated stars observed in common with *IUE*. Typical uncertainties in absolute fluxes for UIT sources with good exposure were determined to be ~ 15% (Stecher et al. 1997).

The majority of the ground-based images were taken under nonphotometric sky conditions. Broadband optical images in the *BVR* bands were calibrated by comparison to a compilation of published aperture and CCD photometry as given by Prugniel & Heraudeau (1998). All *R*-band data given in this atlas are based on the Cousins *R* (Bessell 1986) photometric system. Additional sources were used to flux calibrate the Hα and some *R*-band images. For the broadband data, calibration scaling factors were derived from the mean offset (in magnitudes) between all available photometry and instrumental values determined for matching apertures. Offsets obtained in this manner inherently account for air mass corrections, color terms (for that particular object), and instrumental corrections. We note that foreground stars were masked out during computation of the photometry presented in this paper. To derive a calibration by comparison to published values, instrumental magnitudes were computed without masking foreground stars, on the assumption that the literature values were derived in this manner. References and methods used to calibrate the optical data are given in column (6) of Table 4. Uncalibrated data are indicated as "NC" in the table.

Continuum-free Hα images were obtained by subtracting a scaled *R*-band image from a narrowband image centered on Hα. Unsaturated stars common to both images were used to determine the scaling factor applied to the *R*-band image. Published Hα aperture photometry was then used to derive an absolute calibration for the pure emission line image. The narrowband filters used for the Hα data presented in the atlas included possible [N II] emission; no correction has been applied for this. However, most of the references used to determine absolute calibrations also included [N II], so the calibrations should be consistent. Hα fluxes are given in units of ergs s^{-1} cm^{-2}.

The optical photometry presented here has typical uncertainties of $\leq$ 0.05 mag. The Hα data have a somewhat large uncertainty (~ 10%-30%), due to the limited published photometry available for calibration and to uncertainties in continuum subtraction. For a few objects we could not locate any existing published data of suitable accuracy, and these images lack calibrated zero points. Uncalibrated data are indicated in the tables and figures.

For images which contain multiple sources with published photometry in the same frame (e.g., the Perseus Cluster field), an average calibration was computed and applied to all galaxies in that image including those without existing photometry. Such galaxies have been flagged in Table 4 and have larger photometric uncertainties, since this method does not allow for individual color term corrections. We note that the lack of an absolute calibration does not affect the comparison between the *shapes* of the surface brightness profiles (Figs. 4*b* - 22*b*), or in certain derived photometric parameters such as half-light radii.

4.4. Image Atlas

This UV/optical atlas consists of images and associated radial light and color profiles. In Figures 4*a* - 22*a* we present the registered, multiband images of the primary targets; Figures 23*a* - 23*b* show thumbprints of UIT images for the secondary targets. Objects are presented in order of increasing right ascension. Where available, an Hα and *R*-band image are displayed for comparison to the FUV ("UIT 15") and MUV ("UIT 25") images. In cases where Hα is not available, or the galaxy does not appear as a source in the FUV image, a *B*-band and/or *V*-band image has been substituted. Images are oriented north-up, east-left, and all images for a specific galaxy are displayed with the same spatial scale. The adopted color tables and displayed intensity ranges have been optimized for each individual galaxy in order to emphasize extended, low surface brightness UV structure. Morphological types were obtained from the NASA/IPAC Extragalactic Database (NED) and the Third Reference Catalog of Bright Galaxies (de Vaucouleurs et al. 1991, hereafter RC3).

4.5. Photometry

In Figures 4*b* - 22*b* we present azimuthally averaged radial surface brightness and color profiles for the primary objects. The FUV, MUV, Hα, and *R*-band profiles are shown, where available. For objects lacking Hα data, *B*-band photometry has been substituted. Arrows on the data points, oriented in either an up or down direction, represent lower and upper limits, respectively. The Hα surface photometry is presented in magnitudes, defined by $-2.5 \log_{10}(f)$, where f is in units of ergs s^{-1} cm^{-2}. Surface brightness profiles which are uncalibrated are flagged in the legend with "NC." Photometric errors, representing 1 standard deviation, are indicated on the profiles, generally for the outermost points. For the larger galaxies in this sample, scaling of the profiles in Figures 4*b* - 22*b* precludes display of the detailed structure of the inner light profiles, but these data are available in Table 9 (see Appendix B). In most cases, the FWHM of the seeing disk for the optical data was smaller than the FWHM of the UIT data; this mismatch can produce spurious color gradients for $r \lesssim 5''$ in some sources.

For each primary object synthetic aperture photometry was performed using the calibrated, unregistered, artifact-corrected images. The photometry employed concentric fixed elliptical annuli centered on the peak emission determined from the *R*-band image (where available, or alternatively *B* band). The location of the central peak was typically in agreement with the position given in the RC3. The width of the annuli ranged from 28" (25 UIT pixels) for the outermost regions of the galaxies having the largest angular size, to a minimum of 3".3 (3 UIT pixels) for the innermost annuli. In order to include any possible extended low surface brightness structure around the objects, the outermost apertures were chosen to lie well beyond the D_{25} isophotal diameter given in the RC3. The derived light profiles were individually examined to determine the radius for which the surface brightness profile flattened to the background sky.

Aperture parameters were determined by fitting ellipses to the outer *R*-band (or *B*-band) isophotes for each object. The derived ellipticity and position angles for a given object were used to photometer all of the available bandpasses. For most objects, the adopted position angle and ellipticity closely agreed with values given in the RC3. Values for these parameters are presented in Table 5.

Table 5. Photometric Parameters

			FOREGROUND EXTINCTION						SKY (mag arcsec^{-2})	
OBJECT (1)	l(deg) (2)	b(deg) (3)	A_B (4)	A_{15} (5)	A_{25} (6)	$D_{25}/2$(arcsec) (7)	PA(deg) (8)	b/a (9)	μ_{15} (10)	μ_{25} (11)
Primary Objects										
NGC 221...	121.2	-22.0	0.33	0.67	0.58	261	170	0.7	22.0	24.1
NGC 224...	121.2	-21.6	0.33	0.67	0.58	5704	35	0.3	22.3[a]	25.4[a]
NGC 598...	133.6	-31.3	0.19	0.38	0.33	2119	23	0.6	22.3	24.7
NGC 628...	138.6	-45.7	0.13	0.26	0.23	313	25	0.9	23.9	24.5
NGC 1068...	172.1	-51.9	0.05	0.10	0.09	212	70	0.9	22.4	25.3
NGC 1275...	150.6	-13.3	0.75	1.51	1.31	65	110	0.8	23.3	25.4
NGC 1316...	240.2	-56.7	0.0	0.0	0.0	360	50	0.7	23.4	25.1
NGC 1317...	240.0	-56.7	0.0	0.0	0.0	82	78	0.9	23.5	25.3
NGC 1399...	236.7	-53.6	0.0	0.0	0.0	207	...	1.0	23.4	25.2
NGC 1404...	237.0	-53.6	0.0	0.0	0.0	99	...	1.0	23.5	25.5
NGC 2146...	135.7	24.9	0.33	0.67	0.58	180	135	0.6	24.0	25.8
NGC 2992...	249.7	28.8	0.27	0.54	0.47	106	15	0.3	22.3	26.0
NGC 2993...	249.8	28.8	0.27	0.54	0.47	40	95	0.7	22.1	25.4
NGC 3031...	142.1	40.9	0.16	0.32	0.28	806	157	0.5	24.4	25.8
NGC 3034...	141.4	40.6	0.13	0.26	0.23	336	65	0.4	24.2	24.7
UGC 5336...	142.0	41.1	0.16	0.32	0.28	75	...	1.0	26.3	25.3
UGC 6697...	234.1	73.0	0.0	0.0	0.0	56	137	0.2	22.5	$\lesssim 0$[b]
NGC 4151...	155.1	75.1	0.0	0.0	0.0	189	50	0.7	21.9	27.6
NGC 4321...	271.1	76.9	0.06	0.12	0.10	222	30	0.9	20.0	21.6
Secondary Objects										
Mrk 335...	108.8	-41.4	0.11	0.22	0.19	9	...	1.0	21.6	25.0
NGC 891...	140.4	-17.4	0.32	0.65	0.56	404	22	0.2	23.2	25.2
NGC 1267...	150.4	-13.4	0.75	1.51	1.31	33	...	1.0	22.7	24.8
NGC 1268...	150.4	-13.4	0.75	1.51	1.31	29	56	0.7	23.1	24.9
NGC 1270...	150.5	-13.4	0.75	1.51	1.31	44	15	0.8	23.0	25.1
NGC 1272...	150.5	-13.3	0.75	1.51	1.31	61	...	1.0	23.0	25.0
NGC 1273...	150.5	-13.3	0.75	1.51	1.31	33	...	1.0	22.9	25.3
UGC 2665...	150.5	-13.2	0.75	1.51	1.31	31	122	0.4	22.8	25.5
NGC 1277...	150.6	-13.2	0.75	1.51	1.31	29	...	1.0	22.9	25.1
NGC 1278...	150.6	-13.2	0.75	1.51	1.31	46	...	1.0	22.9	25.2
NGC 1282...	150.7	-13.3	0.75	1.51	1.31	42	25	0.8	23.2	25.4

NGC 1396...	236.7	-53.7	0.0	0.0	0.0	30	...	1.0	23.4	25.3
NGC 2551...	141.0	32.5	0.07	0.14	0.12	50	55	0.7	23.4	28.3
NGC 3837...	234.4	72.9	0.0	0.0	0.0	19	...	1.0	22.6	26.5
MCG 3-30-71...	234.8	72.9	0.0	0.0	0.0	26	...	1.0	23.2	26.5
NGC 3842...	234.3	73.0	0.0	0.0	0.0	42	5	0.7	23.1	25.2
CGCG 97-114...	235.1	73.0	0.0	0.0	0.0	3	...	1.0	22.6	24.6
NGC 4156...	154.8	75.0	0.0	0.0	0.0	42	...	1.0	21.9	26.2
UGC 7188...	154.7	75.2	0.0	0.0	0.0	31	...	1.0	22.1	24.4
NGC 4470...	287.0	70.0	0.0	0.0	0.0	39	0	0.7	19.1	21.1
NGC 4472...	286.9	70.2	0.0	0.0	0.0	306	155	0.8	19.1	21.4
NGC 4476...	283.1	74.4	0.10	0.20	0.17	51	25	0.7	22.9	22.8
NGC 4478...	283.4	74.4	0.10	0.20	0.17	57	140	0.9	22.6	22.3
NGC 4486...	283.8	74.5	0.0	0.0	0.0	249	...	1.0	22.3	22.1

Notes. - Col. (1): Galaxy identification. Col. (2): Galactic longitude (in units of degrees). Col. (3): Galactic latitude (in units of degrees). Col. (4): Foreground extinction in magnitudes in the *B* band taken from the RC3. All "0" entries are given as zero values in RC3. However, as for any value of A_B, there is an ~ 10% uncertainty in the corresponding UV extinctions. Col. (5): Foreground extinction in magnitudes in the UIT far-UV bandpass. Col. (6): Foreground extinction in magnitudes in the UIT mid-UV bandpass. Derivation of extinction corrections in the UV bands are described in Section 4.5. Col. (7): Major axis radius at the 25th mag arcsec^{-2} *B*-band isophote, obtained from the RC3, in units of arcsec. Col. (8): Position angle adopted for the annular photometry, as described in Section 4.5. No value is given for circular annuli. Col. (9): Minor-to-major axis ratio adopted for the annular photometry, as described in Section4.5. Col. (10): Sky background determined for the FUV photometry, as described in Section4.5. The corresponding background flux was subtracted from the annular photometry. Col. (11): Sky background determined for the MUV photometry.

[a] Because the galaxy completely filled the frame, this value (as well as the associated photometry) is questionable.

[b] The background surrounding this galaxy has a local negative value, therefore no surface brightness value is given.

Accurate determination of background corrections for the UV photometry is crucial, as the UV background is a function of position in the UIT images and can vary as much as 40% across the image. Background values were determined by taking a sigma-clipped mean value of sky pixels within an irregular polygonal region surrounding each galaxy. The derived backgrounds are presented in Table 5. A detailed discussion of the systematics and origin of the UV sky background as measured from UIT images is given by Waller et al. (1995).

In the case of M31, which completely fills the frame, a background surface brightness of 25.4 mag arcsec^{-2} was adopted for the MUV image. This value was determined by interpolation of UIT MUV sky backgrounds present at other nearby locations (Waller et al. 1995). However, a similar approach for the FUV images, giving $\mu_{\rm FUV}$ = 23.3 mag arcsec^{-2}, resulted in an anomalously elevated light profile. A visual inspection of the image frame (Fig. 5*a*) shows that much of the galaxy away from the central region contains very little extended or diffuse UV emission. Therefore, the minima in the light profile of NGC 224 should be close to the limiting FUV surface brightness of ~ 24.5 mag arcsec^{-2} (for well-exposed images, as determined from light profiles of other UIT targets). We then forced the dimmest regions in the FUV surface brightness profile (uncorrected for extinction) to equal this limiting magnitude by using a FUV background of 22.3 mag arcsec^{-2}. Although this particular light profile has been adjusted in a somewhat arbitrary manner, the final adopted sky value is consistent with values derived for other UIT frames taken under similar observing conditions (see col. [10], Table 5).

Light from extragalactic sources is affected by foreground dust in the Milky Way. In Table 5 we list the foreground extinction values adopted in this paper. These were derived using the *B*-band extinctions values, A_b, given in the RC3 and the Cardelli et al. (1989, hereafter CCM) Galactic reddening law. The UIT filter functions were convolved with the CCM reddening law to derive extinction coefficients in the FUV and MUV bandpasses. We note that all extinction values in the FUV have intrinsic errors on the order of ~ 0.1 mag arising from uncertainties in the dust column along the line of sight. FUV extinctions are determined by $A_{1500} = k_\lambda \times E(B-V)$, where k_λ is the extinction law coefficient. For the CCM law, k_{1500} = 8.36. Therefore, an uncertainty of ±0.01-0.02 mag in $E(B-V)$, corresponds to an uncertainty of ~ 0.08-0.12 mag in A_{1500}. Even where the adopted

UV foreground extinction value is 0, residual extinction may still affect the source. In this Atlas, no corrections for extinction internal to the galaxies have been applied.

A complete tabulation of the aperture photometry for each primary object is given in Appendix B. Total integrated UV and optical magnitudes for all primary and secondary targets are listed in Table 6. Both apparent (first line) and absolute (second line) magnitudes are given for each galaxy. These magnitudes represent the total flux contained within a radius (col. [2]) at which the surface brightness profile flattens. Where we lacked optical imagery for a particular filter, a value was taken from Prugniel & Heraudeau (1998). These values are noted in the table and should be used with caution, since the literature photometry was not derived using the star masks employed in the atlas photometry. Columns (9)-(12) of Table 6 list the total UV to optical colors for each system (line 1). These values were constructed from the total integrated magnitudes. Column (13) is the ratio of FUV flux (ergs s^{-1} cm^{-2} $Å^{-1}$) to Hα flux (ergs s^{-1} cm^{-2}). All magnitudes and colors in Table 6 have been corrected for foreground dust extinction, using the extinction parameters given in Table 5. Uncalibrated data in Table 6 are indicated by footnotes. Associated 1 σ photometric uncertainties are given in parentheses.

Table 6. Integrated Ultraviolet/Optical Photometry

Object (1)	r (2)	$m(15)_0$ $M(15)_0$ (3)	$m(25)_0$ $M(25)_0$ (4)	$m(B)_0$ $M(B)_0$ (5)	$m(V)_0$ $M(V)_0$ (6)	$m(R)_0$ $M(R)_0$ (7)	$\log_{10} f(H\alpha)_0$ $\log_{10} L(H\alpha)_0$ (8)	$(15-25)_0$ (9)	$(25-R)_0$ (10)	$(B-V)_0$ (11)	$(B-R)_0$ (12)	$(f_{15}/f_{H\alpha})_0$[a] (13)
Primary Objects												
NGC 221...	86.9	12.98	11.31	...	...	...	...	1.67	...	...	...	...
		-11.43	-13.10	...	...	...	...	(0.08)	...	...	...	...
		(0.08)	(0.05)	...	...	...	...					
NGC 224...	3208	...[b]	...[b]	...	...	...	...	...[b]	...	...	...	...
NGC 598...	2033	4.91[c]	5.95[c]	6.10[d]	5.59[d]	5.82[c]	-9.22[c]	-1.04[c]	0.13[c]	0.51[d]	0.28[d]	0.066[c]
		-19.71[c]	-18.67[c]	-18.52[d]	-19.03[d]	-18.80[c]	16.29[c]	(0.06)	(0.05)	(0.05)	(0.05)	(0.004)
		(0.06)	(0.05)	(0.05)	(0.05)	(0.05)	(0.02)					
NGC 628...	349	9.43	9.90	9.89	9.36	8.97	-10.80	-0.47	0.93	0.53	0.92	0.039
		-19.97	-19.50	-19.52	-20.05	-20.44	15.67	(0.15)	(0.06)	(0.05)	(0.05)	(0.005)
		(0.15)	(0.05)	(0.05)	(0.05)	(0.05)	(0.02)					
NGC 1068...	264	10.34	10.29	9.80	9.03	8.22	-12.67	0.05	2.07	0.77	1.58	1.255
		-20.58	-20.63	-21.13	-21.89	-22.70	14.10	(0.05)	(0.05)	(0.08)	(0.06)	(0.058)
		(0.05)	(0.05)	(0.05)	(0.06)	(0.05)	(0.02)					
NGC 1275...	89.7	11.57	12.25	11.93	11.26	10.70	...	-0.68	1.55	0.68	1.23	...
		-22.70	-22.02	-22.34	-23.02	-23.57	...	(0.07)	(0.07)	(0.09)	(0.10)	...
		(0.07)	(0.05)	(0.08)	(0.05)	(0.06)	...					
NGC 1316...	281	13.97	11.94	9.81[c]	8.87[c]	8.31[c]	NC[e]	2.04	3.63[c]	0.94[c]	1.50[c]	NC
		-17.18	-19.22	-21.34[c]	-22.28[c]	-22.84[c]	NC	(0.20)	(0.08)	(0.05)	(0.05)	...
		(0.19)	(0.07)	(0.05)	(0.05)	(0.05)	...					
NGC 1317...	107	13.26	13.60	11.99	11.07	10.44	-12.15	-0.34	3.16	0.92	1.55	0.025
		-17.90	-17.55	-19.17	-20.08	-20.71	14.67	(0.05)	(0.05)	(0.05)	(0.05)	(0.001)
		(0.05)	(0.05)	(0.05)	(0.05)	(0.05)	(0.02)					

NGC 1399...	190	12.82	12.95	10.79	9.77[f]	9.35[f]	...	-0.13	3.60	1.02	1.44	...
		-18.32	-18.19	-20.35	-21.37[f]	-21.79[f]	...	(0.05)	(0.05)	(0.05)	(0.05)	...
		(0.05)	(0.05)	(0.05)	(0.05)	(0.05)	...					
NGC 1404...	99.6	14.00	13.43	...	10.19[d]	...	...	0.56	...	...	...	...
		-17.14	-17.71	...	-20.95[d]	...	...	(0.08)	...	...	...	...
		(0.07)	(0.05)	...	(0.05)	...	...					
NGC 2146...	291	...	12.59	11.13	10.38[d]	9.89	-11.11	...	2.70	0.75[d]	1.24	...
		...	-18.11	-19.57	-20.32[d]	-20.81	15.62	...	(0.18)	(0.05)	(0.05)	...
		...	(0.18)	(0.05)	(0.05)	(0.05)	(0.04)					
NGC 2992...	74.4	...	14.44	12.97	12.09	11.53	-11.93	...	2.91	0.87	1.44	...
		...	-17.86	-19.34	-20.21	-20.78	15.12	...	(0.15)	(0.05)	(0.05)	...
		...	(0.15)	(0.05)	(0.05)	(0.05)	(0.02)					
NGC 2993...	75.9	11.36	12.09	12.87	12.53	12.14	-11.60	-0.73	-0.05	0.34	0.72	0.041
		-20.95	-20.21	-19.44	-19.77	-20.16	15.45	(0.06)	(0.05)	(0.05)	(0.05)	(0.002)
		(0.05)	(0.05)	(0.05)	(0.05)	(0.05)	(0.02)					
NGC 3031...	750	9.20	8.95	7.91[c]	7.01[c,f]	6.55	-12.46[c,f]	0.25	2.40	0.90[c]	1.36[c]	2.188[c]
		-18.58	-18.83	-19.88[c]	-20.77[c,f]	-21.23	13.68[c,f]	(0.33)	(0.05)	(0.08)	(0.05)	(0.665)
		(0.33)	(0.05)	(0.05)	(0.07)	(0.05)	(0.02)					
NGC 3034...	529	...	10.64	8.88[c]	8.14	7.54[c]	-9.82[c]	...	3.10[c]	0.74[c]	1.33[c]	...
		...	-17.14	-18.91[c]	-19.64	-20.24[c]	16.32[c]	...	(0.09)	(0.05)	(0.05)	...
		...	(0.08)	(0.05)	(0.05)	(0.05)	(0.02)					
UGC 5336...	99.3	13.24	13.79	14.66[c]	14.51[d]	14.02	...	-0.55	-0.23	0.15[d]	0.64[c]	...
		-14.54	-14.00	-13.12[c]	-13.27[d]	-13.76	...	(0.51)	(0.15)	(0.08)	(0.09)	...
		(0.49)	(0.14)	(0.08)	(0.05)	(0.06)	...					
UGC 6697...	63.9	12.86	13.33	14.32	13.68[d]	13.62	...	-0.47	-0.30	0.64[d]	0.69	...
		-21.81	-21.35	-20.36	-20.99[d]	-21.05	...	(0.07)	(0.05)	(0.05)	(0.05)	...
		(0.06)	(0.05)	(0.05)	(0.05)	(0.05)	...					
NGC 4151...	241	10.26	11.11	11.12	10.55	10.03	NC	-0.85	1.08	0.57	1.09	NC
		-20.41	-19.55	-19.55	-20.12	-20.64	NC	(0.05)	(0.05)	(0.07)	(0.05)	...
		(0.05)	(0.05)	(0.05)	(0.05)	(0.05)	...					
NGC 4321...	274	9.47	10.28	10.26	9.63	9.10	-11.16	-0.81	1.18	0.64	1.17	0.085
		-21.55	-20.74	-20.76	-21.39	-21.92	15.63	(0.31)	(0.24)	(0.05)	(0.05)	(0.017)
		(0.20)	(0.24)	(0.05)	(0.05)	(0.05)	(0.03)					
Secondary Objects												
Mrk 335...	24.6	11.38	12.35	...	...	...	...	-0.97	...	...	...	...
		-23.73	-22.76	...	...	...	...	(0.05)	...	...	...	...

		(0.05)	(0.05)	...	...	...	...					
NGC 891...	302	...	13.00	...	...	NC	-11.32	...	NC	...	NC	...
		...	-16.73	...	...	NC	15.21	...	...	...	...	...
		...	(0.23)	...	...	...	(0.02)					
NGC 1267...	28.7	...	15.80	13.59[d]	12.61[d]	...	...	...	...	0.98[d]	...	...
		...	-18.47	-20.68[d]	-21.66[d]	...	...	...	...	(0.05)	...	...
		...	(0.15)	(0.05)	(0.05)	...	...					
NGC 1268...	28.7	...	15.20	...	...	...	...	...	...	...	...	...
		...	-17.96	...	...	...	...	...	...	...	...	...
		...	(0.14)	...	...	...	...					
NGC 1270...	52.4	...	17.02	13.62	12.63[c]	12.02[c]	...	...	5.00[c]	0.99[c]	1.60[c]	...
		...	-17.25	-20.65	-21.64[c]	-22.25[c]	...	...	(0.27)	(0.09)	(0.10)	...
		...	(0.26)	(0.08)	(0.05)	(0.06)	...					
NGC 1272...	85.3	...	16.84	12.70	11.60	11.05	...	...	5.80	1.10	1.65	...
		...	-17.43	-21.58	-22.67	-23.22	...	...	(0.28)	(0.09)	(0.10)	...
		...	(0.27)	(0.08)	(0.05)	(0.06)	...					
NGC 1273...	48.9	...	17.24	13.71	12.77	12.15	...	...	5.09	0.94	1.56	...
		...	-17.03	-20.56	-21.51	-22.12	...	...	(0.26)	(0.09)	(0.10)	...
		...	(0.25)	(0.08)	(0.05)	(0.06)	...					
UGC 2665...	42.6	...	15.56	14.68	13.99	...	...	...	...	0.69	...	...
		...	-19.52	-20.41	-21.10	...	...	...	...	(0.09)	...	...
		...	(0.10)	(0.08)	(0.05)	...	...					
NGC 1277...	20.6	...	17.34	14.14	13.15	12.60	...	...	4.75	0.99	1.55	...
		...	-16.93	-20.13	-21.12	-21.68	...	...	(0.42)	(0.09)	(0.10)	...
		...	(0.42)	(0.08)	(0.05)	(0.06)	...					
NGC 1278...	54.5	...	16.59	13.23	12.17	11.61	...	...	4.97	1.07	1.62	...
		...	-17.69	-21.04	-22.11	-22.66	...	...	(0.23)	(0.09)	(0.10)	...
		...	(0.23)	(0.08)	(0.05)	(0.06)	...					
NGC 1282...	58.4	...	17.14	13.36	12.44	11.88	...	...	5.26	0.92	1.48	...
		...	-15.29	-19.07	-19.99	-20.55	...	...	(0.24)	(0.09)	(0.10)	...
		...	(0.23)	(0.08)	(0.05)	(0.06)	...					
NGC 1396...	23.9	...	17.90	...	14.65[d]	...	...	...	...	...	...	...
		...	-13.24	...	-16.49[d]	...	...	...	...	...	...	...
		...	(0.12)	...	(0.05)	...	...					
NGC 2551...	49.9	15.64	14.16	13.09[d]	12.08[d]	...	...	1.48	...	1.01[d]	...	...
		-16.88	-18.36	-19.42[d]	-20.43[d]	...	...	(0.44)	...	(0.05)	...	...
		(0.44)	(0.06)	(0.05)	(0.05)	...	...					
NGC 3837...	43.5	...	17.57	14.38	13.39[d]	12.98	...	...	4.59	0.99[d]	1.40	...

		...	-17.10	-20.29	-21.28[d]	-21.69	...	...	(0.76)	(0.05)	(0.05)	...
		...	(0.76)	(0.05)	(0.05)	(0.05)	...					
MCG 3-30-71...	26.1	14.79	15.29	15.69	15.40[d]	15.12	...	-0.50	0.16	0.29[d]	0.56	...
		-19.28	-18.78	-18.38	-18.66[d]	-18.94	...	(0.25)	(0.16)	(0.05)	(0.05)	...
		(0.20)	(0.16)	(0.05)	(0.05)	(0.05)	...					
NGC 3842...	58.6	...	15.93	13.41	12.45[d]	12.16	...	...	3.77	0.96[d]	1.25	...
		...	-18.75	-21.26	-22.22[d]	-22.51	...	...	(0.38)	(0.05)	(0.05)	...
		...	(0.38)	(0.05)	(0.05)	(0.05)	...					
CGCG 97-114...	8.1	15.89	16.30	...	...	...	...	-0.41	...	...	...	...
		-18.78	-18.37	...	...	...	...	(0.25)	...	...	...	...
		(0.20)	(0.16)	...	...	...	...					
NGC 4156...	50.4	14.08	15.11	14.05	13.19	12.70	NC	-1.02	2.41	0.86	1.35	NC
		-20.70	-19.68	-20.74	-21.60	-22.09	NC	(0.13)	(0.10)	(0.07)	(0.05)	...
		(0.09)	(0.09)	(0.05)	(0.05)	(0.05)	...					
UGC 7188...	42.0	14.12	≤ 15.86[g]	15.57	15.09	14.74	NC	...[g]	...[g]	0.48	0.83	NC
		-16.54	≤ -14.81[g]	-15.10	-15.58	-15.93	NC	...	...	(0.10)	(0.08)	...
		(0.09)	(0.26)	(0.07)	(0.07)	(0.05)	...					
NGC 4470...	44.5	...	13.29	13.17[d]	12.63[d]	12.17[d]	...	...	1.12[d]	0.54[d]	1.00[d]	...
		...	-17.73	-17.85[d]	-18.39[d]	-18.85[d]	...	...	(0.16)	(0.05)	(0.05)	...
		...	(0.16)	(0.05)	(0.05)	(0.05)	...					
NGC 4472...	308	...	13.68	9.43[d]	8.46[d]	...	...	...	...	0.97[d]	...	...
		...	-17.34	-21.59[d]	-22.56[d]	...	...	...	...	(0.05)	...	...
		...	(0.14)	(0.05)	(0.05)	...	...					
NGC 4476...	53.5	...	14.72	13.18[d]	12.33[d]	11.91[d]	...	...	2.81[d]	0.85[d]	1.27[d]	...
		...	-16.30	-17.84[d]	-18.69[d]	-19.11[d]	...	...	(0.21)	(0.05)	(0.05)	...
		...	(0.21)	(0.05)	(0.05)	(0.05)	...					
NGC 4478...	61.4	16.69	15.06	12.28[d]	11.42[d]	10.78[d]	...	1.63	4.28[d]	0.86[d]	1.50[d]	...
		-14.33	-15.96	-18.74[d]	-19.60[d]	-20.24[d]	...	(0.79)	(0.17)	(0.05)	(0.05)	...
		(0.78)	(0.17)	(0.05)	(0.05)	(0.05)	...					
NGC 4486...	301	13.12	12.66	9.87	8.94	8.26	...	0.46	4.41	0.94	1.62	...
		-17.90	-18.36	-21.15	-22.08	-22.76	...	(0.17)	(0.09)	(0.09)	(0.08)	...
		(0.15)	(0.08)	(0.07)	(0.05)	(0.05)	...					

Notes. - Col. (1) Galaxy Identification. Col. (2) Radius (in arcsec) within which the total integrated magnitudes are measured. Cols. (3)-(7) First line shows the total apparent magnitudes within the listed bandpasses as defined in Section 4.5 . Second line shows the total absolute magnitudes, using the adopted distances given in Table 3 . Photometric errors, which do not include uncertainties in calibration or in extinction corrections, are given in parentheses. All magnitudes presented here have been corrected for foreground galactic extinction using the extinction estimates listed in Table 5 and the Cardelli et al. 1989 reddening law. The *R*-band filter is calibrated on the Cousins *R* system. Col. (8) First line shows Hα total integrated flux, in units of log$_{10}$(ergs s^{-1} cm^{-2}), also corrected for extinction. Second line shows Hα luminosity, in unit of $\log_{10}$(ergs s-1). No correction for N [II] emission has been made. Cols. (9)-(12) First line shows the global colors within the listed bandpasses, corrected for foreground extinction. Second line shows uncertainty in the color index. Col. (13) Ratio of FUV flux (ergs s^{-1} cm^{-2} $Å^{-1}$) to Hα flux (ergs s^{-1} cm^{-2}), corrected for extinction.

[a] Ratio of FUV flux (erg s^{-1} cm^{-2} $Å^{-1}$) to Hα flux (erg s^{-1} cm^{-2}).

[b] UV emission completely filled the image frame, and so no total integrated magnitudes or colors could be computed.

[c] Total integrated magnitude was based on the surface brightness profile and the assumption of azimuthal symmetry, in order to compensate for lost light due to the galaxy extending beyond the edges of the image frame. Any associated colors should be regarded with caution.

[d] Averaged photometry taken from Prugniel & Heraudeau (1998). Note that there may be uncertainties in comparing this literature value to the atlas photometry for this galaxy, since the same stars have not consistantly been masked out in both data sets.

[e] "NC" refers to data which were omitted due to lack of proper calibration.

[f] Central core of galaxy was saturated. However, total integrated colors should not be affected.

[g] The MUV image had a defect running through the galaxy. The process of removing the defect also removed some of the galaxy flux. The associated M_{25} photometry should be considered as an upper limit only.

No integrated magnitudes are quoted for NGC 224 because the two Astro-1 UIT frames contain only a small fraction of the entire object. A small region of NGC 598 (M33) also extends beyond the data frame; however, we attempted to account for the missing flux by assuming azimuthal symmetry in the radial light profiles.

Foreground stars can be non-negligible contributors to large-aperture flux measures, especially in the optical bands. Prompted by a desire to compare UV and optical photometry of galaxies free of field star contamination, we chose to mask out field stars which affect the photometry. The R-band images were used to determine coordinates of superposed field stars, and the Hα images were used to distinguish field stars from H II knots within the galaxy (which were not masked). Masks of optically bright stars which were not UV sources were not applied to the UIT images. For all filters except Hα, the integrated photometry presented here has been adjusted for galaxy light which had been masked out, using the surface brightness profile to interpolate the flux within masked pixels. In the optical images, typically there were many masked stars. However, due to the complex, "blobby" morphology of Hα emission, we felt that correcting for masked pixels using this approach would have produced too large a correction. Therefore, no corrections for masked pixels has been made in the Hα data. We emphasize that the photometry presented here cannot be directly compared to values in the literature without consideration for the effects of superposed field stars.

4.6. Length Scales and Light Concentration

Quantitative measures of the light distribution in galaxies are valuable as input into models of galaxy evolution and for intercomparison of local and high-redshift systems (e.g., Abraham 1997). We have derived a set of photometric parameters for the primary atlas sample which quantifies the size and intensity of the global light distribution. In Table 7 we list half-light radii for the available bandpasses. These values were computed assuming that the integrated magnitudes given in Table 6 represent the total luminosities of the galaxy. Growth curves (see Appendix B) were interpolated to yield the radius at which the integrated flux equals half of the total flux for that bandpass.

Table 7. Half-Light Radii

Object (1)	$r_{1/2}(15)$ (arcsec) (kpc) (2)	$r_{1/2}(25)$ (arcsec) (kpc) (3)	$r_{1/2}(B)$ (arcsec) (kpc) (4)	$r_{1/2}(V)$ (arcsec) (kpc) (5)	$r_{1/2}(R)$ (arcsec) (kpc) (6)	$r_{1/2}$(Hα) (arcsec) (kpc) (7)
NGC 221...	20	25	...	...	...	...
	0.1	0.1	...	...	...	...
NGC 224...	...[a]	...[a]	...	...	...	...
	...[a]	...[a]	...	...	...	...
NGC 598...	830[b]	771[b]	...	...	642[b]	819[b]

	3.4[b]	3.1[b]	...	...	2.6[b]	3.3[b]
NGC 628...	149	139	119	108	106	152
	5.5	5.1	4.4	4.0	3.9	5.6
NGC 1068...	19	27	35	37	32	6
	1.4	2.0	2.6	2.8	2.4	0.4
NGC 1275...	17	17	22	24	25	...
	5.9	5.7	7.6	8.5	8.8	...
NGC 1316...	29	62	53[b]	52[b]	52[b]	26
	2.4	5.1	4.4[b]	4.3[b]	4.3[b]	2.1
NGC 1317...	13	14	24	25	26	12
	1.1	1.2	2.0	2.0	2.1	1.0
NGC 1399...	13	22	36	53[c]	43[c]	...
	1.1	1.8	2.9	4.3[c]	3.6[c]	...
NGC 1404...	14	21	...	...	...	...
	1.1	1.7	...	...	...	...
NGC 2146...	...	70	75	...	63	26
	...	4.7	5.0	...	4.2	1.8
NGC 2992...	...	25	28	26	24	10
	...	3.5	3.9	3.6	3.4	1.4
NGC 2993...	10	9	11	12	12	5
	1.4	1.3	1.5	1.7	1.6	0.7
NGC 3031...	410	375	209[b]	192[b,c]	159	380[b,c]
	7.2	6.5	3.7[b]	3.3[b,c]	2.8	6.6[b,c]
NGC 3034...	...	113	107[b]	93	92[b]	72[b]
	...	2.0	1.9[b]	1.6	1.6[b]	1.3[b]
UGC 5336...	43	43	41[b]	...	43	...
	0.8	0.8	0.7[b]	...	0.8	...
UGC 6697...	31	31	23	...	21	...
	13	13	9.5	...	8.8	...
NGC 4151...	11	7	22	48	36	13[c]
	0.7	0.5	1.5	3.1	2.4	0.9[c]
NGC 4321...	96	82	97	94	95	90
	7.4	6.4	7.5	7.3	7.4	69.

Notes. - Col. (1) Galaxy identification. Cols. (2)-(7) First line shows the radius (in units of arcsec) enclosing half the light within the listed bandpass. Second line is the same as above, but in units of kpc, using adopted distances given in Table 3.

[a] No half-light radius could accurately be computed for NGC 224, due to much of the galaxy extending beyond the image frame.

[b] The half-light radius was computed using the surface brightness profile and assuming azimuthal symmetry for the galaxy, since the galaxy emission extended beyond the edges of the CCD frame.

[c] Half-light radius was based on photometry which ignored a few saturated pixels in the galaxy core.

In Table 8 we present two measures of the light concentration in the primary galaxies. Central surface brightness (cols. [2]-[7]) is defined here as the mean surface brightness within the central one kiloparsec-diameter region of the galaxy. For a few distant systems the adopted physical size corresponded to an angular size which was less than the size of the smallest synthetic aperture; these values are noted in the table. All values in Table 8 have been corrected for foreground extinction, as described previously.

Table 8. Mean Surface Brightness

	CENTRAL SURFACE BRIGHTNESS						SURFACE BRIGHTNESS AT $r_{1/2}$					
OBJECT (1)	$(\mu_{15})_0$ (2)	$(\mu_{25})_0$ (3)	$(\mu_B)_0$ (4)	$(\mu_V)_0$ (5)	$(\mu_R)_0$ (6)	$(\mu_{H\alpha})_0$ (7)	$(\mu_{15})_0$ (8)	$(\mu_{25})_0$ (9)	$(\mu_B)_0$ (10)	$(\mu_V)_0$ (11)	$(\mu_R)_0$ (12)	$(\mu_{H\alpha})_0$ (13)
NGC 221	21.81	21.92	...	...	...	...	21.07	19.99	...	...	...	...
NGC 224	20.83	20.33	...	...	...	...	...[a]	...[a]	...	...	...	...
NGC 598	19.90	20.75	...	...	20.14	-15.20	20.89[b]	21.80[b]	...	...	21.29[b]	-15.61[b]
NGC 628	21.18	21.40	20.31	19.55	19.08	-15.63	22.15	22.51	22.16	21.43	21.00	-15.92
NGC 1068	17.43	18.16	17.37	16.70	15.46	-15.00	18.49	19.22	19.33	18.72	17.57	-14.95
NGC 1275	17.86[c]	18.36[c]	18.01[c]	17.57[c]	17.09[c]	...	19.37	20.02	20.35	19.90	19.42	...
NGC 1316	21.50	20.31	17.50	16.48	15.88	NC[d]	22.85	22.52	20.05[b]	19.07[b]	18.50[b]	NC
NGC 1317	21.02	21.23	18.90	17.92	17.22	-14.72	20.70	21.20	20.66	19.76	19.31	-14.97
NGC 1399	19.48	20.32	18.43	19.21[ce]	18.65[ce]	...	20.36	21.67	20.55	20.37	19.55	...
NGC 1404	20.71	20.73	...	...	...	...	21.59	22.01	...	...	...	...
NGC 2146	...	22.04	20.13	...	18.14	-13.92	...	23.17	21.87	...	20.26	-14.49
NGC 2992	...	21.30	19.23	18.00	17.17	-13.58	...	22.11	20.90	19.87	19.15	-14.18
NGC 2993	16.92	17.63	18.26	18.03	17.69	-13.53	17.85	18.55	19.57	19.51	19.05	-13.64
NGC 3031	21.68	20.74	18.37	17.50[e]	16.79	-17.50[e]	23.51	23.11	20.79[b]	19.69[b]	18.85	-18.14[b]
NGC 3034	...	21.25	19.33	18.37	17.64	-13.63	...	21.85	19.97[b]	18.93	18.31[b]	-13.91[b]
UGC 5336	22.97	23.69	24.47	...	23.93	...	23.38	23.96	24.69[b]	...	24.20	...
UGC 6697	20.12[c]	20.76[c]	20.83[c]	...	19.93[c]	...	20.36	20.83	21.17	...	20.30	...
NGC 4151	16.36	16.97	17.32	17.76	16.81	NC	16.91	16.81	19.37	20.52	19.41	NC
NGC 4321	18.51	18.85	19.06	18.35	17.78	-14.53	21.15	21.67	22.01	21.27	20.77	-15.79

Notes. - Col. (1) Galaxy identification. Cols. (2)-(5) Central surface brightness (mag arcsec $^{-2}$) of the listed bandpass, as defined in Section 4.5. These values have been corrected for foreground galactic extinction using the extinction extimates listed in Table 5 and the Cardelli et al. 1989 reddening law. The R-band is calibrated on the Cousins-R system. Col. (6) Hα central surface brightness, in units of log$_{10}$(ergs s^{-1} cm^{-2} arcsec^{-2}), corrected for extinction. No correction for [N II] contamination has been made. Cols. (7)-(12) Average surface brightness within the half-light radius, for the listed bandpass (see Section 4.5). Extinction corrections have been applied. Col. (13) Average Hα surface brightness, in units of log$_{10}$(ergs s^{-1} cm^{-2} arcsec^{-2}), within the half-light radius. Extinction corrections have been applied.

[a] Because much of this galaxy extends well outside of the image frame, no accurate half-light radius could be computed.

[b] Refers to cases in which galaxy emission extends beyond the edges of the CCD frame, such that an accurate half-light radius cannot be determined. In such cases, a lower limit to the half-light radius (and the corresponding surface brightness at that radius) is based on the total integrated light seen in the image frame.

[c] Refers to cases in which a 0.5 kpc radius is smaller than the smallest aperture. In such situations, the smallest aperture was used to compute the central surface brightness.

[d] "NC" refers to data which were omitted due to lack of proper calibration.

[e] Half-light radius based on photometry which ignored a few saturated pixels in the galaxy core.

Effective surface brightness, listed in columns (8)-(13), is defined here as the surface brightness of a source within the half-light radius listed in Table 7. These values were determined by the total flux within the half-light radius divided by the corresponding area. Uncalibrated data presented in Table 8 are indicated by footnotes.

5. COMMENTS ON INDIVIDUAL OBJECTS

5.1. Primary Objects

NGC 221 (M32). - A satellite to M31, M32 is a compact dwarf elliptical galaxy noted for its high optical surface brightness. The UV images show a compact, centrally concentrated source projected onto the disk of M31. Enlarged UV images of M32 are shown in Figure 4*a*, while the full-field versions from which these were extracted are shown in the NGC 224 / M31 mosaics in Figures 5*a* - 5*b*. M32 is the bright object near the left hand (eastern) edge of the M31 UIT 25 mosaic, just below the overlap region.

OB stars in the M31 disk adjacent to M32 produce a complex background which has been modeled and removed from our photometry, but which produces greater uncertainty in the integrated UV magnitudes. M32 exhibits a good fit to a de Vaucouleurs $r^{0.25}$ profile for $r \lesssim 40''$ in both the FUV and MUV bands. Axial ratios of the UV isophotes match those of the optical bands; this is true in general for the normal ellipticals in our sample. M32 has the reddest central (FUV-MUV) color (after extinction corrections) of any of the five normal early-type systems (M32, NGC 1399, NGC 1404, and the bulges of M31 and M81) included in our sample. This is consistent with results from *IUE* (Burstein et al. 1988; O'Connell et al. 1992). The *R*-band photometry plotted in Figure 4*b* was interpolated from the major axis profile data taken from Kent (1987). The sharp central rise in the *R*-band flux with respect to the UV flux is partially an artifact of mismatched spatial resolution.

There are strong radial gradients in both the (FUV-MUV) and (FUV-*B*) colors. The colors become bluer with increasing radius, contrary to the UV color gradients observed in other dynamically hot systems (O'Connell et al. 1992; Ohl et al. 1998). As in the case of M31 (below), individual massive stars hotter than B1 V would be detectable in our UV images if they were present. No isolated point sources are visible within M31 in the UV imagery. Instead, the UV light distribution shows an azimuthally smooth, radial decline. This UV morphology is typical of other normal E galaxies and spiral bulges and is evidence that the far-UV light originates in low-mass stars (reviewed in O'Connell 1999). *HST* UV imagery of the central region of M32 has been presented by Bertola et al. (1995); Cole et al. (1998); and Brown et al. (1998) with the FOC and WFPC2 cameras, and more recently by Brown et al. (2000) with STIS. These images confirm the absence ofluminous, massive OB stars. The STIS images of Brown et al. (2000) are sufficiently deep to resolve the horizontal branch (HB) and to confirm that the UV light in M32 is produced by a mixture of evolved hot HB stars and more luminous, but shorter-lived, post-HB stars. The absence of a UV-bright nucleus is notable since M32 is the densest resolvable extragalactic system (Lauer et al. 1998). Evidently, high stellar density alone is not sufficient to produce an active nucleus or a nuclear population of UV-bright stars.

NGC 224 (M31). - The Andromeda galaxy, a member of the Local Group, is a disk system, type SA(s)b, ~ 690 kpc in distance, and inclined 78° to our line of sight. Several low-resolution, wide field UV images of M31 were obtained with both balloon (Deharveng et al. 1980) and rocket experiments (Deharveng et al. 1976; Carruthers, Heckathorn, & Opal 1978; Bohlin et al. 1985; Bohlin et al. 1988), the latter two in both FUV and MUV bands. The best of these images achieved a spatial resolution of ~ 15" and showed that the UV emission from M31 is dominated by the bulge and a broken ring of OB associations.

UIT imagery was obtained in two overlapping fields during Astro-1; M31 completely fills the field of view in both. One field is centered on the bulge; the other is centered ~ 40' to the southwest along the major axis. Images in each filter have been combined and are displayed as mosaics in Figures 5*a* - 5*b*. The radial UV surface brightness and color profiles plotted in Figures 5*a* - 5*b*, respectively, are based on mean values within those segments of the elliptical apertures which lie within our mosaic. The profiles therefore reflect behavior only near the southwestern major axis for $r < 50'$. The *R*-band profile shown in Figures 5*a* - 5*b* was interpolated from the major axis profile data taken from Kent (1987).

The bulge is extended in both FUV and MUV and displays a relatively smooth appearance; neither bright substructure nor dust lanes are evident. As in the case of M81, the bulge of M31 is considerably more prominent at longer wavelengths, though the contrast is not as extreme as in M81. In both FUV and MUV light, the inner bulge follows a reasonably good de Vaucouleurs $r^{0.25}$ profile to $r \sim 90''$. Except at very small radii where the spatial resolution of the data are mismatched, the bulge shows only a small color gradient in (25-*R*). However, the FUV light is more centrally concentrated, producing a strong radial color gradient in (FUV-MUV) for $0 \lesssim r \lesssim 150''$, in which the light gets redder with increasing radius. This behavior is typical of large spiral bulges and elliptical galaxies but is much larger in amplitude and is reversed in sense from gradients in the optical bands such as (*B*-*V*) or (*V*-*K*) (O'Connell et al. 1992; Ohl et al. 1998).

There are no detected UV point sources in the bulge, even though individual stars as faint as B1 V (*m*(MUV) ~ 18.4) would be above the MUV threshold (O'Connell et al. 1992). If the FUV light from the bulge originated in recently formed massive stars with a normal initial mass function, there would be ~ 200 OB stars visible within $r \lesssim 2'$. Their absence supports the interpretation of the FUV light as originating from low-mass, post-giant branch stars (e.g., Greggio & Renzini 1990; O'Connell 1999). *HST* UV observations of the core of M31 have been presented by King et al. (1992); Bertola et al. (1995); King, Stanford, & Crane (1995); and Brown et al. (1998). At *HST* resolution, the nucleus of M31 is double, and the component coincident with the dynamical center has UV colors which are bluer than those of the background bulge and therefore may contain massive stars formed through stellar collisions (King et al. 1995; Lauer et al. 1998). The second, off-nuclear component has UV colors similar to the bulge. These sources are not resolved in the UIT photometry. Brown et al. (1998) have partially resolved the hot stellar population responsible for the FUV light in the central 14" × 14" using *HST* /FOC images. Color-magnitude diagrams of the resolved stars are consistent with objects that have evolved from the extreme horizontal branch.

Outside the bulge, the MUV light profile roughly parallels the *R*-band profile. However, the FUV profile flattens and even rises slightly with increasing radius, meaning that the (FUV-MUV) color becomes systematically bluer with radius. This result is preliminary because of the difficulty in determining the sky background (see Section 4). The existence of a smooth radial distribution of FUV emission at small radii suggests the presence of an FUV-bright inner disk which spatially overlaps with the outer bulge. Such an inner disk is not seen in the case of M81 (NGC 3031, see Fig. 17*a*), where the combined FUV light of the bulge and disk is undetectable at inner radii (r < 3'.5 = ~ 3.5 kpc). The surface brightness profiles are quite different between these two objects, despite the fact that M81 is only slightly earlier in Hubble type (Sab rather than Sb).

The outer disk of M31 is rich in UV-bright massive stars, the brightest concentration of which is NGC 206, located ~ 5' from the southwestern edge of the mosaics shown in Figures 5*a* - 5*b*. Hill et al. (1992a) provide UV photometry of 30 resolved stars in NGC 206; most are evolved OB stars with $30 \lesssim M / M_{\odot} \lesssim 60$. Hill et al. (1993c, 1995b) presented enlargements of the UIT images for some 60 OB associations in M31 and photometered individual stars and integrated light. They infer a maximum stellar mass of 85 $M_{\odot}$. Only about 40% of the integrated MUV light and 20% of the FUV light of a typical association comes directly from the resolved stars; the remainder may be dust-scattered starlight with a smaller contribution from fainter stars with $T \gtrsim$ 10,000 K. Bohlin et al. (1993) obtained UV photometry for 43 compact clusters; most of these are old globulars, but seven appear to be compact young clusters. The disk shows a strong (FUV-MUV) color gradient, becoming systematically bluer from r ~ 3' to r ~ 50' (~ 10 kpc) by about 2 mag. This reflects the increasing contribution of OB associations to the total integrated light at larger radii.

NGC 598 (M33). - This object, of type SA(s)cd at a distance of D ~ 700 kpc, 52' × 56' in size, and inclined ~ 55°, is the least luminous of the three spiral galaxies in the Local Group. The UIT images were centered on OB association NGC 595 to permit the Hopkins Ultraviolet Telescope to obtain spectra during the UIT exposures. M33 extends slightly beyond the UIT field, but almost all of the UV-luminous regions are contained within the 40' field. The UIT, Hα, and *R*-band images are presented in Figure 6*a*.

The UIT images are almost completely filled with UV-bright knots and clusters, which roughly trace out spiral arms. High surface brightness UV features are found at all radii, but there is considerable diffuse UV light as well. The galaxy is considerably more irregular and much less centrally concentrated in the UV than in the optical bands. Qualitatively, the spiral structure is traced better by the UV continuum than by the (younger) Hα-emitting regions. Several giant extragalactic H II regions (GEHRs), including NGC 604, are visible in these frames. NGC 604 is located ~ 12' NE of the nucleus and is prominent in both the UV and Hα images. Massey et al. (1996) have cataloged the 356 brightest UV objects on the UIT frames and obtained follow-up spectroscopy for about half of these. Most are classified as O and early-B supergiants.

The UV morphology of M33 has been discussed by Landsman et al. (1992) using UIT data and by Buat et al. (1994) using lower resolution data obtained with the FOCA balloon-borne telescope. The FOCA image contains the entire galaxy at 20" resolution in a bandpass centered at 2000 Å. Buat et al. (1994) find that about 80% of the FUV light is contributed by discrete sources rather than a diffuse background. This is a larger discrete contribution than found in more luminous spirals like M74 (Cornett et al. 1994). Keel (1998) has used *Voyager 2* data to obtain one-dimensional spatial profiles for M33 in Lyα and the 800-1200 Å continuum and compared this to the UIT photometry.

The UV brightness profiles shown in Figure 6*b* display a steep decline to a radius of 3', followed by a long plateau, then a gradual decline. This pattern has been noted in other disk galaxies imaged by UIT (Fanelli et al. 1997b) and is distinct from the more smoothly declining optical broadband radial profiles. For $r \gtrsim$ 3', the *R*-band profile is well fitted by an exponential, whereas the UV bands exhibit considerably more structure. Inflections in the UV profiles are caused by luminous OB associations, in particular the "bump" at r ~ 14' due to NGC 604. Landsman et al. (1992) find scale lengths for the best-fit exponentials of 5'.6 in the MUV and 7'.0 in the FUV. These values imply a gradient toward bluer (UV-visible) and (FUV-MUV) colors with increasing radius, as seen in the color profiles in Figure 6*b*, and in other disk galaxies imaged by UIT (M74 and M81). Over the entire disk δ(FUV-MUV) ~ -0.6 mag, about 1/3 of the gradient found in M31. Over the same radius, δ(NUV-*R*) ~ -1.0 mag. Both internal reddening and changes in the history of star formation can produce the observed color changes (Landsman et al. 1992; Cornett et al. 1994), although the larger amplitudes seen in objects like M74 and M81 argue for the latter.

NGC 628 (M74). - NGC 628, a face-on spiral of type SA(s)c at a distance of ~ 7.6 Mpc, shows considerable grand design spiral structure and has been used for density wave studies (Cepa & Beckman 1990). In the UV (see Fig. 7*a*), the spiral arms are highlighted as "beads on a string," where bright knots embedded in diffuse emission trace the spiral pattern (Chen et al. 1992;

Cornett et al. 1994). The pattern is much more organized than in the case of the slightly later type system M33. Many of the UV-bright knots are also bright in $\mathrm{H}\alpha$, though, as in the other spiral disks with UV data, there are large variations in the ratio of $\mathrm{H}\alpha$ to far-UV continuum among the knots. As seen best in the MUV image, the brightest knots tend to lie on the inside edges of the spiral arms formed by the diffuse UV continuum. This is in the correct sense for an age gradient if gas in the disk rotates through the spiral pattern from inside to outside, such that the youngest and most massive stars are located at the inner edge of the pattern. Over 70% of the UV light in both bands originates from the more diffuse and presumably older component, rather than from the younger, compact regions.

As in M33, the UV surface brightness profiles (Fig. 7*b*) show smaller radial gradients than those observed in the optical bandpasses. The stronger central concentration of the optical light is evident in the images presented in Figure 7*a* and is consistent with Cornett et al. (1994), who find that azimuthally averaged scale lengths for the continuum emission *decrease* with *increasing* wavelength. However, the UV profiles are clearly nonexponential despite the approximately exponential behavior of the *R*-band profile. UV/optical colors become systematically bluer by over 1.5 mag with increasing radius in the disk. The $\mathrm{H}\alpha$/UV flux ratio also systematically increases with radius. Using color-color diagrams, Cornett et al. (1994) have analyzed these color gradients and conclude that they reflect the star formation history rather than metallicity or internal extinction. The entire disk has undergone active star formation within the past ~ 500 Myr, but the inner regions have experienced more rapidly declining star formation than the outer regions. What is surprising is not that the star formation history changes with radius but that it exhibits such a remarkably smooth and organized pattern of change. Other spirals, e.g., M33 and M81, likewise have organized patterns but with different color-color relations. Such patterns are important clues to the global mechanisms by which disk galaxies regulate star formation.

NGC 1068 (M77). - An SA(r)b disk system, NGC 1068 is the prototype Type 2 Seyfert galaxy and one of the nearest galaxies harboring an AGN (*D* ~ 15.1 Mpc). In addition to the active nucleus, the optical disk exhibits a number of unusual features, most prominently a high surface brightness inner disk and a population of luminous knots.

Neff et al. (1994) provide a detailed description of the UV morphology of NGC 1068; the UV photometry is discussed by Fanelli et al. (1997a). The UV images, presented in Figure 8*a*, show the bright AGN, a population of very luminous starburst knots, a bright oval inner disk, and a fainter, more circular halo. The UV knots were first studied with *IUE* spectra and were found to be sites of intense recent massive star formation (Snijders, Briggs, & Boksenberg 1982; Weedman & Huenemoerder 1985; Bruhweiler, Truong, & Altner 1991; Hutchings et al. 1991). The brightest knot complex, located ~ 750 pc from the nucleus in PA ~ 315°, has ~ 80 times the luminosity of 30 Dor and gives NGC 1068 a "double nucleus" appearance at UV wavelengths, in marked contrast to its optical morphology. The radial decline of the azimuthally averaged UV surface brightness (Fig. 8*b*) can be followed for over 8 mag. The plateau in the light profiles associated with the inner disk ($r \lesssim 60''$) is more pronounced in the UV than the *R* band. Both the MUV and *R* profiles flatten at *r* ~ 100". Neff et al. (1994) suggest that the UV halo is either indirect light from the UV-bright inner disk that is scattered by dust grains, or direct UV radiation from the stellar population in the outer disk. The absence of a significant change in the MUV-*R* color suggests the latter model, since one expects the dust to preferentially scatter the UV light. Despite the bright AGN, the stellar disk produces 81% of the integrated FUV and 83% of the MUV flux. The bright disk emission in NGC 1068 implies that even at UV wavelengths, the contribution of an active nucleus to the total light can be small and that composite AGN + starburst objects will be difficult to interpret at large redshift.

NGC 1275, Perseus A. - The central dominant galaxy in the Perseus Cluster, NGC 1275 is a peculiar E galaxy whose unusual features and evolutionary state have been extensively studied (e.g., Burbidge & Burbidge 1963; Rubin et al. 1977; McNamara, O'Connell, & Sarazin 1996). It contains a Seyfert-type AGN, evidence for recent star formation throughout its main body, an enormous system of line-emitting filaments near the systemic velocity, and a distinct system of emission line knots with a redshift ~ 3000 km s^{-1} greater than that of the galaxy. It is one of the best examples of mass accretion from an X-ray cooling flow.

NGC 1275 is detected in both the FUV and MUV (Fig. 9*a*). The nonthermal nucleus dominates the UV light for $r \lesssim 5''$, but it contributes only ~ 20% to the integrated FUV flux and $\lesssim$ 8% to the MUV flux. The off-nuclear FUV and MUV ligh distributions are clearly asymmetric. Smith et al. (1992) describe the UIT data in more detail. They subtracted symmetric elliptical fits to the MUV and found the residual UV continuum light to be spatially coincident with the extended lower (systemic) velocity $\mathrm{H}\alpha$ emission. There was evidence for UV emission from the high-velocity system as well, consistent with the photoionization requirements of the high-velocity $\mathrm{H}\alpha$ emitting gas. The UV colors of the main body of the galaxy (afte exclusion of the AGN and correction for significant internal extinction of A_{FUV} ~ 3.5) indicate the presence of stars with masses up to ~ 5 $M_{\odot}$ but not above, suggesting either a cessation of star formation in the last 50-100 Myr or a truncated initial mass function. The "super star clusters" discovered by *HST* (Holtzman et al. 1992; Carlson et al. 1998) are below our detection threshold. The unusual properties of this galaxy have been interpreted as products of either the cooling flow or a recent interaction/merger.

NGC 1316 (Fornax A, Arp 154). - A member of the Fornax cluster, this peculiar elliptical or S0 galaxy is at a distance of 19 Mpc. A system of dust filaments cross the minor axis, and there are numerous indications for the infall of material (Schweizer 1980). At MUV wavelengths, a central source is observed embedded in diffuse light from the prominent galactic bulge (Fig. 10*a*). The galaxy is only barely detected in the FUV. The diffuse extension to the southwest on the MUV image is spurious, produced by residual phosphorescence from a preceding exposure of the planet Jupiter. This artifact has been masked out of our photometry.

NGC 1317. - This early-type barred spiral (SAB(r)a) is located 6' north of NGC 1316. The UV images (Fig. 11*a*) show a bright, broken, elliptical ring of UV knots ~ 17" in diameter (~ 2.1 kpc at the adopted distance), roughly coincident with the Hα ring. The UV morphology is very different from the optical continuum morphology, which shows only traces of the knotty ring. These strong differences in morphology are found to be most pronounced for early-type disk systems. NGC 4736, observed during Astro-2, is another example of an early-type spiral, (SA(r)ab), with a strong, UV-bright central ring. Lacking multiwavelength imagery, NGC 1317 might be erroneously classified as a "ring" galaxy based solely on the UV morphology. Ring galaxies which have undergone a central penetrating collision (Marcum, Appleton, & Higdon 1992) are extremely rare systems; however, circumnuclear rings of massive star formation are much more common (Crocker, Baugus, & Buta 1996).

NGC 1399. - NGC 1399 is the central and brightest elliptical galaxy in the nearby (D ~ 19 Mpc) Fornax cluster of galaxies and is well detected in both UV bands (see Fig. 12*a*). The central FUV surface brightness is exceptionally high among the normal E galaxies and spiral bulges we have observed. There is a superposed foreground star visible 13" northeast of the nucleus on the MUV frame. As discussed by O'Connell et al. (1992) and Ohl et al. (1998), the radial light profiles in both the FUV and MUV (Fig. 12*b*) are consistent with a de Vaucouleurs ($\mu \sim r^{0.25}$) profile over a 5 mag range, suggesting that the FUV light is produced by low-mass stars from the dominant old stellar population. At larger radii, the axial ratio of the UV isophotes matches that of the optical, but there is a flattening of the UV isophotes for $r \lesssim 5''$ in both UV bands which appears to be real but has not been reported at longer wavelengths (Mackie, Visvanathan, & Carter 1990; Bicknell et al. 1989). There are strong (FUV-MUV) and (UV-optical) color gradients, in which the colors become redder with increasing radius. The central (FUV-MUV) color (~ -0.9, see Fig. 12*b*) is among the bluest known among normal elliptical galaxies. UIT images of the Fornax cluster field, including NGC 1399 and NGC 1404> are discussed by O'Neil et al. (1996).

NGC 1404.-This elliptical galaxy is also a member of the Fornax Cluster, located ~ 10' southeast of NGC 1399. The UV images (Fig. 13*a*) show a strong centrally peaked source. The bright object southeast of the galaxy core visible in the MUV image is a foreground star, which was masked out of the photometry. As in the case of most of the other old populations with good detections in the UV, NGC 1404 exhibits a significant UV color gradient (Fig. 13*b*) in which the colors become redder with increasing radius.

NGC 2146. - This is an infrared-luminous system, probably a postmerger object undergoing a burst of star formation (Hutchings et al. 1990). NGC 2146 appears to be a nearly edge-on spiral with two or more prominent dust lanes and a disturbed morphology. The MUV images show a compact central source, faint emission from the spiral arms (up to 2' from the nucleus), several discrete knots, and the strong dust lane. No emission is evident in the FUV image, presumably because the extensive dust layer lies in the foreground of the young population, similar to the morphology of M82. The UV/optical photometry is discussed further by Hennessy (1995).

NGC 2992 (Arp 245). - This highly inclined ($i \gtrsim 70°$) Sa galaxy hosts a Seyfert 1.9 nucleus and is interacting with the peculiar galaxy NGC 2993 at a projected separation of ~ 25 kpc. A strong interaction is inferred from the tidal tails and connecting bridge observed optically (Schombert, Wallin, & Struck-Marcell 1990). Optically, NGC 2992 shows a galactic bulge bisected by a dust lane (Ward et al. 1980). NGC 2992 is quite faint in the MUV and is not detected in the FUV (Fig. 15*a*). The MUV image reveals patchy, diffuse light at the position of the optically defined bulge (Fanelli et al. 1997a). Despite the AGN emission line spectrum seen in the optical (e.g., the bright Hα emission shown in Fig. 15*a*), there is no evidence of a compact UV nuclear source, most likely due to the dust lane and high inclination of the galaxy.

NGC 2993 (Arp 245). - This Sa spiral is a companion to NGC 2992. It is oriented more face-on than NGC 2992. By contrast with NGC 2992, the UV images (Fig. 16*a*) show a bright, centrally peaked source, identified as a probable starburst nucleus. The tracking was poor for the FUV exposure, leading to a slight tailing of the images.

NGC 3031 (M81). - At a distance of ~ 3.6 Mpc and having large angular size (14' × 26'), the grand design SA(s)ab spiral galaxy M81 is morphologically similar to M31 and has often been used as a test of density wave theories (e.g., Adler & Westphal 1996). FOCA images of M81 at 2000 Å with resolution ~ 20" have been analyzed by Blecha et al. (1990) and Reichen et al. (1994), who compared the UV continuum in detail to other tracers of spiral structure, including Hα, H I, and free-free radio emission.

A preliminary discussion of the UIT images (Fig. 17*a*) was given by Hill et al. (1992b). In the FUV, the bulge is very faint, and its surface brightness drops precipitously with radius, by 5.5 mag within 50", exhibiting a 2.5 mag increase in the (FUV-MUV) color (Fig. 17*b*). In both the MUV and FUV bands, the bulge follows a de Vaucouleurs $r^{0.25}$ profile within $r \lesssim$ 50". M81 contains a low-luminosity LINER/Seyfert 1 active nucleus. This AGN is not detectable in the UV at our 3" resolution, and our FUV profile shows no evidence of a nuclear point source. However, the active nucleus was recently detected in the UV with *HST* (Ho, Filippenko, & Sargent 1996; Devereux, Ford, & Jacoby 1997) as a faint point source ($d \lesssim$ 0".04) which photoionizes a small gas disk extending to r ~ 7".

In both the FUV and MUV frames of Figure 17*a*, the galaxy has a "ringlike" morphology, produced by the pattern of UV knots strung out along the dominant spiral arms and the faintness of the central regions of the galaxy out to r ~ 200". Not only do the outer parts of the bulge become very faint in the FUV, but there is evidently little underlying disk light inside 200". The inner edge of the disk near r ~ 250" also exhibits a large (FUV-MUV) color gradient, evidence of a rapid change in the mean age of the disk population. There are remarkable changes of morphology with wavelength. Comparing the MUV to the R band, we see that the outer disk becomes more prominent and structured at shorter wavelengths while the central bulge is much less prominent (see Fig. 17*a*). The contrast between the large UV color gradients and the tiny (B-R) gradient is striking in Figure 17*b*. The (FUV-MUV) color is roughly uniform at radii larger than 300" in the disk. The (UV-V) colors in the disk are redder than those observed in M33 and M74, indicating an older characteristic age for the disk (Cornett et al. 1994). In the rest-frame FUV, a high-redshift galaxy like M81 would not appear to be a normal spiral galaxy.

UV, Hα, and extinction properties of the 52 brightest resolved sources are discussed by (Hill et al. 1992b, 1995a). They estimate the total mass in recently formed massive stars (5-120 $M_{\odot}$) to be 1.4 × 10^5 $M_{\odot}$. The inferred star formation rate is 0.13 $M_{\odot}$ yr^{-1}. Allen et al. (1997) have compared the UIT images to Hα and H I maps of M81 at 9" resolution. They find that while bright Hα peaks are always associated with bright UV continuum peaks, the converse is not always true, which is expected because the UV continuum persists for many times the duration of strong photoionization. H I is closely associated with the UV continuum, suggesting that it is a produced by stellar UV photodissociation from a massive underlying H_2 layer and is not a precursor to star formation. Obscuration by dust has little effect on the morphology of M81 (or most of the other normal galaxies in this atlas), and Allen et al. (1997) argue that local chimneys blown in the dust layer by concentrated star formation permit the UV light to escape with little extinction.

NGC 3034 (M82). - M82 is the peculiar irregular companion to M81. Its central 500 pc contain a concentrated starburst (star formation rate ~ 10 $M_{\odot}$ yr^{-1}) with a bolometric luminosity 100 times larger than a corresponding volume in our own Galaxy (Telesco 1988; Reike et al. 1993; Waller, Gurwill, & Tamura 1992; O'Connell et al. 1995). The starburst has probably been triggered by a tidal interaction with M81 (now ~ 36' distant). M82 is observed nearly edge-on, and a complex network of dust lanes crisscross the galaxy.

M82 was first observed in the UV at 2000 Å with the FOCA experiment at ~ 15" resolution (Courvoisier et al. 1990). Our MUV image (Fig. 18*a*), with ~ 3" resolution, shows similar global features but with more detail. M82 was not detected in the 270 s FUV exposure, giving a limiting magnitude m(FUV) $\gtrsim$ 14.5 within an aperture of 4'.5 radius.

In the MUV, the galaxy clearly has a peculiar morphology. There are two extended bright structures along the major axis and a fan-shaped plume along the minor axis to the southeast. Fainter regions are detectable at larger radii (to r ~ 5'). Two dust lanes (also visible on the B-band image) are prominent in the MUV image: the strong central lane on the east side of the minor axis plume and another lane about 1' west of this. The brightest central knot on the B- or V-band images (labeled "A" in the notation of O'Connell & Mangano 1978) is considerably less conspicuous in the MUV but is still detectable despite extinction along the line of sight of A_V ~ 2 mag. The brightest region in the galaxy in the MUV is region "B," which lies about 1' east of the center. In optical bands this region has a high surface brightness, comparable to region A's, but a significantly lower extinction of A_V ~ 0.5 (Marcum & O'Connell 1996). The large UV/optical color excursions (see Fig. 18*b*) found within the main body appear to be produced mainly by the complex geometry of the dust layer within M82 (Hennessy 1995).

The fanlike MUV extension below the plane of M82 coincides with the southeastern base of the bright Hα plume discovered by Lynds & Sandage (1963), which is now thought to be associated with a superwind driven by supernova explosions in the starburst (Lehnert, Heckman, & Weaver 1999). However, the MUV light is much fainter on the northwest minor axis, and the general light distribution is much more asymmetrical than in Hα or optical continuum bands. The MUV/optical colors become bluer at larger radii in the southeastern plume. The MUV band does not contain any prominent emission lines from hot gas, so the light is virtually entirely continuum. Given evidence for extensive dust scattering in the halo of M82 (e.g., Schmidt, Angel, & Cromwell 1976; Scarrott, Eaton, & Axon 1991), the MUV light is best interpreted as scattering by dust grains of photons from the central starburst regions. This would require that lines of sight from the plume to the starburst regions have relatively low UV extinction. The asymmetry can be produced by preferential forward-scattering by grains in the southeastern plume, which kinematic evidence suggests is nearer us (e.g., Bland & Tully 1988). A more detailed discussion of the UV images of M82 is given by Hennessy (1995).

UGC 5336 (Holmberg IX, DDO 66). - UGC 5336 is a low surface brightness, dwarf irregular companion to M81. The MUV image (Fig. 19*a*), while shallow, does show diffuse irregular emission, but no prominent knots attributable to OB associations or individual main-sequence stars hotter than B0 are detected. Individual cooler stars with masses up to ~ 12 $M_{\odot}$ are detectable distributed across the face of the galaxy in the optical bands, apparently from a recent (~ 20-200 Myr old) population superposed on an older population which dominates the *V*-band light (Davidge & Jones 1989). The color profiles displayed in Figure 19*b* indicate that recently formed stars are spatially well mixed with the older population. The star formation history of Holmberg IX as revealed by the UV/optical imagery is discussed by Hill et al. (1993b). UIT data on other star-forming dwarf galaxies from the Astro-2 sample are discussed by Stewart et al. (2000).

UGC 6697. - UGC 6697 is a peculiar, late-type disk system, observed to be the brightest UV source in the field of the cluster Abell 1367. With a observed UV diameter of ~ 1', this system is apparently viewed close to edge-on, yet is remarkably bright in the UV (see Fig. 20*a*), in striking contrast to the inclined systems M82 and NGC 891. The latter apparently suffer much greater extinction by dust located external to most of the stellar component. UGC 6697 shows blue (FUV-MUV) colors throughout, with the UV/optical colors becoming significantly bluer at larger radii (Fig. 20*b*). Abell 1367 was also observed at 2000 Å with the FOCA experiment by Donas et al. (1990), who estimated star formation rates for UGC 6697 and other cluster members.

NGC 4151. - NGC 4151 is an early-type spiral, oriented approximately face-on, which hosts the prototypical Seyfert 1.5 AGN. The active nucleus is centered within a weak barlike or oval distortion with a PA ~ 130° (Simkin 1975). Near the ends of the bar are Hα-emitting knots symmetrically bracketing the nucleus (see Fig. 21*a*). Low surface brightness spiral arms are visible extending from the end of the barlike structure. The outer disk of NGC 4151 is optically faint and contains no prominent H II regions.

Fanelli et al. (1997a) discuss the UV morphology of NGC 4151. The unresolved, bright AGN dominates the light in both UV bands, producing ~ 81(82)% of the total FUV (MUV) light, unlike most of the other AGN systems in this sample. This result is produced by the absence of substantial massive star formation in the disk, and the face-on orientation of the galaxy, which minimizes absorption of the AGN continuum by dust. In addition to the AGN, two emission regions are seen in both UV bandpasses, on opposite sides of the nucleus. Each region is resolved into a few discrete knots, which correspond to the structure observed in the Hα image. The UV light in the knots is produced by recent massive star formation which appears to be localized near the end of the central bar. For the assumed distance, these star-forming regions extend to a radius of ~ 6 kpc. In the FUV, an additional diffuse component is detected, oval-shaped and brighter toward the nucleus. The lower surface brightness outer disk present in deep optical (cf. Arp 1977) and H I images (Pedlar et al. 1992) is not seen in the UV. In Figure 21*a*, note that the center of the Hα image is saturated.

NGC 4321 (M100). - NGC 4321 is a well-studied, grand design spiral galaxy, type SAB(s)bc, located within the Virgo Cluster. A prominent circumnuclear ring of recent star formation is inferred from Hα imagery, with a radius of ~ 15". The Astro-1 images are underexposed (see Fig. 22*a*), revealing the overall spiral arm pattern only faintly. The principal feature observed in the UV is a horseshoe-shaped broken circumnuclear ring, resolved into ~ 15-20 knots, bracketing the optically defined nucleus, which itself is fainter than the ring. This structure is ~ 16" × 24" in diameter, corresponding to a physical size of 1.2 × 1.7 kpc. The star-forming ring appears to be associated with a weak stellar bar observed at *I* (Pierce 1986) and in the NIR (Knapen et al. 1995). Despite the shallow exposure, it is apparent that the circumnuclear ring dominates the global UV light in this system.

5.2. Secondary Objects

Objects in the sample were classed as "secondary," due either to intrinsic faintness, truncated exposures, or those showing a point-source morphology. We present the UV imagery along with matching optical imagery where available in Figures 23*a* - 23*b*.

Mrk 335. - Classified as a Seyfert 1, the active nucleus is embedded in an early type galaxy (E or S0) at a redshift of $z = 0.025$ (Heckman & Balick 1981; MacKenty 1990). The UIT frames (Fig. 23*a*) show a bright, unresolved point source in both bandpasses. Fanelli et al. (1997a) find no excess UV flux which could be attributed to the host galaxy after modeling and subtraction of the central point source. The active nucleus dominates the light at UV and optical bandpasses, producing 100% of the UV light, 92% of the *R*-band flux (MacKenty 1990) and ~ 50% of the light at *K* (McLeod & Reike 1995).

NGC 891. - As one of the nearest edge-on systems, NGC 891 has been used to explore the vertical structure of galaxy disks (e.g., Morrison et al. 1997). It is unusual in showing bright diffuse Hα emission out to more than 4 kpc from the plane of the galaxy (Rand, Kulkarni, & Hester 1990), and deep continuum images show dust filaments extending out half that distance (Howk & Savage 1997).

The MUV image is underexposed (Fig. 23*a*). It shows a faint, spatially resolved linear structure coincident with the midplane of the galaxy. The UV light is most likely produced by stellar associations in the outer disk of the galaxy and by scattering of light from the inner disk by the extended dust. In the FUV (not shown), only very faint extended emission is observed.

NGC 1267, NGC 1268, NGC 1270, NGC 1272, NGC 1273, NGC 1277, NGC 1278, and NGC 1282. - Six of these galaxies detected on the MUV frame centered on NGC 1275 are members of the Perseus cluster. Most are early types, the latest being NGC 1268 (Sb). The brightest of these in the MUV is NGC 1267 (type E+), which shows a very compact source (see Fig. 23*a*). This could be a mild starburst or an active nucleus, although no radio emission has been reported. Although these objects are faint, we believe their (MUV-R) colors are accurate to 0.1-0.2 mag. After correction for foreground extinction, these have the reddest (MUV-R) colors (see Table 6) of any objects in our sample. A sufficiently large error ($\gtrsim$ 0.5 mag) in the estimate of foreground A_V seems unlikely. Instead, these may be metal-rich systems that lack the large extreme horizontal branch component which boosts the MUV flux in ellipticals like NGC 1399.

UGC 2665. - This late-type, highly inclined disk galaxy is barely detected in the MUV (see Fig. 23*a*). It is a background galaxy located in the field of view of the Perseus cluster. Like similar late-type disk systems in the primary object sample, the central bulge in this galaxy disappears at UV wavelengths.

NGC 1396. - This early-type galaxy, type SAB0-, is a member of the Fornax cluster. It is detected as a faint but clearly extended source in the MUV (Fig. 23*b*), but it is not seen in the FUV.

NGC 2551. - This disk system, type SA0/a, was seredipidously observed in a UIT pointing centered on Z Cam. In the MUV (Fig. 23*b*), the galaxy has a bright nucleus and a moderately bright disk showing clumpy structure.

NGC 3837. - This E galaxy is located in the Abell 1367 cluster. It shows as a slightly elongated structure on the MUV frame (Fig. 23*b*).

MCG 3-30-71. - This galaxy, of uncertain classification, is located in the Abell 1367 frame. It appears elongated in the MUV image (Fig. 23*b*), with the same orientation seen in POSS images. There is also a definite detection in the FUV frame.

NGC 3842. - This is another E galaxy located in the Abell 1367 cluster. It has a concentrated core detected in the MUV (Fig. 23*b*).

CGCG 97-114. - This compact galaxy is located in the Abell 1367 cluster. It appears as point source in both the FUV and MUV.

NGC 4156. - NGC 4156 is an Sb spiral located in the field of view of NGC 4151, but with a substantially larger redshift. Both the FUV and MUV images (Fig. 23*b*) show a centrally concentrated source and extended emission corresponding to the optical spiral arms.

UGC 7188. - This faint, late-type spiral is also located in the field of view of NGC 4151. The redshift quoted in Schneider et al. (1992) suggests that UGC 7188 is associated with NGC 4151. UGC 7188 appears as a resolved, diffuse source in both UV bandpasses (Fig. 23*b*). There are evidently large excursions in the UV/optical flux ratio with position.

NGC 4470. - This type Sa disk system is a member of the Virgo cluster, and located in the UIT frame centered on NGC 4472. Faint diffuse emission is seen in both the FUV and MUV frames (Fig. 23*b*).

NGC 4472. - The UIT frame for this well-known bright elliptical member of the Virgo cluster was badly underexposed. It was only faintly detected in the MUV (Fig. 23*b*).

NGC 4476. - This early-type galaxy (type SA0-), a member of the Virgo cluster, is located in the UIT frame centered on NGC 4472. It is detected only in the MUV image (Fig. 23*b*).

NGC 4478. - This elliptical, a member of the Virgo cluster and located in the UIT frame centered on NGC 4472, is faintly detected in the MUV (Fig. 23*b*) as a point source. Due to a large number of point source-like artifacts in this image (for example, note the bright source to the east), caution should be exercised in using this detection or associated photometry.

NGC 4486 (M87). - This is a well-known giant E galaxy in the Virgo cluster with an active nucleus, bright nonthermal jet, and X-ray cooling flow. The Astro-1 UIT images are underexposed. Only the central parts of the galaxy, including the nucleus and the nonthermal jet (the jet being brighter), are detected (Fig. 23*b*). Ohl et al. (1998) analyzed deeper exposures of M87 from Astro-2. The brightness of the nucleus and jet notwithstanding, they find that only 10% of the FUV light within a radius of 10" is contributed by these features and conclude that most of the UV light of M87 is stellar.

6. DISCUSSION

A discussion of our photometry and a quantitative analysis of UV/optical galaxy morphologies will be presented in later papers. Here, we summarize the more important trends regarding the UV morphologies of galaxies which have emerged from our data and related studies.

1. UV morphologies are usually significantly different from visible band morphologies. This is a consequence of spatially inhomogeneous stellar populations. Differences are most pronounced for systems in the middle range of Hubble types, Sa to Sc. Objects at the extremes of the Hubble sequence (ellipticals or very late disk systems and irregulars) tend to have more homogeneous populations and therefore less dramatic wavelength-dependent morphology.

2. Although elliptical galaxies and large spiral bulges are fainter in the far-UV than the optical bands by factors of ~ 6-60 (in flux per unit wavelength), nonetheless they are much brighter than expected from the cool ~ 1 $M_{\odot}$ turnoff stars in the dominant population. Their optical and UV axis ratios are similar, though they are usually much more compact in the UV. They exhibit smooth UV profiles, with none of the clumpiness normally associated with recent massive star formation. (Exceptions are NGC 1275, recently affected by a cooling flow or interaction, and the nonthermal jet in NGC 4486.) There is little UV evidence for dust in our sample of normal ellipticals at 3" resolution (though lanes are present in the peculiar objects NGC 1275 and 1316 and are often found at *HST* resolution in elliptical cores). Because of the absence of dust, the intergalactic ionizing radiation field of old stellar populations may be competitive with that of young populations in more dusty disk and irregular galaxies.

3. The ellipticals and spiral bulges exhibit large far-UV/optical color gradients in which the colors become redder outward (with the exception of NGC 221, where the gradient is strong but reversed). The gradients are larger than any at optical/IR wavelengths. The UV light is evidently extremely sensitive to the characteristics of its parent population. The FUV profiles of some of the early-type systems (e.g., NGC 221 and 1399) are well fitted by de Vaucouleurs functions, which are characteristic of spheroids at optical wavelengths. However, Ohl et al. (1998) find that the inner FUV profiles of some E/S0 galaxies are more consistent with an exponential function. Although exponentials are normally associated with disks, the FUV contours are generally consistent in shape and orientation with optical band isophotes, and the three-dimensional FUV light distributions are therefore unlikely to be genuinely disklike. Because of the large color gradients, it is not necessarily expected that the UV profiles of systems which are true spheroids at optical wavelengths would be closely de Vaucouleurs in shape.

4. The best evidence is that the far-UV light in most elliptical galaxies and large bulges is produced by extreme horizontal branch stars and their descendants in the dominant, low-mass, metal-rich population (O'Connell 1999 and references therein). The UV output of such objects is very sensitive to envelope properties and hence age, helium and metal abundance, and giant branch mass loss. It is a remarkable circumstance, if this interpretation is correct, that relatively crude UV observations can in principal determine envelope masses for stars in distant galaxies with a precision of a few 0.01 $M_{\odot}$.

5. The range in central (UV-optical) colors for early-type galaxies is very large, as first established by *IUE* spectra (e.g., Burstein et al. 1988). We find unusually red (MUV-R) values, after extinction corrections, for the early-type galaxies in the Perseus cluster. These may be metal-rich systems which lack the extreme HB component.

6. The cool stars in the large bulges of Sa and Sb spirals fade in the UV while the hot OB stars in their disks brighten such that their Hubble classifications (if these were attempted in the UV) would become significantly later. In the far-UV, early-type spirals can appear as peculiar, ringlike systems. At optical wavelengths, such structures would be associated with a short-lived, nonequilibrium situation, not with the stable configuration we know them to be.

7. The mean azimuthally averaged profiles of galaxy disks are approximately exponential in the UV but show considerably more structure than at optical wavelengths. In spiral disks with well organized, large amplitude spiral structure, the UV-bright structures closely outline the spiral pattern. In most cases, however, the UV appearance of disks can be considerably more fragmented and chaotic than at optical wavelengths, and the UV Hubble types are significantly later. UV suppression of bulge light in large-bulge spirals permits study of population changes in their inner disks, which appear to be dramatic in the case of M81.

8. The luminous AGNs in our sample range considerably in their contribution to the total UV light. In Mrk 335 the AGN is completely dominant; in NGC 4151 it contributes 80%; while in NGC 1068, 1275, and 4486 the contribution is only 10%-20%. A number of systems have unusual UV-bright structures in their inner disks, including rings (NGC 1317, 4321) and compact knots (NGC 1068). Such structures, and starburst nuclei (e.g., NGC 2993 here and M83 in Kuchinski et al. 2000), could easily dominate the UV light in high-redshift analogs.

9. Because of the often complex structural changes between the optical and UV bands, there is no simple relation between the half-light radii in these bands. However, in the most regular Sb-Sc spiral disks with good photometric coverage

(NGC 628 and 3031), the UV light is more extended than the optical continuum light.

10. Although none are illustrated in this paper, the cool bars of barred spirals become less prominent in the UV as well (Bohlin et al. 1983; Kuchinski et al. 2000), and this effect extends even to fairly late-type systems such as Magellanic irregulars (Page & Carruthers 1981; Smith, Cornett, & Hill 1987).

11. Dust in normal spiral disks does not dominate UV morphologies, despite the high selective UV extinction characteristic of Milky Way and Magellanic Cloud dust grains. The overall distributions of far-UV light and Hα light for those systems where both are available are quite similar even though $A(1500Å) / A(H\alpha) \sim 3.2$. Such ready escape of far-UV photons from normal spiral disks was not anticipated. Quantitative analysis of UV spectra of starburst galaxies shows that the UV continuum often suffers less extinction than predicted from optical band extinction estimates, e.g., based on Hα / Hβ ratios (Fanelli et al. 1988; Calzetti et al. 1994; Mas-Hesse & Kunth 1999). This is evidently mainly a consequence of the complex dust/star/gas geometries of star-forming regions. The emergent UV spectrum will, of course, always be weighted toward regions of lower extinction. But it appears that the heaviest extinction is confined to thin layers and the immediate vicinity of young H II complexes and that the UV light emerges from thicker star distributions, regions evacuated of dust by photodestruction or winds, or by virtue of strong clumpiness in dust concentrations (Fanelli et al. 1988; Calzetti et al. 1994; Calzetti 1997; Gordon, Calzetti, & Witt 1997; Allen et al. 1997). Only in cases like M82 and NGC 2146, where the dust layers appear dynamically disrupted, or the massive star formation is deeply embedded, does dust appear to be a major factor in UV morphology. A tentative conclusion from the available information is that dust will infrequently conceal the UV light of starburst activity for periods longer than ~ 50 Myr in the absence of continuing dynamical disturbances. This implies that some high-redshift starburst systems could be UV-bright.

12. Dust is expected to be more important in edge-on galaxies, and some of these can be very faint in the UV (e.g., NGC 891 here). However, other edge-on systems have high UV surface brightness, for instance UGC 6697 in this paper or NGC 4631 in Smith et al. (2000). Since the dust content of the outer disks of galaxies is expected to be low because of the lower metallicities there, one might expect many edge-on systems to be reasonably bright in the UV.

13. A significant fraction of the far-UV light in spiral disks is diffuse rather than being closely concentrated to obvious star-forming regions, and this appears to vary from object to object. The far-UV (1500 Å) light is in general more diffuse than is Hα. The diffuse component could arise from migration of UV-bright stars away from their birth sites during their ~ 50 Myr lifetimes, in situ star formation in low-density regions, or scattered light from dust grains. In the case of the Large Magellanic Cloud, UIT observations determined that about 70% of the detected 37,000 OB stars fell outside the boundaries of well-defined H II regions (Parker et al. 1998), consistent with diffuse component estimates from deeper, narrow-field *HST* observations (Brosch et al. 1999). The UV-bright plume of M82 indicates that dust scattering can be very important in some cases; similar instances of scattering in galactic winds might be detectable in high-redshift starburst systems.

7. CONCLUSION

This part of our UV/optical atlas of galaxies has compared vacuum UV imagery and photometry at 1500 and 2500 Å of selected nearby galaxies of all types obtained with the Ultraviolet Imaging Telescope during the Astro-1 mission with optical band data. The second part of the atlas (Kuchinski et al. 2000) discusses 1500 Å data from the Astro-2 mission for a sample of mainly face-on spiral galaxies. Later papers will discuss our UV/optical photometry, quantitative morphological comparisons, and simulations of the appearance of high-redshift objects based on this local sample.

All of the data discussed here are available electronically. The raw and pipeline-processed UIT data frames can be obtained from the Multimission Archive at the Space Telescope Science Institute. The processed image frames and photometry files used in this paper will be deposited in the NASA-Goddard Astronomical Data Center.

We are grateful to Laura Allen, George Becker, Mike Greason, Joan Hollis, Joel Offenberg, and Ronak Shah for assistance with this project and to all of those others who contributed to the success of the Astro-1 and Astro-2 missions. We acknowledge the use of the SkyView facility (http://skyview.gsfc.nasa.gov) located at NASA Goddard Space Flight Center and also the NASA/IPAC Extragalactic Database (NED), which is operated by the Jet Propulsion Laboratory, California Institute of Technology, under contract with NASA. Funding for the UIT project was provided through the *Spacelab* Office at NASA Headquarters under project number 440-51. Additional support was provided by NASA grants NAG5-700, NAGW-2596, and NAG5-6403 to the University of Virginia.

APPENDIX A

STAR FORMATION HISTORY WEIGHTING FUNCTIONS

Stars are intrinsically broadband emitters. As a consequence, the integrated light of a stellar population at any wavelength contains contributions from many parts of the Hertzsprung-Russell diagram and necessarily from all ages present in the population. However, there is a significant wavelength dependence in sensitivity to age, which can be used to extract information on the history of a population.

A useful way of quantifying the dependence of the integrated light on the star formation history is in the form of a "history weighting function." This describes how much the stars of a given generation affect the resultant luminosity at each wavelength. Here we give a simple analytic illustration of weighting functions in three important wavelength regimes discussed in the main text: the ultraviolet ionizing continuum (λ < 912 Å), the far-UV continuum (~ 1500 Å), and the optical band (here, the *V* band).

Detailed spectral synthesis models (e.g., Larson & Tinsley 1978; Bruzual & Charlot 1993) show that the integrated light of a given generation of stars decays roughly as a power law in the age *t*: $L(\lambda,t) \sim a(\lambda)t^{-\beta(\lambda)}$. The function $a(\lambda)$ describes the initial spectral energy distribution per unit mass of the generation. The power-law time dependence is a good approximation over most of the interesting range of ages (at least after ~ 2 million years) and for most wavelengths. Although some treatments in the literature assume the decay is exponential, this is clearly unphysical because it implies a constant decay time whereas the actual timescale for stellar evolution increases as the turnoff mass decreases.

A power-law dependence implies that photometric measures for the integrated light, stated in conventional magnitude units, respond in proportion to log *t*. This means that we should imagine the history of a galaxy as a set of bins of constant size in δ log *t* stretching from the present to a lookback time of ~ 15 Gyr. The appropriate size for the bins is governed by the number of independent data points available, the wavelength range, and the photometric precision. The log *t* binning implies that much less information is available on the details of the early history than on more recent times. This is true for both integrated light and resolved color-magnitude diagrams.

From a spectral synthesis routine written by W. Landsman (see Hill et al. 1994b), which uses the Geneva stellar evolutionary tracks, we find for the Lyman continuum, the 1500 Å continuum, and the *V* band that β ~ 4.3, 1.5, and 0.8, respectively. (At 1500 Å there is an abrupt increase in β for times after 500 Myr.) These values are for solar abundance. Other model sets (e.g., Bruzual & Charlot 1993) yield similar results, but the exact figures are not important for our discussion.

The integrated present-day luminosity of a galaxy is then given by

$$L(\lambda) \sim a(\lambda) \int \mathrm{SFR}(t_0 - t)\, t^{-\beta(\lambda)}\, dt\,,$$

where SFR is the star formation rate ($M_{\odot}$ yr^{-1}) at a given cosmic time, t_0 is the present cosmic epoch, and *t* is the lookback time to the formation of each generation. Here, we are not so much interested in the actual spectrum of the galaxy as in visualizing how activity in log *t* bins over four decades in age (1-15,000 Myr) affects observations at each wavelength. So, we can rewrite this expression as

$$L(\lambda) \sim L_1(\lambda) \int \mathrm{SFR}(t_0 - 10^{\zeta})\, W(\lambda, \zeta)\, d\zeta\,,$$

where $\zeta = \log_{10} t$ and L_1 is the luminosity produced for a continuous star formation rate of 1 $M_{\odot}$ yr^{-1}. The normalized weighting function is $W(\lambda, \zeta) = b(\lambda) \exp\{2.30\, [1 - \beta(\lambda)]\, \zeta\}$. It measures the relative contribution of each generation of stars in log *t* space to the present-day luminosity at each wavelength. The integral of *W* over log *t* is unity in this formulation. For our three wavelength regimes, $b(\lambda)$ = 74.0, 1.74, and 0.08, respectively, where we have truncated the 1500 Å integral at 500 Myr.

The history weighting functions are plotted in Figure 24. The three wavelengths offer very different age sensitivities and therefore serve to "dissect" the star formation history. The weighting functions other than that for the Lyman continuum are broad and smooth. This is typical of most wavelengths. The absence of structure in the weighting functions makes analysis of star formation histories difficult and is an important contributor to a number of well-known ambiguities and controversies in integrated light analysis. Our ability to extract information on the history of star formation from integrated light depends strongly on the range of wavelengths observed.

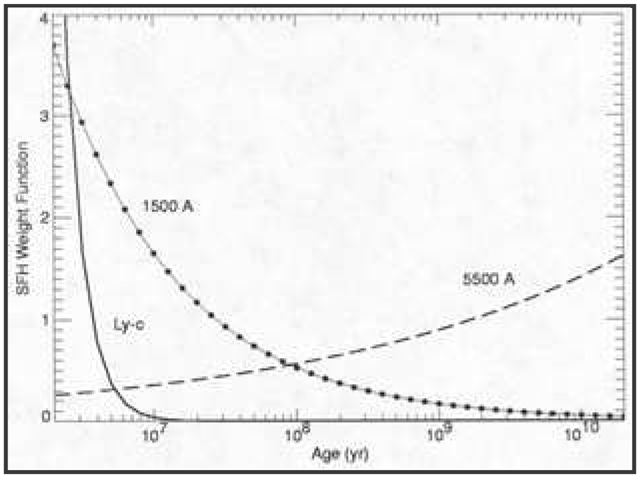

Figure 24. Normalized history weighting functions showing the contribution of star formation activity at various times in the past to the integrated light in three wavelength regimes. The vertical scale is linear. The curves for 1500 and 5500 Å are plotted at 3 times their actual values.

The sensitivity of Lyman continuum radiation, and hence strong emission lines or radio free-free continuum, to star formation declines rapidly with age and is essentially 0 for times over 10 Myr in the past. These indicators are very useful but also of very limited scope. The 1500 Å continuum is also most sensitive to the youngest stars, but its usefulness extends another factor of 50 in age beyond 10 Myr. The integrated *V*-band light of a single generation decays slowly, so the present-day *V*-band light of a galaxy can be strongly composite. It is most sensitive to populations over 1 Gyr in age. The 1500 Å and *V*-band continua are about equally sensitive to stars of age ~ 100 Myr.

An alternative way of quantifying the sensitivity of different wavelengths to the star formation history is by determining light-weighted "mean ages" at each wavelength (e.g., O'Connell 1990; Hill et al. 1994b). Defined as in the latter reference, mean ages for the Lyman continuum, the far-UV continuum, and the *V* band are 2 Myr, 35 Myr, and 2 Gyr, respectively.

APPENDIX B

GROWTH CURVE PHOTOMETRY

Table 9 presents the detailed surface brightness profiles and growth curves for our primary targets. We note that the values listed in Table 9 have *not* been corrected for foreground extinction. We felt that this photometry is most useful to the community as measured from the images, without our assumptions regarding extinction. The values for each bandpass are truncated at the radius where the profiles flatten, or in some cases based on visual inspection of the image. For some objects the UV light curves are still rising at radii for which the profiles should have flattened, due to image defects within the UIT images which can add net positive flux to the larger annuli. For images lacking an absolute calibration (all are Hα or *R*-band data) the relative magnitudes are indicated as such by an italic font. Mismatches between the UV and optical-band point spread functions render color comparisons within *r* ~ 5" unreliable.

Table 9. Growth Curve Photometry

This table is available only on-line as a machine-readable table.

Table 9

REFERENCES

1. Aaronson, M., & Mould, J. 1981, PASP, 93, 20
2. Abraham, R. G. 1997, in The Ultraviolet Universe at Low and High Redshift, ed. W. Waller, M. Fanelli, J. Hollis, & A. Danks (New York: AIP), 195

3. Abraham, R. G., Freedman, W., & Madore, B. 1997, in The *Hubble Space Telescope* and the High Redshift Universe, ed. N. R. Tanvir, A. Aragon-Salamanca, & J. V. Wall (London: World Scientific), 57
4. Adler, D. S., & Westphal, D. J. 1996, AJ, 111, 735
5. Allen, R. J., Knapen, J. H., Bohlin, R., & Stecher, T. P. 1997, ApJ, 487, 171
6. Arp, H. 1977, ApJ, 218, 70
7. Barth, A. J., Ho, L. C., Filippenko, A. V., & Sargent, W. L. W. 1998, ApJ, 496, 133
8. Bertola, F., Bressan, A., Burstein, D., Buson, D., Chiosi, C., & Di Serego Alighieri, S. 1995, ApJ, 438, 680
9. Bessell, M. S. 1986, PASP, 98, 1303
10. Bicknell, G. V., Carter, D., Killeen, N. E., & Bruce, T. E. 1989, ApJ, 336, 639
11. Bland, J., & Tully, B. 1988, Nature, 334, 43
12. Blecha, A., Golay, M., Huguenin, D., Reichen, D., & Bersier, D. 1990, A&A, 233, L9
13. Bohlin, R. C., Cornett, R. H., Hill, J. K., Hill, R. S., O'Connell, R. W., & Stecher, T. P. 1985, ApJ, 298, L37
14. Bohlin, R. C., Cornett, R. H., Hill, J. K., Hill, R. S., & Stecher, T. P. 1988, ApJ, 334, 657
15. Bohlin, R., Cornett, R., Hill, J., Smith, A., & Stecher, T. 1983, ApJ, 274, L53
16. Bohlin, R. C., et al. 1991, ApJ, 368, 12
17. Bohlin, R. C., et al. 1993, ApJ, 417, 127
18. Bouwens, R., Broadhurst, T., & Silk, J. 1998, ApJ, 506, 579
19. Brinchmann, J., et al. 1998, ApJ, 499, 112
20. Brosch, N. 1999, Exp. Astron., 9, 119
21. Brosch, N., Shara, M., MacKenty, J., Zurek, D., & McLean, B. 1999, AJ, 117, 206
22. Brown, T. M., Ferguson, H. C., Stanford, S. A., & Deharveng, J.-M. 1998, ApJ, 504, 113
23. Brown, T. M., Bowers, C. W., Kimble, R. A., Sweigart, A. V., & Ferguson, H. C. 2000, ApJ, 532, 308
24. Bruhweiler, F. C., Truong, K. Q., & Altner, B. 1991, ApJ, 379, 596
25. Bruzual, G., & Charlot, S. 1993, ApJ, 405, 538
26. Buat, V., Vuillemin, A., Burgarella, D., Milliard, B., & Donas, J. 1994, A&A, 281, 666
27. Bunker, A. J. 1999, in ASP Conf. Ser. 191, Photometric Redshifts and High-Redshift Galaxies, ed. R. Weymann, L. Storrie-Lombardi, M. Sawicki, & R. Brunner (San Francisco: ASP), 317
28. Burbidge, E. M., & Burbidge, G. R. 1965, ApJ, 142, 1351
29. Burstein, D., Bertola, F., Buson, L. M., Faber, S. M., & Lauer, T. R. 1988, ApJ, 328, 440
30. Calzetti, D. 1997, AJ, 113, 162
31. Calzetti, D., Kinney, A. L., & Storchi-Bergmann, T. 1994, ApJ, 429, 582
32. Cardelli, J. A., Clayton, G. C., & Mathis, J. S. 1989, ApJ, 345, 245 (CCM)
33. Carlson, M. N., et al. 1998, AJ, 115, 1778
34. Carruthers, G. R., Heckathorn, H. M., & Opal, C. B. 1978, ApJ, 225, 346
35. Cepa, J., & Beckman, J. E. 1990, ApJ, 349, 497
36. Chen, P. C., et al. 1992, ApJ, 395, L41
37. Cheng, K.-P., et al. 1992, ApJ, 395, L29
38. Cheng, K.-P., Hintzen, P., Smith, E. P., Angione, R., Talbert, F., Collins, N., & Stecher, T. P. 1996, Ground-Based CCD Imaging in Support of the Astro/UIT Mission (3 vols.; NSSDC CDROMs)
39. Cole, A. A., et al. 1998, ApJ, 505, 230
40. Condon, J. J. 1992, ARA&A, 30, 575
41. Corbin, M. R., Vacca, W. D., O'Neil, E., Thompson, R. I., Rieke, M., & Schneider, G. 2000, AJ, 119, 1062
42. Cornett, R. H., et al. 1992, ApJ, 395, L9
43. Cornett, R. H., et al. 1994, ApJ, 426, 553
44. Cornett, R. H., Greason, M. R., Hill, J. K., Parker, J. W., & Waller, W. H. 1997, AJ, 113, 1011
45. Courvoisier, T. J.-L., Reichen, M., Blecha, A., Golay, M., & Huguenin, D. 1990, A&A, 238, 63
46. Crocker, D. A., Baugus, P. D., & Buta, R. 1996, ApJS, 105, 353
47. Davidge, T. J., & Jones, J. H. 1989, AJ, 97, 1607
48. Deharveng, J.-M., Laget, M., Monet, G., & Vuillemin, A. 1976, A&A, 50, 371
49. Deharveng, J.-M., Milliard, B., Laget, M., & Jakobsen, P. 1980, A&A, 88, 52
50. Deharveng, J.-M., Sasseen, T. P., Buat, V., Bowyer, S., Lampton, M., & Wu, X. 1994, A&A, 289, 715
51. de Jong, R. S., & van der Kruit, P. C. 1994, A&AS, 106, 451
52. de Vaucouleurs, G., de Vaucouleurs, A., Corwin, H. G., Jr., Buta, R. J., Paturel, G., & Fouque, P. 1991, Third Reference Catalog of Bright Galaxies (New York: Springer) (RC3)
53. Devereux, N., Ford, H., & Jacoby, G. 1997, ApJ, 481, L71
54. Djorgovski, S. B. 1985, Ph.D. thesis, Univ. California, Berkeley
55. Donas, J., Deharveng, J. M., Laget, M., Milliard, B., & Huguenin, D. 1987, A&A, 180, 12
56. Donas, J., Milliard, B., & Laget, M. 1995, A&A, 303, 661
57. Donas, J., Milliard, B., Laget, M., & Buat, V. 1990, A&A, 235, 60
58. Donas, J., Milliard, B., Laget, M., & Deharveng, J. M. 1981, A&A, 97, L7
59. D'Onofrio, M., Capaccioli, M., Zaggia, S. R., & Caon, N. 1997, MNRAS, 289, 847

60. Elmegreen, D. M. 1980, ApJS, 43, 37
61. Elmegreen, D. M. 1981, ApJS, 47, 229
62. Fanelli, M. N., Collins, N., Bohlin, R. C., Neff, S. G., O'Connell, R. W., Roberts, M. S., Smith, A. M., & Stecher, T. P. 1997a, AJ, 114, 575
63. Fanelli, M. N., O'Connell, R. W., Burstein, D., & Wu, C.-C. 1992, ApJS, 82, 197
64. Fanelli, M. N., O'Connell, R. W., Thuan, T. X. 1988, ApJ, 334, 665
65. Fanelli, M. N., et al. 1997b, in The Ultraviolet Universe at Low and High Redshift, ed. W. Waller, M. Fanelli, J. Hollis & A. Danks (New York: AIP), 83
66. Ferrarese, L., et al. 1996, ApJ, 464, 568
67. Frogel, J. A. 1985, ApJ, 298, 528
68. Freedman, W. L. 1990, ApJ, 355, L35
69. Freedman, W. L., & Madore, B. F. 1990, ApJ, 365, 186
70. Freedman, W. L., Wilson, C. D., & Madore, B. F. 1991, ApJ, 372, 455
71. Freedman, W. L., et al. 1994, ApJ, 427, 628
72. Fruscione, A., & Gavazzi, G. 1990, A&A, 230, 293
73. Gallagher, J. S., Hunter, D. A., & Tutukov, A. V. 1984, ApJ, 284, 544
74. Giavalisco, M., Livio, M., Bohlin, R. C., Macchetto, F. D., & Stecher, T. P. 1996, AJ, 112, 369
75. Godwin, J. G., & Peach, J. V. 1982, MNRAS, 200, 733
76. Gordon, K. D., Calzetti, D., & Witt, A. N. 1997, ApJ, 487, 625
77. Goudfrooij, P., Hansen, L., Jorgensen, H. E., Norgaard-Nielsen, H. U., de Jong, T., & van den Hoek, L. B. 1994, A&AS, 104, 179
78. Greggio, L., & Renzini, A. 1990, ApJ, 364, 35
79. Heckman, T. M., & Balick, B. 1981, ApJ, 247, 32
80. Hennessy, G. S. 1995, Ph.D. thesis, Univ. Virginia
81. Hill, J. K., et al. 1992a, ApJ, 395, L33
82. Hill, J. K., et al. 1992b, ApJ, 395, L37
83. Hill, J. K., et al. 1993a, ApJ, 413, 604
84. Hill, J. K., et al. 1993b, ApJ, 402, L45
85. Hill, J. K., Isensee, J. E., Bohlin, R. C., O'Connell, R. W., Roberts, M. S., Smith, A. M., & Stecher, T. P. 1993c, ApJ, 414, L9
86. Hill, J. K., et al. 1994a, ApJ, 425, 122
87. Hill, J. K., et al. 1995a, ApJ, 438, 181
88. Hill, J. K., et al. 1995b, ApJS, 98, 595
89. Hill, R. S., Cheng, K.-P., Bohlin, R. C., O'Connell, R. W., Roberts, M. S., Smith, A. M., & Stecher, T. P. 1995c, ApJ, 446, 622
90. Hill, R. S., Home, A. T., Smith A. M., Bruhweiler, F. C., Cheng, K.-P., Hintzen, P. M. N., & Oliversen, R. J. 1994b, ApJ, 430, 568
91. Ho, L. C., Fillipenko, A. V., & Sargent, W. L. W. 1996, ApJ, 462, 183
92. Hodge, P. W. 1966, Atlas and Catalogue of H II Regions in Galaxies (Seattle: Univ. Washington)
93. Hodge, P. W., & Kennicutt, R. C. 1983, AJ, 88, 296
94. Holtzman, J. A., et al. 1992, AJ, 103, 691
95. Howk, J., & Savage, B. D. 1997, AJ, 114, 2463
96. Hutchings, J. B., Neff, S. G., Stanford, S. A., Lo, E., & Unger, S. W. 1990, AJ, 100, 60
97. Hutchings, J. B., et al. 1991, ApJ, 377, L25
98. Keel, W. C. 1998, ApJ, 506, 712
99. Kennicutt, R. C. 1998, ARA&A, 36, 189
100. Kennicutt, R. C., & Hodge, P. W. 1980, ApJ, 241, 573
101. Kennicutt, Jr., R. C., & Kent, S. M. 1983, AJ, 88, 1094
102. Kent, S. M. 1987, AJ, 94, 306
103. King, I. R., et al. 1992, ApJ, 397, L35
104. King, I. R., Stanford, S. A., & Crane, P. 1995, AJ, 109, 164
105. Knapen, J. H., Beckman, J. E., Shlosman, I., Peletier, R. F., Heller, C. H., & De Jong, R. S. 1995, ApJ, 443, L73
106. Kohle, S., Kissler-Patig, M., Hilker, M., Richtler, T., Infante, L., & Quintana, H. 1996, A&A, 309, L39
107. Kuchinski, L. E., et al. 2000, ApJS, 131, 441
108. Landsman, W. B., Roberts, M. S., Bohlin, R. C., O'Connell, R. W., Smith, A. M., & Stecher, T. P. 1992, ApJ, 401, L83
109. Larson, R. B., & Tinsley, B. M. 1978, ApJ, 219, 46
110. Lasker, B. M., Sturch, C. R., Mclean, B. J., Russell, J. L., Jenkner, H., & Shara, M. M. 1990, AJ, 99, 2019
111. Lauer, T. R., Faber, S. M., Ajhar, E. A., Grillmair, C. J., & Scowen, P. A. 1998, AJ, 116, 2263
112. Lehnert, M. D., Heckman, T. M., & Weaver, K. A. 1999, ApJ, 523, 575
113. Lilly, S. J., Tresse, L., Hammer, F., Crampton, D., & Le Fèvre, O. 1995, ApJ, 455, 108
114. Lynds, C. R., & Sandage, A. R. 1963, ApJ, 137, 1005

115. MacKenty, J. W. 1990, ApJS, 72, 231
116. Mackie, G., Visvanathan, N., & Carter, D. 1990, ApJS, 73, 637
117. Madau, P., Ferguson, H. C., Dickinson, M. E., Giavalisco, M., Steidel, C. C., & Fruchter, A. 1996, MNRAS, 283, 1388
118. Maoz, D., Filippenko, A. V., Ho, L. C., Macchetto, F. D., Rix, H.-W., & Schneider, D. P. 1996, ApJS, 107, 215
119. Maoz, D., Filippenko, A. V., Ho, L. C., Rix, H.-W., Bahcall, J. N., Schneider, D. P., & Macchetto, F. D. 1995, ApJ, 440, 91
120. Marcum, P. M., Appleton, P. N., & Higdon, J. L. 1992, ApJ, 399, 57
121. Marcum, P. M., & O'Connell, R. W. 1996, in ASP Conf. Ser. 98, From Stars to Galaxies: The Impact of Stellar Physics on Galaxy Evolution, ed. C. Leitherer, U. Fritze-von-Alvensleben, & J. Huchra (San Francisco: ASP), 419
122. Martin, C., Hurwitz, M., & Bowyer, S. 1990, ApJ, 354, 220
123. Martin, C., Milliard, B., Viton, M., & Donas, J. 1997, in The Ultraviolet Universe at Low and High Redshift, ed. W. Waller, M. Fanelli, J. Hollis, & A. Danks (New York: AIP), 73
124. Martin, C. D., et al. 1999, in ASP Conf. Ser. 164, Ultraviolet-Optical Space Astronomy Beyond *HST*, ed. J. A. Morse, J. M. Shull, & A. L. Kinney (San Francisco: ASP), 182
125. Mas-Hesse, J. M., & Kunth, D. 1999, A&A, 349, 765
126. Massey, P., Bianchi, L., Hutchings, J. B., & Stecher, T. P. 1996, ApJ, 469, 629
127. McGlynn, T., Scollick, K., & White, N. 1996, in IAU Symp. 179, New Horizons from Multiwavelength Sky Surveys, ed. B. J. McLean et al. (Dordrecht: Kluwer), 465
128. McLeod, K. K., & Reike, G. H. 1995, ApJ, 441, 96
129. McMillan, R., Ciardullo, R., & Jacoby, G. H. 1993, ApJ, 416, 62
130. McNamara, B. R., O'Connell, R. W., & Sarazin, C. L. 1996, AJ, 112, 91
131. Michard, R. 1982, A&AS, 49, 591
132. Milliard, B., Donas, J., & Laget, M. 1991, Adv. Space Res., 11(11), 135
133. Morrison, H. L., Miller, E. D., Harding, P., Stinebring, D. R., & Boroson, T. A. 1997, AJ, 113, 2061
134. Neff, S. G., Fanelli, M. N., Roberts, L. J., O'Connell, R. W., Bohlin, R. C., Roberts, M. S., Smith, A. M., & Stecher, T. P. 1994, ApJ, 430, 545
135. O'Connell, R. W. 1987, AJ, 94, 876
136. O'Connell, R. W. 1990, in Windows on Galaxies, ed. G. Fabbiano, J. S. Gallagher, & A. Renzini (Dordrecht: Kluwer), 39
137. O'Connell, R. W. 1991, Adv. Space Res., 11(11), 71
138. O'Connell, R. W. 1999, ARA&A, 37, 603
139. O'Connell, R. W., et al. 1992, ApJ, 395, L45
140. O'Connell, R. W., Gallagher, J. S., Hunter, D. A., & Colley, W. N. 1995, ApJ, 446, L1
141. O'Connell, R. W., & Mangano, J. J. 1978, ApJ, 221, 62
142. Ohl, R. G., et al. 1998, ApJ, 505, L11
143. O'Neil, K., Bothun G. D., Smith, E. P., & Stecher, T. P. 1996, AJ, 112, 431
144. Page, T., & Carruthers, G. R. 1981, ApJ, 248, 906
145. Parker, J. W., Hill, J. K., Bohlin, R. C., O'Connell, R. W., Neff, S. G., Roberts, M. S., Smith, A. M., & Stecher, T. P. 1996, ApJ, 472, L29
146. Parker, J. W., et al. 1998, AJ, 116, 180
147. Pedlar, A., Howley, P., Axon, D. J., & Unger, S. W. 1992, MNRAS, 259, 369
148. Pei, Y. C., & Fall, S. M. 1995, ApJ, 454, 69
149. Peletier, R. F., Davies, R. L., Illingworth, G. D., Davis, L. E., Cawson, M. 1990, AJ, 100, 1091
150. Petit, H., Hua, C. T., Bersier, D., & Courtes, G. 1996, A&A, 309, 446
151. Pierce, M. J. 1986, ApJ, 305, 204
152. Prugniel, P., & Heraudeau, P. 1998, A&AS, 128, 299
153. Rand, R. J., Kulkarni, S. R., & Hester, J. J. 1990, ApJ, 352, L1
154. Reichen, M., Kaufman, M., Blecha, A., Golay, M., & Huguenin, D. 1994, A&AS, 106, 523
155. Reike, G. H., Loken, K., Reike, M. J., & Tablyn, P. 1993, ApJ, 412, 99
156. Renzini, A., Greggio, L., di Serego Alighieri, S., Cappellari, M., Burstein, D., & Bertola, F. 1995, Nature, 378, 39
157. Rubin, V. C., Ford, W. K., Peterson, C. J., & Oort, J. H. 1977, ApJ, 211, 693
158. Scarrott, S. M., Eaton, N., & Axon, D. J. 1991, MNRAS, 252, 12P
159. Schild, R., Tresch-Fienberg, R., & Huchra, J. 1985, AJ, 90, 441
160. Schmidt, G. D., Angel, J. R., & Cromwell, R. H. 1976, ApJ, 206, 888
161. Schneider, S. E., Thuan, T. X., Mangum, J. G., & Miller, J. 1992, ApJS, 81, 5
162. Schombert, J. M., Wallin, J. F., & Struck-Marcell, C. 1990, AJ, 99, 497
163. Schweizer, F. 1980, ApJ, 237, 303
164. Sharina, M. E., Karachentsev, I. D., & Tikhonov, N. A. 1996, A&AS, 119, 499
165. Shaya, E. J., et al. 1996, AJ, 111, 2212
166. Simkin, S. M. 1975, ApJ, 200, 567
167. Smith, A. M., Cornett, R. H., & Hill, R. S. 1987, ApJ, 320, 609

168. Smith, A. M., et al. 2000, ApJ, in press
169. Smith, B. J., & Harvey, P. M. 1996, ApJ, 468, 139
170. Smith, E. P., et al. 1992, ApJ, 395, L49
171. Snijders, M. A., Briggs, S. A., & Boksenberg, A. 1982, in Proc. Third European *IUE* Conference, ed. M. Grewing (Noordwijk: ESA), 551
172. Sohn, Y.-J., & Davidge, T. J. 1996, AJ, 111, 2280
173. Stecher, T., Bohlin, R., Hill, J., & Jura, M. 1982, ApJ, 255, L99
174. Stecher, T. P., et al. 1992, ApJ, 395, L1
175. Stecher, T. P., et al. 1997, PASP, 109, 584
176. Steidel, C. C., Adelberger, K. L., Giavalisco, M., Dickinson, M., & Pettini, M. 1999, ApJ, 519, 1
177. Stewart, S. E., et al. 2000, ApJ, 529, 201
178. Stone, R. P. S. 1977, ApJ, 218, 767
179. Telesco, C. M. 1988, ARA&A, 26, 343
180. Treyer, M. A., Ellis, R. S., Milliard, B., Donas, J., & Bridges, T. J. 1998, MNRAS, 300, 303
181. Usui, T., Saito, M., & Tomita, A. 1998, AJ, 116, 2166
182. Waller, W. H., Gurwell, M., & Tamura, M. 1992, AJ, 104, 63
183. Waller, W. H., et al. 1995, AJ, 110, 1255
184. Ward, M., Penston, M. V., Blades, J. C., & Trutle, A. J. 1980, MNRAS, 193, 563
185. Weedman, D. W., & Huenemoerder, D. P. 1985, ApJ, 291, 72
186. Witt, A., Stecher, T., Boroson, T., & Bohlin, R. 1989, ApJ, 336, L21
187. Young, J. S., Kleinmann, S. G., & Allen, L. E. 1988, ApJ, 334, L63